CHARACTERIZATION OF CG9426 AS ORTHOLOG OF ID-CAUSATIVE GENE IPP AND ANALYSIS OF ITS EXPRESSION PATTERN IN THE *DROSOPHILA* NERVOUS SYSTEM

by

Eymen Ece Oruç

B.S., Molecular Biology and Genetics, Boğaziçi University, 2021

Submitted to the Institute for Graduate Studies in
Science and Engineering in partial fulfillment of
the requirements for the degree of
Master of Science

Graduate Program in Molecular Biology and Genetics
Boğaziçi University
2023

ACKNOWLEDGEMENTS

First of all, I should express my gratitude to my dear advisor Prof. Arzu Çelik Fuss, for providing me the opportunity to gain all the experience through this journey. I am also thankful to Asst. Prof. Şükrü Anıl Doğan and Assoc. Prof. Aslı Kumbasar for devoting their precious time to evaluate my thesis.

I extend my thanks to Dr. Anastasia Fokina, who supervised and taught me most of the molecular experiments that were conducted in this study, for her guidance and patience. I also owe a thank to Dr. Farzaneh Larti for supporting me and helping me to gain my self-esteem; to Berfin Dağ and Ece Nur Erol for their companionship, being with me during all my laughter and tears; to Barış Can Mandacı and Ayşe Kahraman for giving me the confidence to ask every single question that came to my mind.

I am thankful to Elif Darbuka Tula, Gamze Sakallı, Muhammed Solkol, Taha Akkülah, and Mert Tufan for their help in my experiments and to all the lovely members of the Fly Lab for cherishing the day and reducing the stress of hard work.

I should thank my father, my dear sisters Nazlı and Melis, and my lovely friends, Gülru, Güz, Elifnaz and Melisa for their emotional support whenever I needed and for their understanding for the times that I couldn’t spend with them in these two years.

I also thank TUBITAK as I was financially supported by TUBITAK 2210-A National MSc/MA Scholarship Program. This study was supported by Boğaziçi University Research Fund with Grant Number 18121 (21B01M1).

ABSTRACT

CHARACTERIZATION OF CG9426 AS ORTHOLOG OF ID-CAUSATIVE GENE IPP AND ANALYSIS OF ITS EXPRESSION PATTERN IN THE *DROSOPHILA* NERVOUS SYSTEM

Intellectual disability (ID) is defined as general deprivation in cognition and learning, affecting around 1-2% of people worldwide. Although the underlying causes of ID are numerous and complex, there is a convergence in mechanisms that are affected. Intracisternal A particle-promoted polypeptide (*IPP*) gene encodes for 584amino acid-long IPP protein that includes a BTB/POZ domain, a BTB/Kelch associated domain and 6 Kelch-repeat domains. The Kelch protein family is known to be essential for maintaining the actin organization. There have been 63 members identified in the Kelch protein superfamily and several of them have been associated with intellectual disability. *Drosophila melanogaster* provides numerous advantages in modelling human brain diseases due to its short life span, large number of offspring and ease of genetic manipulation with currently available techniques. CG9426 is the *Drosophila* ortholog of the *IPP* gene sharing 37% identity and 58% similarity. My aim was to analyze the morphological outcomes of dysregulation of IPP by using *Drosophila melanogaster* as a model organism and obtain a broader perspective on IPP. In this study I demonstrated how IPP expression compensated for the low viability rate and reduced the ratio of mushroom body defects in *CG9426* knockout mutants. These results support the idea that *CG9426* and *IPP* are functional orthologs, and *Drosophila melanogaster* can be a suitable model to understand the causative of role of IPP in intellectual disability. The expression pattern of CG9426 was analyzed and found to be expressed in neuroblasts in the larval brain and glial cells in the adult fly brain. Glial cells have an equally important role in nervous system function as their neuronal counterparts. The attributed roles of glia range from controlling neuronal cell number and axonal pathfinding to regulating synapse formation, function, and plasticity. *CG9426* knockout and knockdown lines exhibited defects in their mushroom bodies highlighting the importance of IPP and its fly ortholog in neurodevelopment.

ÖZET

CG9426'NIN ZİHİNSEL ENGELLİLİK İLİŞKİLİ IPP GENİNİN ORTOLOGU OLARAK KARAKTERİZASYONU VE *DROSOPHILA* SİNİR SİSTEMİNDE İFADE ÖRÜNTÜSÜNÜN ANALİZİ

Zihinsel engellilik algı ve öğrenmede aksama olarak tanımlanmakta ve dünya genelinde toplum %1-2'sini etkilemektedir. Zihinsel engelliliğe sebep olan pek çok sayıda ve karmaşık sebepler bulunmasına rağmen, etkilenen mekanizmalarda yöndeşme mevcuttur. Intracisternal A particle-promoted polypeptide (IPP) geni 584 aminoasit uzunluğunda bir BTB/POZ bölgesi, bir BTB/Kelch ile ilişkilendirilmiş BACK bölgesi ve 6 Kelch bölgesi tekrarı içeren IPP proteinini kodlamaktadır. Kelch protein ailesi 50 aminoasit uzunluğunda tekrarlayan Kelch bölgelerini içermeleriyle tanımlanmakta, bu bölgeler bir araya gelerek pervane benzeri bir yapı oluşturarak aktin organizayonunda görev almaktadırlar. Tanımlanan 63 Kelch protein ailesi üyesinden bazılarının zihinsel engellilikle ilişkisi kanıtlanmıştır. *Drosophila melanogaster* kısa yaşam süresi, çok sayıda yavru vermesi ve geliştirilmiş teknikler sayesinde genetik manipülasyonunun kolaylığıyla insan beyin hastalıklarının modellenmesinde birçok avantaj sağlamaktadır. CG9426, %37 özdeşlik ve %58 benzerlik paylaştığı için *IPP* geninin *Drosophila*daki ortologu olarak tanımlanmıştır. Bu projenin amacı *Drosophila melanogaster* modelini kullanarak *IPP*'nin nörogelişimdeki rolünü saptamaktır. Bu çalışmada, oluşturulan transgenik suşlarla *IPP* gen ifadesinin *CG9426* gen ifadesinin eksikliğinde meydana gelen düşük yaşama oranını ve mantarsı yapıdaki bozuklukları nasıl telafi ettiği gösterilmiştir. Bu sonuçlar *CG9426* ve IPP genlerinin fonksiyonel ortologlar olduğuna kanıt oluşturmakta ve *Drosophila melanogaster*in IPP'nin zihinsel engelliliğe nasıl sebep olduğunu anlamada model olarak kullanılabileceğini göstermektedir. Bu çalışmada ayrıca CG9426'nın beyindeki ifade örüntüsü analiz edilmiş ve larvalarda nöroblastlarda yetişkinlerde glia hücrelerinde üretildiği saptanmıştır. Glia hücrelerinin sinir sisteminde hücre sayısının ve akson yönbulumunu ve sinaps oluşumunu düzenlenmektedir. CG9426 mutantları mantarsı yapıda bozukluklar göstererek IPP geni ve sinek ortologu olan CG9426'nın nörogelişimdeki önemini vurgulamıştır.

TABLE OF CONTENTS

LIST OF FIGURES

LIST OF TABLES

LIST OF SYMBOLS

bp	Base Pair
kb	Kilobase
mL	Milliliter
ng	Nanogram
rpm	Revolutions per minute
µg	Microgram
µl	Microliter
µm	Micrometer
°C	Degree Celcius

LIST OF ACRONYMS/ABBREVIATIONS

APS	Ammonium Persulfate
CB	Central Brain
cDNA	Complementary DNA
CNS	Central Nervous System
DNA	Deoxyribonucleic Acid
GAN	Giant Axonal Neuropathy
GFP	Green Fluorescent Protein
ID	Intellectual Disability
IPP	Intracisternal A Particle-Promoted Polypeptide
MB	Mushroom Body
OP	Optic Lobe
PBS	Phosphate Buffered Saline
PCR	Polymerase Chain Reaction
PFA	Paraformaldehyde
RNA	Ribonucleic Acid
RNAi	RNA Interference
SDM	Site-directed Mutagenesis
SDS	Sodium Dodecyl Sulfate
TBCB	Tubulin Folding Factor B
TBS	Tris Buffered Saline
TEMED	Tetramethyl Ethylenediamine
UAS	Upstream Activating Sequence

UPS	Ubiquitin Proteosome System
VNC	Ventral Nerve Cord

1. INTRODUCTION

1.1. Intellectual Disability

According to the 5th edition of Diagnostic and Statistical Manual of Mental Disorders (DSM-5) of the American Psychiatric Association, Neurodevelopmental Disorders (NDD) were defined as conditions encountered during the developmental period that induce impairments and deficiencies in functioning (American Psychiatric Association, 2000). NDDs include intellectual disability (ID); autism spectrum disorder (ASD); attention-deficit/hyperactivity disorder (ADHD); neurodevelopmental motor disorders, such as tic disorders; communication disorders, and specific learning disorders (Morris-Rosendahl *et al*., 2022)

Intellectual disability (ID) is defined by intellectual functioning below average with additional limitations in adaptive functioning. ID can manifest as an isolated phenomenon or can be accompanied by malformations, neurological defects, impaired senses, seizures, and behavioral disturbances (American Psychiatric Association, 2000). ID affects around 1–3% of the population worldwide (Perou *et al*., 2013). Adaptive functions are evaluated under three major categories: conceptual, social, and practical. Conceptual functions involve reasoning, executive function, and problem solving; social functions encompass interpersonal communication and relationship whereas practical functions pertain to personal care and activities of daily living (Svenaeus, 2014). Mental abilities are assessed using intelligence tests such as the Weschler Scale Intelligence in Children, which includes verbal and non-verbal components. ID is diagnosed based on intellectual quotient (IQ) scores below 70. The severity of ID is categorized based on IQ scores: mild ID (51–70), moderate (36–49), severe (21–35) and profound (<20).

Intellectual disability can manifest as either isolated cognitive deficits or in conjunction with different symptoms and physical indicators, such as autism, epilepsy, anxiety, obsessive-compulsive disorder, and sleep disorders. These manifestations might include characteristic facial or body features, or structural abnormalities detected through

magnetic resonance imaging (Cox *et al*., 2017). Specific indicators associated with ID facilitate clinical diagnoses and contribute to the discovery of new genes related to ID through exome and genome sequencing. Some syndromes are more prevalent in specific populations and should be given priority in screening, such as Tay Sachs observed in Ashkenazi Jews and Bardet Biedl observed in Bedouin families (Katz and Lazcano-Ponce, 2008).

Previous studies related to this topic have revealed that the underlying causes of ID can often be multigenic. For instance, in the case of Rett Syndrome, affected patients have mutations in *MeCP2* genes. However, there are also various cases where mutations in *FOXG1* and *CDKL5* genes are responsible (Byun *et al*., 2015). Conversely, single gene mutations are known to give rise to diverse phenotypes, as seen in Fragile X Syndrome. Mutations in the Fragile X gene can result in the classic Fragile X Syndrome phenotype, but they can also lead to the Prader-Willi variant characterized by weight gain and increased appetite (McLennan *et al*., 2011).

Although there are various causes of ID, including metabolic disorders, endocrine dysfunction, and environmental exposure to toxins, genetic factors play a prominent role. An increasing number of genetic defects in individuals with ID have been revealed by numerous genome-wide techniques, such as comparative genomic hybridization and whole exome sequencing. Despite some milder cases where underlying causes remain unidentified, more than 528 genes have been found to cause ID, and over 1700 genes have been associated with ID in OMIM (Jansen *et al*., 2023).

1.2. Modelling Neurodevelopmental Disorders in Drosophila melanogaster

Due to limited knowledge about the genes affecting cognitive development, treatment for ID remains underdeveloped. *Drosophila melanogaster*, commonly known as the fruit fly, is one of the model organisms that aids in gaining a better understanding of the underlying genetic causes of ID (Mariano *et al*., 2020). Although flies are not so closely related to mammals from an evolutionary perspective, they still offer valuable insights. For example, the most common single-gene cause of ID, a mutation in the *FXS* gene, exhibited a positive

response to drug treatment with a metabotropic glutamate inhibitor that rescued the memory defect in *FXS* gene mutant flies (Bolduc, 2008).

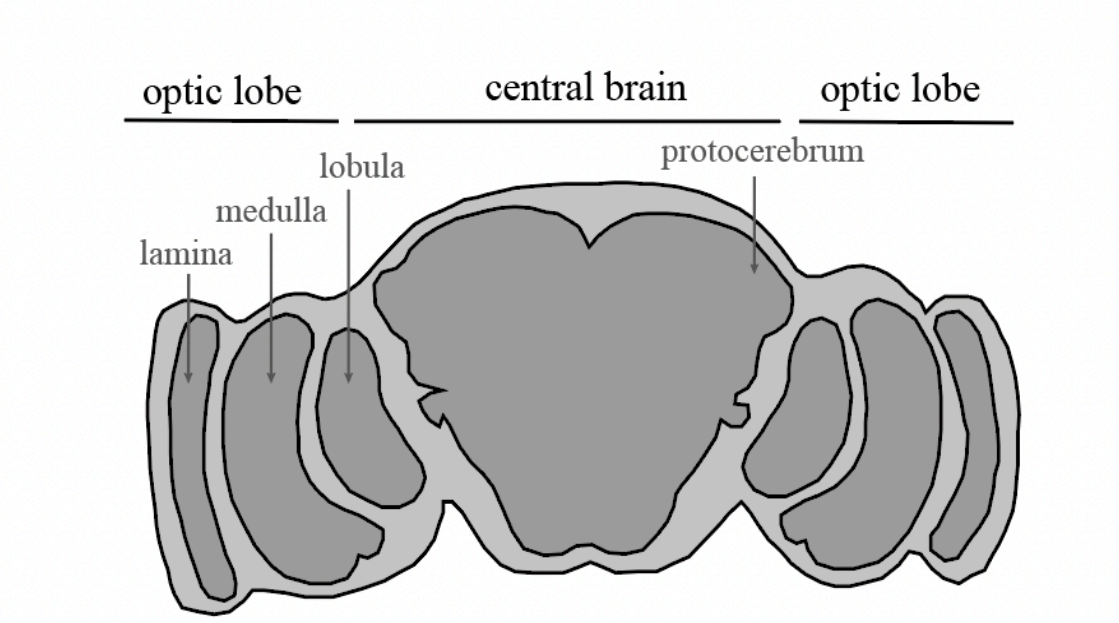

Figure 1.1. Structure of the *Drosophila* adult brain. The adult brain consists of the central brain and two optic lobes located on the sides. The internal region of the central brain is called protocerebrum. Optic lobes have three main subsections: lamina, medulla, and lobula.

The major components of the *Drosophila* central nervous system (CNS) include the optic lobes, central brain, and ventral nerve cord. The optic lobes reside on the sides of the central brain and are further divided into three main subregions: lamina, medulla, and lobula. The mushroom body, located in the dorsoventral region of the central brain serves as the olfactory learning and memory center for flies (Sousa-Nunes *et al.*, 2010).

1.3. Neuronal Stem Cells

Vertebrates and *Drosophila* show a significant parallelism between the temporal patterning mechanisms of brain development. Specific cell types emerge successively, and combinations of various transcription factors specify cell fates in both organisms. Hormones and signaling pathways, which are the associates of cell-extrinsic cues, also take part in temporal patterning. Neuronal diversity relies on temporal patterning mechanisms provided by sequentially produced cell types from progenitors (El Danaf *et al*., 2023).

In both mammals and flies, stem cells utilize different modes of proliferation to maintain the stem cell pool and generate specialized cells (Bello *et al*., 2008). In multicellular organisms, pluripotent stem cells are generated from totipotent cells. As development progresses, lineage potential gradually becomes restricted, eventually leading to the differentiation of tissue-specific multipotent stem cells (Eckfeldt *et al*., 2005).

Neural stem cells in the *Drosophila* CNS are called neuroblasts (NBs). NBs undergo proliferation during two major periods (Campos *et al*., 1985; Maurange *et al*., 2005). Initially, during the embryonic period, within the single-layered neuroectoderm, NBs undergo lateral inhibition (Egger *et al*., 2008). The polarity between the apical-basal axis and the alignment of mitotic spindles causes asymmetric division, giving rise to two morphologically different daughter cells (Jan *et al*., 2001; Knoblich *et al*., 2008; Chia *et al*., 2008). The larger daughter cell preserves the *Drosophila* neural stem cell division strategy, engaging in asymmetric division and self-renewal, while the smaller ganglion mother cell (GMC) undergoes a terminal division to generate neurons or glial cells. Following the completion of embryogenesis, the embryonic NBs' cell cycle halts, remaining inactive until proliferation is reinitiated at the larval development stage (Campos *et al*., 1985; Maurange *et al*., 2005; Kim *et al*., 2009). Postembryonic neuroblast are categorized into three main groups: optic lobe neuroblasts, which reside on the lateral surface of the central brain (CB); type I central brain neuroblasts located within the central brain and the ventral nerve cord (VNC), and type II neuroblasts, which are found on the dorsomedial surface of the two hemispheres (Saini *et al*., 2012; Figure 1.2).

1.4. Mushroom Body

Processing and storage of information are primary functions of brain. The proper functioning of the brain relies on the establishment of complex networks among different types of neurons. Mapping this cellular organization is important in understanding the molecular basis of specific brain functions, such as learning and memory (Rolls, 1987).

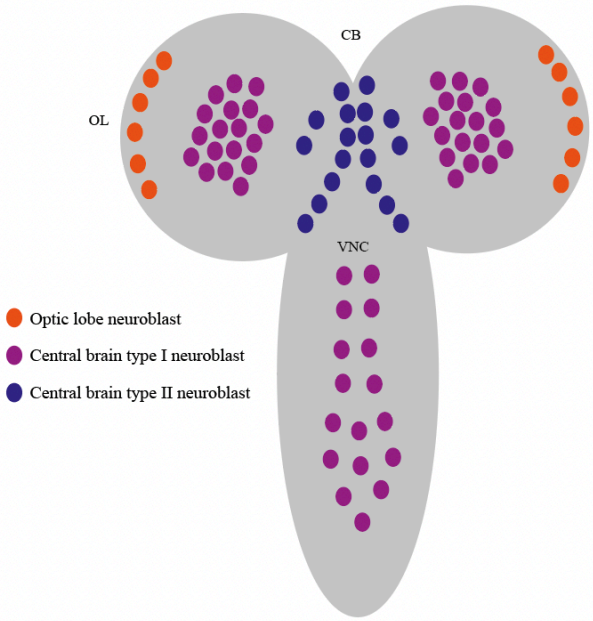

Figure 1.2. Schematic representation of neuroblast subtypes in third instar larva. Three main subtypes of neuroblasts are: optic lobe neuroblast (orange), central brain type I neuroblast (purple), central brain type II neuroblast (indigo) (Adapted from Saini *et al*., 2012).

Drosophila is a convincing model for neurodevelopmental studies. The mushroom bodies (MBs) are prominent structures in the *Drosophila* brain that are essential for olfactory learning and memory (Aso *et al*., 2009). The MB consists of intrinsic and extrinsic neurons. Intrinsic neurons are composed of Kenyon cells, whose cell bodies are situated in the posterior lateral region of the central brain of *Drosophila*. The dendrites of Kenyon cells form a structure called the calyx, whereas the axons of the Kenyon cells project to the dorsoventral region of the central brain, forming a structure called the peduncle. These axonal projections construct the MB α, α′, β, β′ and γ lobes (Aso *et al*., 2009; Technau *et al*., 1982).

A single MB neuroblast sequentially generates at least three types of morphologically distinct neuron types through asymmetric divisions (Technau and Heisenberg, 1982). Neurons projecting into the γ lobe of the adult MB emerge first, prior to the mid-3rd instar larval stage. Neurons projecting into the α′ and β′ lobes emerge between the mid-3rd instar larval stage and puparium formation. Finally, neurons projecting into the α and β lobes emerge after puparium formation.

Visualization of individual MB neurons has also revealed how different neurons acquire their characteristic axon projections (Ito *et al*., 1998). Axon projections of α′/β′ larval neurons are conserved during metamorphosis, while γ neurons diminish during metamorphosis and remain solely in the peduncle. Selective axonal pruning of widely branched MB neurons to the dorsal and medial lobes of the central brain occurs during puparium formation after the larval stage. This process results in the formation of three distinct axonal bundles which are called the γ lobe, the α′/β′ lobes, and the α/β lobes, respectively (Lee, 1999; Waddell *et al*., 2000; Tanaka *et al*., 2008).

The central complex in Drosophila MB comprises three major neuronal groups: tangential, columnar, and pontine neurons (Hanesch *et al*., 1989; Young *et al*., 2010). These neurons contribute to the formation of the central complex's main structures, namely the protocerebral bridge, the fan-shaped body, the ellipsoid body and the noduli (Hanesch *et al*., 1989). The ellipsoid body, situated as the most anterior component of this complex, is made up of four concentric rings. The fan-shaped body is composed of eight vertical and six horizontal segments. Positioned behind the fan-shaped body, the protocerebral bridge consists of sixteen segments. Lastly, the noduli are spherical structures located in the ventral region of the ellipsoid body (Hanesch *et al*., 1989; Renn *et al*., 1999).

MB development is tightly regulated by neurodevelopmental genes (Crittenden *et al*., 2018). Loss-of-function and gain-of-function studies are conducted with the orthologs of ID-causing genes in *Drosophila*. These studies have revealed the presence of morphological defects, such as loss or fusion of α, β, and γ lobes due to axon guidance or pruning defects (Michel, 2004; Chubak *et al*., 2019; Kim *et al*., 2021; Yu *et al*., 2014), as well as variations in axon volume resulting from dysregulations in Kenyon cell neuroblast proliferation and differentiation (Crittenden *et al*., 2018).

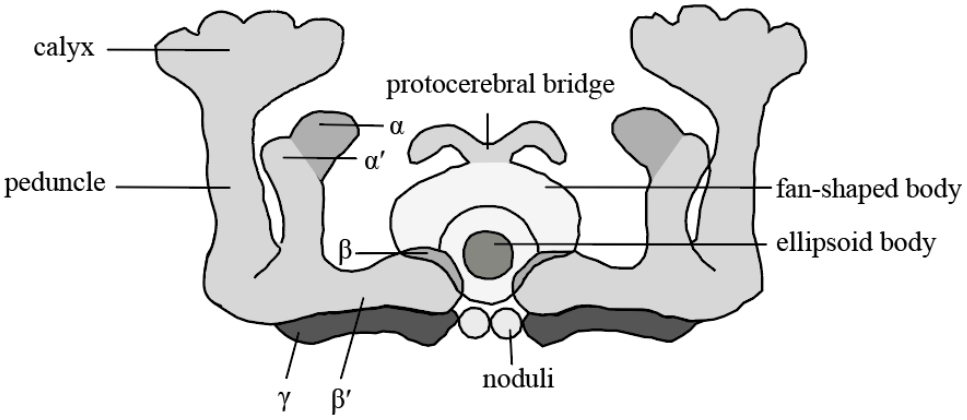

Figure 1.3. Structure of the mushroom body and the central complex. Cell bodies of Kenyon cells reside at posterior lateral region and form the calyx. Axon bundles of these cells project to the dorsoventral region through the peduncles to form three distinct lobes: α/α', β/β' and γ. The central complex consists of the protocerebral bridge, the fan-shaped body, the ellipsoid body, and the noduli (Adapted from Hanesch *et al*., 1989).

1.5. Role of Glial Cells in Neurodevelopment

The neural machinery that affects information processing and underlies ID can involve malformed neuronal networks and defects that result in poor brain plasticity. Neuropathological studies of post-mortem brains from individuals with ID have revealed distinct alterations in their cerebral cortex, hippocampus, and other brain regions (Dierssen and Ramakers, 2006).

Neurons form remarkable circuits with each other, capable of conveying information through the generation of action potentials via rapid changes in their membrane potential (Senatore *et al*., 2016). This transformation relies on the expression of voltage-gated sodium and potassium channels. The fundamental molecular mechanisms responsible for these fundamental neuronal features are evolutionarily conserved (Varoqueaux, 2017).

On the other hand, glial cells represent the other major component of the nervous system, outnumbering neurons in the mammalian brain. However, they remained less conspicuous until recent years. Glial cells do not function by altering their membrane

potential like neurons, but they interact with neurons and are crucial for proper neuronal functioning (Herculano-Houzel, 2014).

The interdependent mechanisms between neurons and glia complicate the elucidation of the exact contribution of glia in neurological manifestations. There are different subtypes of glial cells in the mammalian CNS, each playing a distinct role. The three main subtypes of CNS glia are astrocytes, oligodendrocytes, and microglia (Purves *et al*., 2001).

Astrocytes were previously considered as inactive supportive cells for neurons. However, it is now known that astrocytes play a more active role in various brain functions (Ransom *et al*., 2003). They participate in regulating and recycling neurotransmitters, maintaining the blood-brain barrier, managing metabolism, providing structural support, and engaging in gliotransmission, which involves direct communication with neurons and other glial cells (Ullian *et al*., 2004; Wong, 2019). By supplying essential nutrients to the brain, they contribute to energetic homeostasis (Olsen *et al*., 2015). Astrocytes also play a role in terminating synaptic signals to prevent excitotoxicity. Furthermore, they are responsible for maintaining ionic homeostasis, which directly affects neuronal excitability. Astrocytes participate in cell signaling by releasing gliotransmitters (Olsen *et al*., 2015). Considering their wide range of functions, malfunctions in astrocytes can lead to neurological disorders (Wong, 2019).

Microglia function as the macrophages of the central nervous system, mediating innate and adaptive immune responses in the CNS in the cases of infections, neurodegenerative diseases, or injury (Schafer and Stevens, 2015). Unlike other glial cells, microglia originate from the mesoderm not the neuroectoderm. Their primary roles include removing cellular debris and secreting chemokines and cytokines to initiate immune responses in the CNS. Additionally, they influence brain development by controlling neurogenesis, synaptic maturation, neuronal migration, and branching (Schafer and Stevens, 2015).

Oligodendrocytes constitute the third major subtype of glial cells in the CNS. They play a direct role in white matter development and maintenance by forming myelin sheaths to insulate axons (Zhang *et al*., 2016). This insulation facilitates robust conduction of action potential signaling along the white matter. Oligodendrocytes and myelin are not uniformly

distributed throughout the brain, indicating that oligodendrocytes have varied roles in moderating brain function and neuronal networks (de Hoz and Simons, 2015; Dimou and Simons, 2017). Dysfunction or degeneration of oligodendrocytes is a hallmark feature of demyelinating or dysmyelinating diseases, such as multiple sclerosis, which often presents cognitive impairment in addition to more classic focal neurological deficits (Wong, 2019).

Conventional research on synaptic functioning used to primarily focus on neurons; however, an increasing number of studies have shifted their perspectives towards glia, particularly astrocytes in this context, as they exhibit strong structural and functional interactions with synapses. Recent genetic studies have unveiled the potential contributions of astrocytes to the pathophysiology of nervous system disorders (Wong, 2019).

1.6. Glia in *Drosophila*

Glial cells are crucial components of the nervous system that are evolutionarily conserved. The functionality of the brain demands the collaboration of both neurons and glial cells especially due to their complex interactions. *Drosophila* serves as a widely used model organism with a relatively low number of glial cells which have been extensively characterized. The availability of well-defined promoter elements that can drive Gal4, LexA, Flp, or Cre in specific glial subtypes allows for satisfactory manipulations and spatiotemporal specific resolution (Germani *et al*., 2018). While some glial cell types are specific to flies, they share concrete molecular and functional similarities with their human counterparts, making flies a perfect model to identify core principles for mammalian glial development and function (Bittern *et al*., 2021).

In the fly nervous system, glial cells constitute only 10% of the total cell population. They are divided into three major groups: surface, CNS, and wrapping glial cells (Yıldırım *et al*., 2019). The nervous system is metabolically isolated from the rest of the body by the blood-brain barrier. In Drosophila, this barrier between the brain and the hemolymph is formed by two subgroups of surface glia known as perineurial glial cells and subperineurial glial cells. Cortex glia can be seen as a connection between mesh of neurons called neuropile and subperineurial glia that constitute the blood-brain barrier. Cortex glia emerge during larval stages under the regulation of insulin receptor signaling and the EGF receptor

Heartless. There are two subgroups of neuropil-associated glia: ensheathing glia and astrocyte-like glia. While astrocytes are the most abundant glial cell type in vertebrates, the fly's central nervous system includes only a small number of them (Stork *et al*., 2014).

Similar to their vertebrate counterparts, astrocyte-like glial cells in *Drosophila* also possess gap junctions and numerous protrusions that exude into the neuropil region in order to regulate neurotransmitter homeostasis (Muthukumar *et al*., 2014; Stork *et al*., 2014; MacNamee *et al*., 2016; Peco *et al*., 2016). However, unlike in vertebrates, astrocytic processes often remain at a distance from synaptic sites, suggesting that tripartite synapses might not be present in flies (MacNamee *et al*., 2016; Stork *et al*., 2014). Astrocyte-like glial cells play a role in the moderating synaptic plasticity (Muthukumar *et al*., 2014). Additionally, they are involved in activating Draper expression and scavenging neuronal debris during metamorphosis (Tasdemir-Yilmaz and Freeman, 2014).

Neurotransmitter homeostasis is provided by the expression of specific transport proteins by *Drosophila* astrocyte-like glial cells such as the excitatory amino acid transporter 1 (EAAT1). The expression of EAAT1 requires Notch-mediated glia-neuron interaction. Additionally, the GABA transporter (GAT) and octopamine/tyramine receptors are involved in this process (Soustelle *et al*., 2002; Muthukumar *et al*., 2014; Stork *et al*., 2014). EAAT1 also functions as a chloride channel, contributing to ionic homeostasis in the neuropil region for astrocyte-like glial cells (Parinejad *et al*., 2016). GAT can be endocytosed in response to an increase in intracellular Ca^{2+} concentration in astrocyte-like glial cells which would inhibit the neuronal activity (Ma *et al*., 2016; Zhang *et al*., 2017).

Furthermore, astrocyte-like glial cells have been identified to play a role in controlling sleep behavior through the release of gliotransmitter Noktochor and the expression of a cytokine called Eiger, which activates the Wengen receptor on neurons (Sengupta *et al*., 2019; Vanderheyden *et al*., 2018). In short, astrocyte-like glial cells in *Drosophila* serve an essential role in modulating neuronal activity.

The ensheathing glial cells enshroud the whole neuropil region and act as an extra barrier between the neuropil and cortex regions. They also serve a neuromodulatory function, such as sulfite detoxification (Otto *et al*., 2018). Initially, there are four ensheathing

glial cells present in larval hemisegments. During metamorphosis, some of these glial cells disappear while the remaining ones can proliferate and redifferentiate, ultimately becoming adult neuropil-interacting glial cells. These neuropil-interacting glial cells emerge from Type III neuroblasts (Omoto *et al*. 2015; Kremer *et al*., 2017).

The ensheathing glia establish a glutamine gradient in the neuropil. Similar to astrocyte-like glial cells, ensheathing glial cells also express transporters like EAAT2, which transports taurine and plays a role in sleep dynamics (Besson *et al*., 2005; Peco *et al*., 2016; Stahl *et al*., 2018). While astrocyte-like glial cells acquire their phagocytic capability through circuit remodeling (Muthukumar *et al*., 2014; Tasdemir-Yilmaz and Freeman, 2014), ensheathing glial cells express key components of the glial phagocytic machinery such as the engulfment receptor Drpr and dCed-6. These components respond to injury and phagocytose degenerated axons in case of brain injury (Doherty *et al*., 2009; Hilu-Dadia *et al*., 2017).

1.7. Intracisternal A Particle-Promoted Polypeptide

A report published in 2019 on WES and WGS studies conducted with 404 consanguineous families aimed to reveal possible genetic causes of autosomal recessive intellectual disability (ARID) (Hu *et al.*, 2019). Among 219 families, potential disease-causing variants were identified in 77 known and 77 novel candidate ARID genes, 21 X-linked genes and 9 genes previously reported in other diseases (Hu *et al.*, 2019). One of the novel candidate ARID genes, Intracisternal A Particle-Promoted Polypeptide (IPP), was discovered through WES analysis of two independent Iranian families with consanguineous marriages.

The first family (M8800158) resides in Kerman, Iran, and consists of one female and one male individuals with ID who had a 5 kb deletion on 20 Mbp conserved homozygous region, which also includes IPP gene. Although they were born through unproblematic deliveries, they exhibited delays in psychomotor activities such as walking and speaking. Individual IV:3 experienced seizures during infancy, which could be controlled with medication. Individuals IV:1 and IV:3 displayed aggressive behavior. Their hearing and vision were normal, and they could follow basic commands, count money, and control their

excretory systems after the age of 5. At ages 32, 29, and 15, their heights were measured as 177 cm, 163 cm, and 165 cm, respectively. They had micrognathia, and individual IV:1 and IV:2 had a significant aquiline nose, while individual IV:3 had prognathism and a significant aquiline nose. Although their speech was characterized by mumbling, they did not have any walking defects. The IQs of individuals IV:1, IV:2, and IV:3 were measured as 36, 35, and 38, respectively.

The second family (M8900206), located in the southwest of Iran in Bushehr, had four individuals with ID, all of whom shared a common missense mutation that resides on the 3rd Kelch domain. They were born during the neonatal period after abnormal pregnancies. These individuals also exhibited delays in psychomotor development. There were no auditory or vision impairments, and they could follow basic commands, count money, and control their excretory systems after the age of 8. At ages 40, 33, and 29, their heights were measured as 150 cm, 172 cm, and 151 cm, respectively. They had micrognathia and significant aquiline noses. They could walk normally and form short sentences. While individual IV:1 and IV:2 had significant aquiline noses, individual IV:3 had prognathism and a significant aquiline nose. The IQs of individuals IV:1, IV:2, and IV:3 were measured as 40, 45, and 49, respectively (Hu *et al*., 2019).

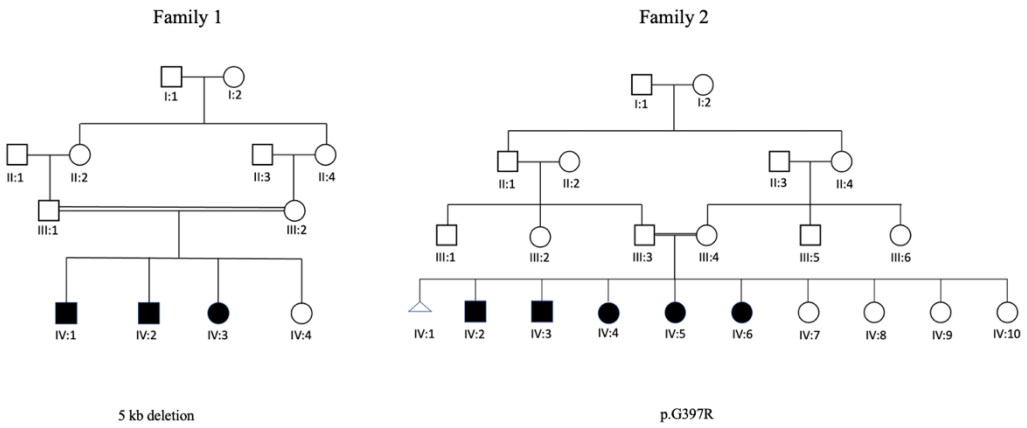

Figure 1.4. Family trees of Iranian ID patients that have mutations in the IPP gene. Family 1 has 3 individuals, all of them have a 5 kb deletion that included the IPP gene region. 4 members of family 2 have a point mutation that results in an amino acid change in the 1189th position (p.G397R) (Adapted from Hu *et al*., 2019).

The IPP cDNA comprises a 1752 bp long open reading frame that encodes a protein of the same name (Figure 1.5). The IPP protein spans 584 amino acids and has a molecular weight of 66 kDa. It is composed of a BTB domain, a BTB Kelch associated BACK domain, and six repetitive Kelch domains (Kim *et al*., 1999).

Figure 1.5. The genomic region of IPP and the structure of the IPP protein. Human IPP gene is 1752 bp long and has 8 exons. This gene encodes for a 584 amino acid long protein IPP. IPP has a BTB domain, a BACK domain and 6 repetitive Kelch domains.

IPP exhibits actin-binding activity mediated specifically by the kelch repeat domain (Kim *et al*., 1999). The BTB domain is found in zinc finger proteins and kelch proteins, and it plays a role in a wide variety of biological processes, including transcription regulation, cytoskeletal arrangement, ion conductance, and protein ubiquitination (Stogios *et al*., 2005). Kelch domains assemble to create a β-propeller structure that frequently interacts with actin filaments (Adams *et al*., 2000). In Figure 1.6, the predicted 3D structure of IPP is shown, with the BTB domain located at the N-terminus and the Kelch repeats forming a propeller-like structure at the C-terminus (Stogios *et al*., 2005).

The first family exhibited a significant 5 kb deletion that encompasses the coding region, while the second family carried a point mutation converting G to A on the 1189th position of IPP (Hu *et al*., 2019). In order to gain a deeper understanding of the disease's pathogenesis, both mutations were replicated in this study using *Drosophila melanogaster* as a model organism. The 5 kb deletion likely results in a complete loss-of-function. Thus, a mutant for the *Drosophila* homolog of IPP, CG9426, was generated. Additionally, flies carrying the pG397R mutation corresponding to the 3rd Kelch Domain of IPP were also

generated. As illustrated in Table 1.1, the mutated site located within the 3rd Kelch Domain of IPP is conserved across various species.

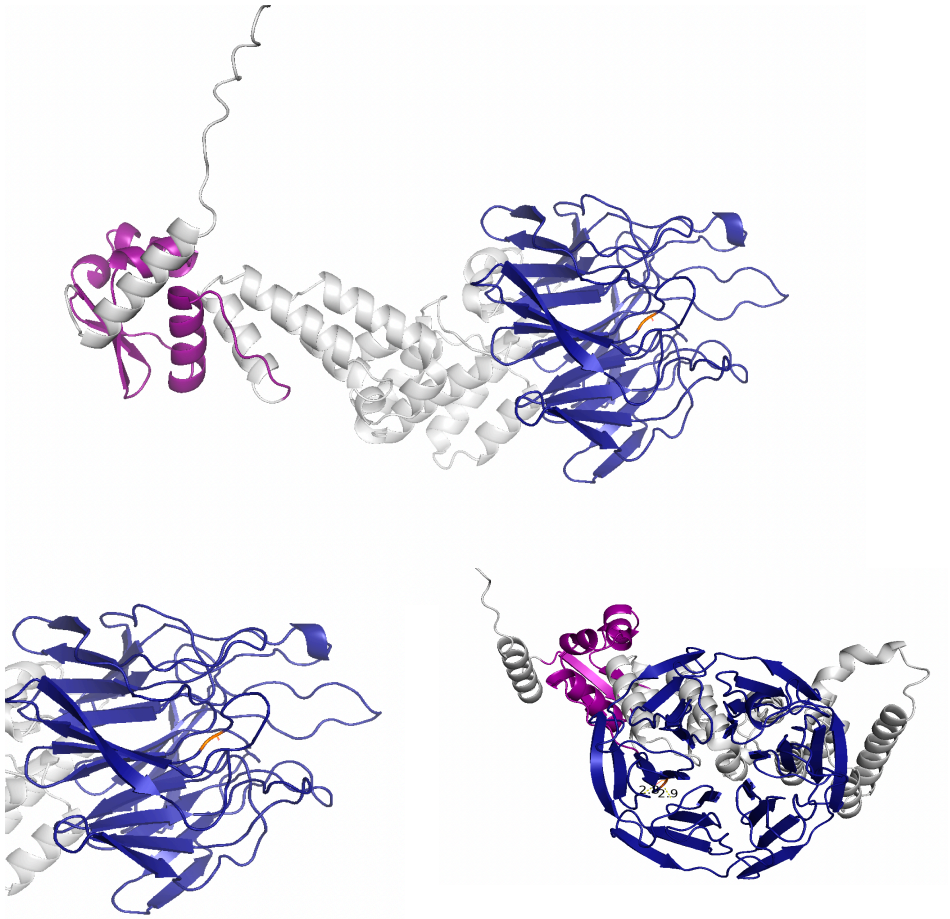

Figure 1.6. Predicted 3D Structure of IPP by PyMol. Region highlighted with pink shows the BTB domain and regions highlighted with dark blue show the Kelch domains. Kelch repeats come together and form the propeller structure. On the 3rd Kelch domain site of mutation p.G397R which is modeled in this study is shown with yellow.

1.8. Kelch Protein Superfamily

The kelch motif was initially defined as a sixfold tandem element in the sequence of the *Drosophila* Kelch ORF1 protein. Repetitive kelch motifs form a conserved β-propeller structure that appears in various polypeptide contexts and provides different protein–protein interaction sites (Adams *et al*., 2000). Members of the Kelch-like gene family encode

proteins that have three distinct domains: the bric-a-brac, tramtrack, broad (BTB) domain, the BACK domain, and five to six repetitive Kelch domains (Shi *et al*., 2019). There are 65 identified members of this family with diverse roles in F-actin organization, stabilization, crosslinking, and cytoskeleton modulation. They are also known for forming complexes through interactions with Cullin3, an E3 Ubiquitin ligase (Adams *et al.*, 2000).

Numerous members of this Kelch protein family play a role in neurodevelopment. Some examples include KLHL1 and KLHL20. KLHL1, an actin-binding protein expressed in neurons, is recognized for controlling calcium channel density by interacting with actin and inducing biophysical changes (Aromoloran *et al.*, 2012). KLHL20, on the other hand, forms a complex with Cul3-RING E3 ubiquitin ligase, participating in protein ubiquitination. KLHL20 serves as an adaptor for substrate recognition by the E3 ligase Cullin3 and contributes to the regulation of neurite outgrowth and synaptic development. *De novo* missense variants of KLHL20 have been identified as causative factors in neurodevelopmental disorders (Sleyp *et al.*, 2022).

Table 1.1. Amino acid sequence of the mutated domain of IPP in Family 2 members across different model organisms. The presence of two consecutive glycines is a hallmark of kelch domains. The first glycine on the 3rd Kelch Repeat is highlighted in yellow. The mutated region is conserved among species.

Species	Gene	Kelch Domain 3
Human	*IPP*	**RCGLGVCVC--YGAIYALGGWVGAEIGN--TI------ERFD------PDENKWEVVGNMA**
Mouse	*Ipp*	**RCGLGVCVC--YGAIYALGGWVGAEIGN--TI------ERFD------PDENKWEVVGSMA**
Rat	*Ipp*	**RCGLGVCVC--YGAIYALGGWVGAEIGD--TI------ERFD------PDENKWEVVGNMA**
Zebrafish	*ipp*	**RCGVGVCSC--HGALYALGGWIGSEIGK--TM------ERYD------PEENKWEVIGSMA**
Fruit fly	*CG9426*	**RCEFGLCTM--GGNLFAVGGWIGDDIGG--SM------ECYD------PEQDLWKLMGSMP**

p.G397R

1.9. Cullin3

Ubiquitination is involved in nearly all life activities of eukaryotes. E3 Ubiquitin Ligases constitute a broad family of enzymes responsible for catalyzing the ubiquitination process, transferring the ubiquitin protein to the target substrate. They form a three-enzyme cascade alongside ubiquitin-activating enzyme E1 and ubiquitin-conjugating enzyme E2 (Yang *et al*., 2021).

Cullin3 is an E3 Ubiquitin Ligase that has been reported to interact with 66 BTB domain containing proteins, including IPP (Kouranti *et al*., 2022). *De novo* mutations in Cullin3 have been shown to cause autism spectrum disorder (ASD). Furthermore, Cullin3 mutations have been associated with motor deficiencies, social and cognitive impairments, attention deficit hyperactivity disorder (ADHD), schizophrenia, ID, sleep disturbances, and epileptic seizures in both humans and mouse models (Codina-Sola, 2015; Redin, 2017; da Silva Montenegro, 2019; Nakashima, 2020). In 2021, Morandell and colleagues demonstrated that Cullin3 modulates neuronal migration by regulating the amount of Plastin3 (Pls3). Pls3 functions cell autonomously, controlling cell migration by moderating actin cytoskeleton organization oriented to neural migration (Morandell *et al*., 2021). More recently, it was discovered that Cullin3 is required for the aPKC kinase-dependent Numb localization during the asymmetric division of *Drosophila* neural stem cells (Rives-Quinto *et al*., 2020). Actinfilin, another synaptic member of Kelch proteins known to bind to the actin cytoskeleton, has also been found to interact with Cullin3 and regulate the degradation of glutamate receptor GluR6 in neurons (Salinas *et al*., 2006). These studies underscore the importance of Cullin3 and its interactors in brain development and processes such as neural migration regulation.

1.10. CG9426

CG9426 is recognized as the fly ortholog of IPP, sharing 37% sequence identity and 58% similarity. It achieves a score of 13 out of 15 for orthology in DIOPT. The *CG9426* gene is located on the 2nd chromosome of flies and encodes for a 627-amino acid protein (Alliance of Genome Resources, 2023). According to public RNASeq data, it is primarily expressed in the embryonic/larval muscle system and embryonic/larval somatic muscle cell (FlyBase, 2023). Predicted to possess actin-binding activity due to its 6 Kelch domains, it is also projected to participate in protein ubiquitination because of its BTB domain. All interacting partners of CG9426 were identified using the two-hybrid method, except for Cul3 (FlyBase, 2023). Prior to this project, there were no studies related to the elucidation of the function of CG9426.

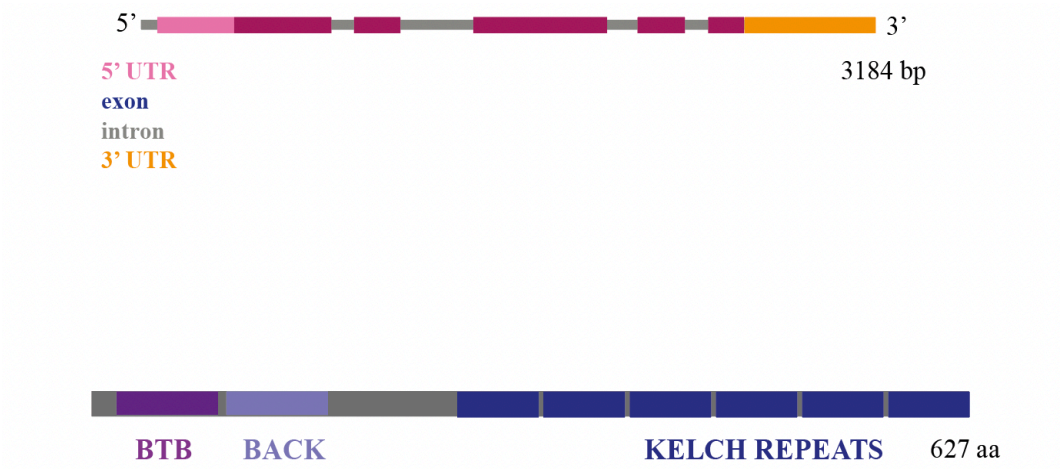

Figure 1.7. The genomic region of *CG9426* and protein structure. The *CG9426* gene spans 3184 bp and is composed of 5 exons. This gene encodes for a 627-amino acid protein, featuring a BTB domain, a BACK domain and 6 repetitive Kelch domains.

1.11. CRISPR Mediated Integration Cassette

As emphasized above, *Drosophila* is a preferable model organism in many aspects due to availability of versatile tools that ease gene editing. The UAS-Gal4 system is a bivalent system widely used in genetic studies. Gal4 recognizes the DNA sequence UAS (Brand *et al*., 1994). In 2015, a T2A-Gal4 technology called Trojan Gal4 was developed. Trojan Gal4 is based on the integration of a cassette that includes *SA-T2A-GAL4-polyA* (polyadenylation signal) in coding introns of genes (Gnerer *et al*., 2015; Diao *et al*., 2016). The *polyA* will arrest transcription of the gene and generate a truncated protein from gene in which the cassette is inserted. *T2A* is a viral ribosomal skipping site that arrests translation, and the Gal4 protein remains untagged after the site (Diao and White, 2012). *T2A-GAL4* enable the determination of expression patterns by using UAS-GAL4 system.

CRISPR Mediated Integration Cassette system is integration of this cassette system into the intronic region of the gene of interest by CRISPR method. sgRNAs target the CDS introns to integrate the cassette by a homology directed repair mechanism. There are different CRIMIC constructs designed by the Bellen Lab. In this study pM37 construct was used. In addition to the SA,T2A, GAL4 and polyA sites this construct also includes: two ϕC31 *attP* sites that can be utilized for replacing the integrated cassette with various cassettes containing two *attB* sites through Recombinase Mediated Cassette Exchange (RMCE), two

FRT sites at the two ends of the cassette to enable reversion of the integration by using FLP-FRT system, and a 3xP3-GFP site to track the presence of cassette by following the GFP expression on the eyes (Bateman *et al*., 2006; Kanca *et al*., 2017) (Figure 1.8). With the CRIMIC construct, it is also possible to conduct rescue experiments, structure-function analyses, and to observe whether the phenotypes can be reverted with an integrated transgene carried by *UAS*-cDNA for the gene of interest (Bellen and Yamamoto, 2015).

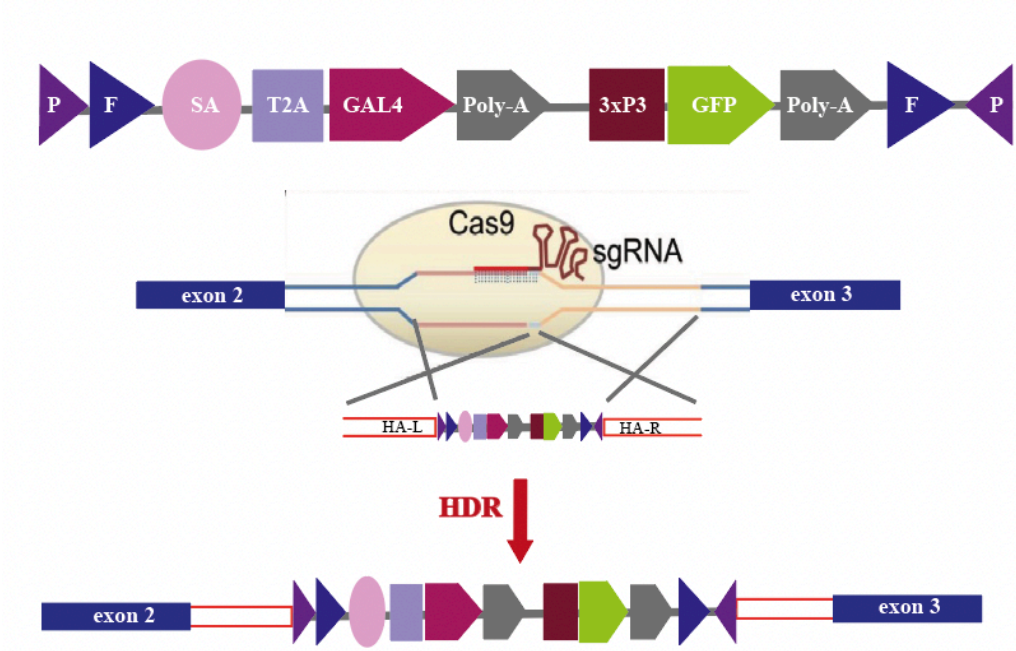

Figure 1.8. Structure of the CRIMIC pM37 construct and integration strategy. The CRIMIC cassette is integrated into the intronic region of the target gene using the CRISPR method. The cassette comprises two attP sites (P), two FRT sites (F), a Splice Acceptor site (SA), a T2A-GAL4 site followed by a poly-A and a GFP sequence downstream of 3xP3 promoter, followed by another polyA.

1.12. RNA Interference

The concept of RNA interference (RNAi) was first identified in the *C. elegans.* RNAi induces sequence-specific gene silencing through the formation of double-stranded RNA (dsRNA) (Fire *et al*., 1998). It was discovered that sense RNA is as effective in disrupting gene expression as antisense RNA, and the mixture of dsRNA containing both sense and

antisense RNA was observed to have at least a tenfold greater potential for silencing (Guo *et al*., 1995; Fire *et al*., 1998).

RNAi is a frequently used genetic tool for loss-of-function studies. Introduction of dsRNA into cells activates Dicer2, a ribonuclease that cleaves dsRNA into small interfering RNA (siRNA). These siRNA fragments are then guided by Argonaute 2 (Ago 2) to associated proteins, forming the RNA-Induced Silencing Complex (RISC). Subsequently, the sense strand of siRNA is degraded, whereas the antisense strand induces the cleavage of complementary mRNA via Ago2 leading to gene silencing (Zhu *et al*., 2020).

In addition to the siRNA pathway described above, there are also piwi interacting RNA (piRNA) and microRNA (miRNA) pathways that function in suppressing the expression of target genes (Zhu *et al*., 2020).

In *Drosophila*, gene silencing can be achieved by producing transgenic flies expressing hairpin RNA or by the RNAi method involving dsRNA injection into the germ line of the flies (Czech *et al*., 2011). Previously, long hairpin RNAs were found to be ineffective in gene silencing. An artificial microRNA called short hairpin RNA (shRNA) was designed enhanced effectiveness (Ni *et al*., 2011).

2. AIM OF THE STUDY

Intellectual disability (ID) is characterized by a general deficiency in cognition and learning, affecting approximately 1-2% of the global population. While the underlying causes of ID are numerous and complex, certain mechanisms appear to be commonly affected, including chromatin modification and transcriptional regulation, signal transduction, synaptic function, metabolism, cytoskeleton dynamics, and the ubiquitination system.

In this context, two distinct Iranian families with consanguineous marriages presented individuals with ID. WES data from these individuals revealed a shared mutation in a common gene known as Intracisternal A particle-promoted polypeptide (IPP).

IPP encodes a 584-amino acid long protein that includes a BTB/POZ domain, a BTB/Kelch associated domain, and 6 Kelch-repeat domains. The kelch protein family, characterized by a repetitive motif of 50-amino acid motif, is essential for maintaining actin organization. The Kelch superfamily comprises 63 identified members, some of which have been associated with intellectual disability.

In flies, IPP shares a sequence-similarity-based ortholog called CG9426. This study aims to validate the functional orthology between IPP and CG9426, analyze the morphological consequences of CG9426 loss of function in *Drosophila melanogaster*, analyze its expression in the nervous system, and thus broaden our understanding of IPP and its role in neurodevelopment.

3. MATERIALS

3.1. Biological Materials

All fly lines used in this study are listed in Table 3.1.

Table 3.1. List of fly lines.

Name	Chr. No.	Description
Actin-Gal4	2	Expresses Gal4 protein in post-mitotic neurons under the control of *actin*
longGMR-Gal4	2	Expresses GAL4 in the eye under the control of five copies of a 38 bp glass (gl) binding site.
CG9426-Gal4	3	Expresses Gal4 protein under the control of the putative promotor sequence of *CG9426*
$CG9426^{CRIMIC}$	2	CRISPR-based insertion of a CRIMIC cassette results in expression of GAL4 under CG9426 control
Elav-Gal4	2	Expresses Gal4 protein in post-mitotic neurons under the control of *elav*
Repo-Gal4	2	Expresses Gal4 protein in glia under the control of *repo*
Alrm-Gal4	3	Expresses Gal4 protein in astrocyte-like glia cells under control of *alrm*
UAS-nlacz	3	Expresses nuclear localized beta-galactosidase under the control of UAS sequences

Table 3.1. List of fly lines. (cont.)

Name	**Chr. No.**	**Description**
UAS-IPP^{wt}	3	Expresses HA-tagged wild type IPP under the control of UAS sequences
UAS-IPP^{G397R}	3	Expresses HA-tagged mutated IPP under the control of UAS sequences
UAS-CG9426^{RNAi}	3	Expresses shRNA for RNAi of CG9426 under the control of UAS sequences
BL36303	3	3rd chromosome attP docking site for phiC31 integrase-mediated transformation.
Df(2L)	2	Isogenic deficiency stocks created by FLP-induced recombination between FRT-carrying transgenic insertions; molecularly defined deletion endpoints correspond to initial location of the progenitor insertions.
Dp(2;3)	3	Interchromosomal duplications tiling the majority of the second and third chromosomes from *Drosophila melanogaster.*
BAC^{99C18}	3	Bacterial Artifical Chromosome that includes CG9426 genomic region integrated to the 3rd chromosome
yw	1	Flies carrying a deletion mutation in their w genes
ywQB		General balancer stock with the genotype of *yw; Sp/CyO; TM2, Ubx/TM6B, Tb, Hu*

3.2. Chemicals and Equipment

3.2.1. Chemicals

List of the chemicals that were utilized in this study and their manufacturers are given in Table 3.2.

Table 3.2. List of chemicals.

Chemical	Manufacturer
1 kb marker	NEB, USA (N3232L)
100 kb marker	NEB, USA
Agarose	VWR, USA
Bovine Serum Albumin	Sigma-Aldrich, USA (A9647)
EDTA	Sigma-Aldrich, USA (59417C)
Ethidium Bromide	Sigma Life Sciences, USA (E1510)
Isopropanol	Sigma-Aldrich, USA (W292907)
KOAc	Sigma-Aldrich, USA (A2056)
NaCl	Sigma-Aldrich, USA (S7653)
Paraformaldehyde	Sigma-Aldrich, USA (P6148)
Phenol:chloroform:Isoamyl alcohol	Sigma-Aldrich, USA (P2069)
Proteinase K	Roche, Germany (139963000)
Triton-X 100	AppliChem, USA (A4975)
Tween 20	Roche, USA (11332465001)

3.2.2. Buffers and Solutions

List of the buffers that were utilized in this study and their ingredients are given in Table 3.3.

Table 3.3. List of buffers and their contents.

Buffer	**Ingredients**
PBS	137 mM NaCl 2.7 mM KCl 10 mM Na2HPO4 1.8 mM KH_2PO_4
PBS-T	PBS (1x) 0.3% Triton X-100
PFA	160 g/l PFA, pH 7.4 1M NaOH until solution becomes transparent
PAXD	50 g BSA 3 g Sodium Dexoycholate 0.3% Triton X-100 In PBS
RIPA BUFFER	10 mM Tris-HCl pH= 8.0 1 mM EDTA 0.5 mM EGTA 1 % Triton X 0.5 % SodiumDeoxycholate 0.2 % SDS 140 mM NaCl 1 mM PMSF Protease inhibitor cocktail

Table 3.3. List of buffers and their contents. (cont.)

Buffer	**Ingredients**
Running Buffer (10 X)	29 g Tris-Base 144 g Glycine 10 g SDS up to 1000 ml dH_2O
Transfer Buffer (25 X)	36.4 g Tris-Base 180 g Glycine up to 1000 ml dH_2O
TAE Buffer	40 mM Tris-Cl 1 mM EDTA 0.1% Acetic acid
TBS (0.1 M)	12.1 g Tris-Base 0.2 g KCl 8 g NaCl up to 800 ml dH_2O
TBS-T	TBS (1X) Tween-20

3.2.3. Primers

List of primers and their sequences that are used in cloning experiments of this study is given in Table 3.4.

Table 3.4. List of primers.

Name	Sequence in 5' to 3' direction
IPP-F	CACCATGGCTAATGAGGACTGTCCCAAGG
IPP-R	AAGATTAAAAATCCCCTTTGTTAGAGTCTTGTGAT
IPPsdmF	CTTTGGGTAGATGGGTTGGAGCTG
IPPsdmR	CAACCCATCTACCCAAAGCATAGATAGCC
IPPattbF	GGGGACAAGTTTGTACAAAAAAGCAGGCTCACCATG GCTAATGAGGA
IPPattbR	GGGGACCACTTTGTACAAGAAAGCTGGGTCAAGATT AAAAATCCCCTTTGTTAGAG

3.2.4. Bacterial Strains

Bacterial strains that are used as competent cells in transformation are listed in Table 3.5.

Table 3.5. Bacterial strains.

Strain	Origin	Application
DH5α	*E.coli*	General cloning
Stbl3	*E.coli*	Cloning unstable inserts
Db3.1	*E.coli*	Cloning vectors with ccdB site

3.2.5. Vector Constructs

Vector constructs utilized in this study are listed in Table 3.6.

Table 3.6. List of plasmids.

Vector	Application	Antibiotic
pDONR207	Donor vector for Gateway BP Cloning	Gentamycin
pUASg::HA	Expression vector for Gateway LR Cloning	Ampicillin
pLEX307	Expression vector for Gateway LR Cloning	Ampicillin
psPAX2	2nd generation lentiviral packaging plasmid	Ampicillin
VSVG	Envelope protein production for lentiviral particles	Ampicillin

3.2.6. Antibodies & Dyes

Dyes used in Western Blot are listed in Table 3.7. Primary and secondary antibodies that are used in immunohistochemical and Western Blot experiments are listed in Table 3.8.

Table 3.7. List of dyes.

Dyes			
Name	**Target**	**Dilution**	**Source**
Alexa Fluor 647 conjugated Phalloidin	F-Actin	1:1000	Invitrogen
DAPI	Nucleus	1:1000	Invitrogen

Table 3.8. List of antibodies.

Name	Antigen	Host	Dilution	Source
Primary Antibodies				
Anti-Elav	Elav	Rat	1:20	DSHB
Anti-Repo	Repo	Mouse	1:20	DSHB
Anti-GFP	GFP	Rabbit	1:1000	DSHB
Anti-FasII	Fasciclin II	Mouse	1:20	DSHB
Anti-B-gal	B-galactosidase	Rabbit	1:5000	DSHB
Anti-HA	HA	Rabbit	1:2000	SantaCruz
Anti-V5	V5	Mouse	1:2000	CST
Anti-β actin	β actin	Mouse	1:200	CST
Anti-IPP	IPP	Rabbit	1:200	MyBioSource
Secondary Antibodies				
Alexa Fluor 488-conjugated anti-Rat	Rat IgG H & L	Goat	1:800	Invitrogen
Alexa Fluor 488-conjugated anti-Rabbit	Rabbit IgG H & L	Goat	1:800	Invitrogen
Alexa Fluor 555-conjugated anti-Rat	Rat IgG H & L	Goat	1:800	Invitrogen
Alexa Fluor 647-conjugated anti-Mouse	Mouse IgG H & L	Goat	1:800	Invitrogen
Alexa Fluor 647 conjugated anti-Rat	Rat IgG H & L	Goat	1:800	Invitrogen
Cy5 conjugated anti-Mouse	Mouse IgG H & L	Goat	1:800	Invitrogen

3.2.7. Gels & Mediums

Gels and mediums used in this study and their ingredients are listed in Table 3.9.

Table 3.9. List and ingredients of gels and mediums.

Gel / Medium	Ingredients
1% Agarose Gel (20 ml)	0.2 g Agarose 20 ml dH_2O
LB Agar	3.5 g LB Agar 100 ml dH_2O
LB Broth	2.06 g LB Broth 100 ml dH_2O
7.5% Resolving SDS PAGE Gel (5 ml)	3.56 ml H_2O 2.5 ml AA:BAA:39:5:3 3.76 ml 1M Tris-HCl pH=8.8 0.2 ml 10% SDS 0.1 ml 10% APS 0.01 ml TEMED
4% Stacking SDS PAGE Gel (5 ml)	3.66 ml H_2O 0.66 ml AA:BAA:39:5:3 0.63 ml 1M Tris-HCl pH=8.8 0.1 ml 10% SDS 0.05 ml 10% APS 0.005 ml TEMED
SOC Medium pH= 7.0 (100 ml)	95 ml H_2O 2.0 g tryptone 0.5 g yeast extract 1ml of 1 M KCl
70% glycerol	70 % Neocortex glycerol 30 % PBS

3.3. Equipment

Lists of disposable and fixture laboratory equipment and their manufacturers are given in Table 3.10 and in Table 3.11 respectively.

Table 3.10. List of disposable equipment.

Disposable Equipment	
Material	**Manufacturer**
Micropipette Tips (10-200-1000-5000 µl)	VWR, USA
PCR tubes (200 µl)	Bio-Rad, USA
Plastic Pasteur pipette	TPP Techno Plastic Products AG, Switzerland
Falcon Tubes (15 - 50) ml	Becton, Dickinson and Company, USA
Culture tubes (14 ml)	Greiner Bio-One, Belgium
Petri Dishes, 60 x 15 mm	FIRATMED, Turkey
PVDF membrane	Roche Life Science, USA
Syringe (1cc)	Becton, Dickinson and Company, USA
Microscope cover glass	VWR, USA
Microscope slides	Fisher Scientific, UK
Microcentrifuge tubes	Citotest Labware Manufacturing, China

Table 3.11. List of fixture equipment.

Fixture Equipment	
Material	**Manufacturer**
Autoclave	Astell Scientific Ltd., UK
Centrifuges	Eppendorf, Germany (Centrifuge 5424, 5417R)
Confocal Microscope	Leica Microsystems, USA (TCS SP5)
Electrophoresis Equipment	Bio-Rad Labs, USA
Freezers	Arçelik, Turkey
Gel Documentation System	Bio-Rad Labs, USA (Gel Doc XR)
Incubator	Weiss Gallenkamp, USA (Incubator Plus Series)
Laboratory Bottles	Isolab, Germany
Micropipettes	Eppendorf, Germany
Microwave oven	Vestel, Turkey
Refrigerators	Arçelik, Turkey
Stereo Microscope	Olympus, USA (SZ61)
SynGene Visualizer	Syngene, USA
Thermal Cycler	Bio-Rad Labs, USA (C1000 Thermal Cycler)
Cold Room	Birikim Elektrik Soğutma

4. METHODS

4.1. Amplification of IPP from cDNA

Forward and reverse primers IPP-F: 5' CACCATGGCTAATGAGGACTGT CCCAAGG 3' and IPP-R: 5' AAGATTAAAAATCCCCTTTGTTAGA GTCTTGTGAT 3' were designed to amplify the *IPP* gene from human cDNA. Materials and the PCR Protocol are given in Tables 4.1 and 4.2 respectively.

Table 4.1. Components of the PCR reaction to amplify IPP from cDNA.

Reagents	**Final Concentration**
5x Q5 Reaction Buffer	1x
IPP-F 10 µM Forward Primer	0.5 µM
IPP-R 10 µM Reverse Primer	0.5 µM
dNTP 10 mM	200 µM
Q5 polymerase	0.02 units/µl
DNA	10 ng/µl
dH_2O	up to final volume

Table 4.2. PCR protocol to amplify IPP from cDNA.

PCR Steps	**Temperature**	**Duration**	**Number of Cycles**
Initial denaturation	98 °C	40 sec	1 X
Denaturation	98 °C	10 sec	40 X
Annealing	68 °C	1 min 10 sec	
Elongation	72 °C	3 min 30 sec	
Final Elongation	72 °C	5 min	1 X
Final Hold	12 °C	infinite	1 X

4.2. Agarose Gel Electrophoresis

20 ml of 1% agarose gel mixture was prepared by mixing 0.2 g agarose powder and 1X TAE Buffer. The mixture was heated in microwave to dissolve the agarose in the buffer. After allowing it to cool for 3-4 minutes, 4 µl of EtBr was added to the mixture. The mixture was then poured into the gel tray and left until it completely solidified. The time required for solidification naturally depends on the room temperature. Once solidified, the gel was placed in the electrophoresis tank. To define the size of bands of interest, 2 µL of the appropriate ladder was loaded to the first well.

4.3. Purification of DNA from Agarose Gel

100 µl of PCR product and 20 µl Loading dye were loaded onto the gel. Then band of interest was then dissected on the transilluminator and transferred to an Eppendorf tube. The gel was weighed, and QIAEX I Buffer in a volume three times that of the gel's weight was added. The mixture was vortexed for a minute, followed by incubation at 55°C for 10 minutes with occasional shaking. Afterward, it was centrifuged for 30 seconds at 12,000 rpm, and the supernatant was discarded. Next, 300 µL of QX1 was added to the pellet, resuspended by vortexing, and centrifuged again for 30 seconds at 12,000 rpm. The supernatant was once again discarded, and another 300 µL of QX1 was added to the pellet. After resuspension by vortexing, it was centrifuged for 30 seconds at 12,000 rpm to ensure complete removal of residual agarose. To the pellet, 300 µL of PE Buffer was added and vortexed for 30 seconds to dissolve the salt. The mixture was then centrifuged for 30 seconds at 12,000 rpm, and the supernatant was discarded. This step was repeated three times. Subsequently, the tube was kept open with its cap at 37°C to remove all remaining supernatant until the pellet turned completely white. The pellet was dissolved in 25 µL of dH2O by incubating at 55°C with occasional vortexing. A final centrifugation was performed at 12,000 rpm for 2 minutes to eliminate any remaining beads that could affect the efficiency of subsequent experiments. The supernatant was transferred to a fresh Eppendorf tube, and the concentration of the purified DNA was measured using a NanoDrop Spectrophotometer.

4.4. Gateway BP Cloning

The Polymerase Chain Reaction (PCR) was carried out using primers designed in accordance with the Gateway Manual Protocol to introduce attB sites to the isolated IPP sequence. The IPP sequence with flanking attB sites was subsequently cloned into the pDONR207 Donor Vector. For this, a reaction was set up by combining 2 µL of BP Clonase, 1 µL of 150 ng/µL donor vector, and 6 µL of TE Buffer in a PCR tube. The reaction was allowed to proceed overnight at room temperature. Following the overnight incubation, the reaction was treated with 2 µL of Proteinase K and maintained at 37°C for 20 minutes.

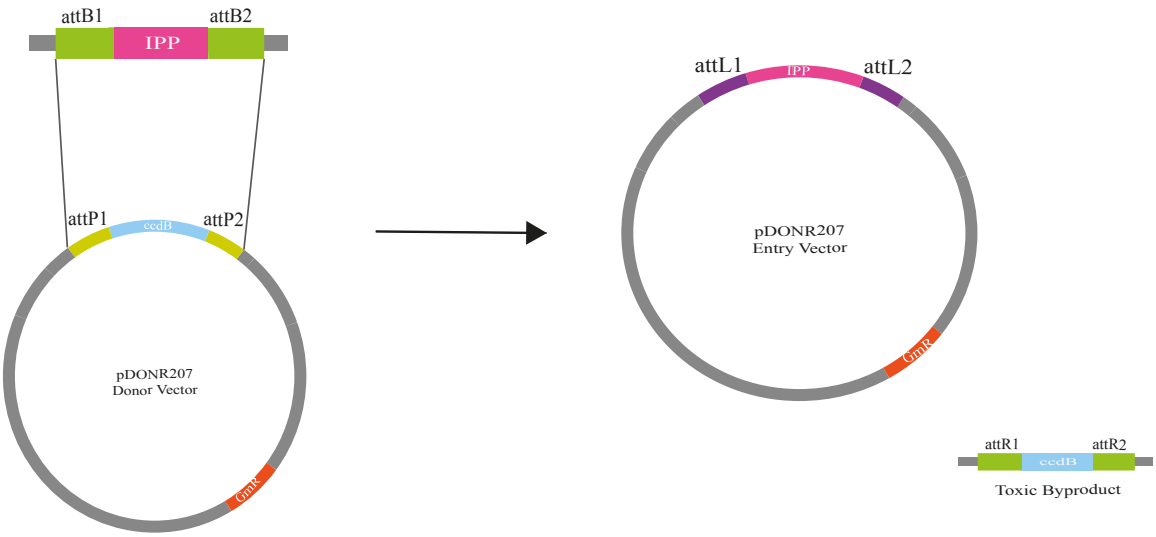

Figure 4.1. Schematic representation of Gateway BP Cloning of IPP into pDONR207 vector. attB sites were introduced to IPP with PCR. IPP was cloned into pDONR207 vector, which features two attP sites. The ccdB region between the two attP sites is expected to be removed, forming a toxic byproduct if the cloning is successful.

4.5. Site Directed Mutagenesis

In order to mimic the mutation observed in one of the affected families, site-directed mutagenesis (SDM) was conducted using PCR. Forward and reverse primers, IPPsdmF 5' CTTTGGGTAGATGGGTTGGAGCTG 3' and IPPsdmR 5' CAACCCATCTACCCAAAG CATAGATAGCC 3', were designed to change 1189th G to A position, resulting in a G397R alteration. The materials and the PCR Protocol are given in Tables 4.3 and 4.4 respectively.

Table 4.3. Reagents for PCR Reaction for SDM.

Reagents	**Final Concentration**
5x Q5 Reaction Buffer	1x
IPPsdm 10 μM Forward Primer	0.5 μM
IPPsdm 10 μM Reverse Primer	0.5 μM
dNTP 10 mM	200 μM
Q5 polymerase	0.02 units/μl
DNA	10 ng/μl
dH_2O	up to final volume

Table 4.4. PCR protocol for SDM.

PCR Steps	**Temperature**	**Duration**	**Number of Cycles**
Initial denaturation	98°C	30 sec	1 X
Denaturation	98°C	10 sec	35 X
Annealing	69.7°C	1 min 10 sec	
Elongation	72°C	3 min 30 sec	
Final Elongation	72°C	5 min	1 X
Final Hold	12°C	infinite	1 X

4.6. *Dpn*I Digestion

*Dpn*I restriction enzymes recognizes the methylated sites on DNA and used to get rid of the template DNA in reaction. 20 µl mix was prepared with 16 µl dH_2O, 4 µl 10x CutSmart Buffer and 0.3 µl *Dpn*I. 8 µl of the mix was added to PCR reactions. Kept overnight in 37°C room.

4.7. Gateway LR Cloning

Gateway LR Cloning was conducted into different destination vectors pUASg::HA and pLEX307 to address different aims. Generated pDonr207_IPP^{WT} and pDonr207_IPP^{G397R} entry vectors were cloned into pUASg::HA vector that were then injected to fly embryos to generate transgenic fly lines which will express human IPP gene under control of a GAL4 driver (Figure 4.2). 1 µl of entry vector with 150 ng/µl concentration and 1 µl of destination vector with 150 ng/µl concentration was mixed with 2 µl LR Clonase in 6 µl TE Buffer and kept in room temperature for overnight. Then the reaction was treated with 2 µl Proteinase K and kept in 37°C for 20 minutes. pDonr207_IPP^{WT} and pDonr207_IPP^{G397R} entry vectors were also cloned into pLEX307 vector with the same procedure to obtain destination vectors that are compatible for transduction (Figure 4.3).

4.8. Transformation

After each cloning step reactions were transformed into competent *E.coli* cells by heat shock method. Three different strains were used DH5α, Stbl3 and Db3.1. pLEX307 vectors are lentiviral vectors, they are more resilient to mutations to prevent that Stbl3 strain was used. Db3.1 strain is a ccdB resistant strain, transformation with this strain was done to amplify pLEX307 vectors. DH5α is the regular *E.coli* strain that was used in transformations of pDONR207 and pUASg::HA plasmids.

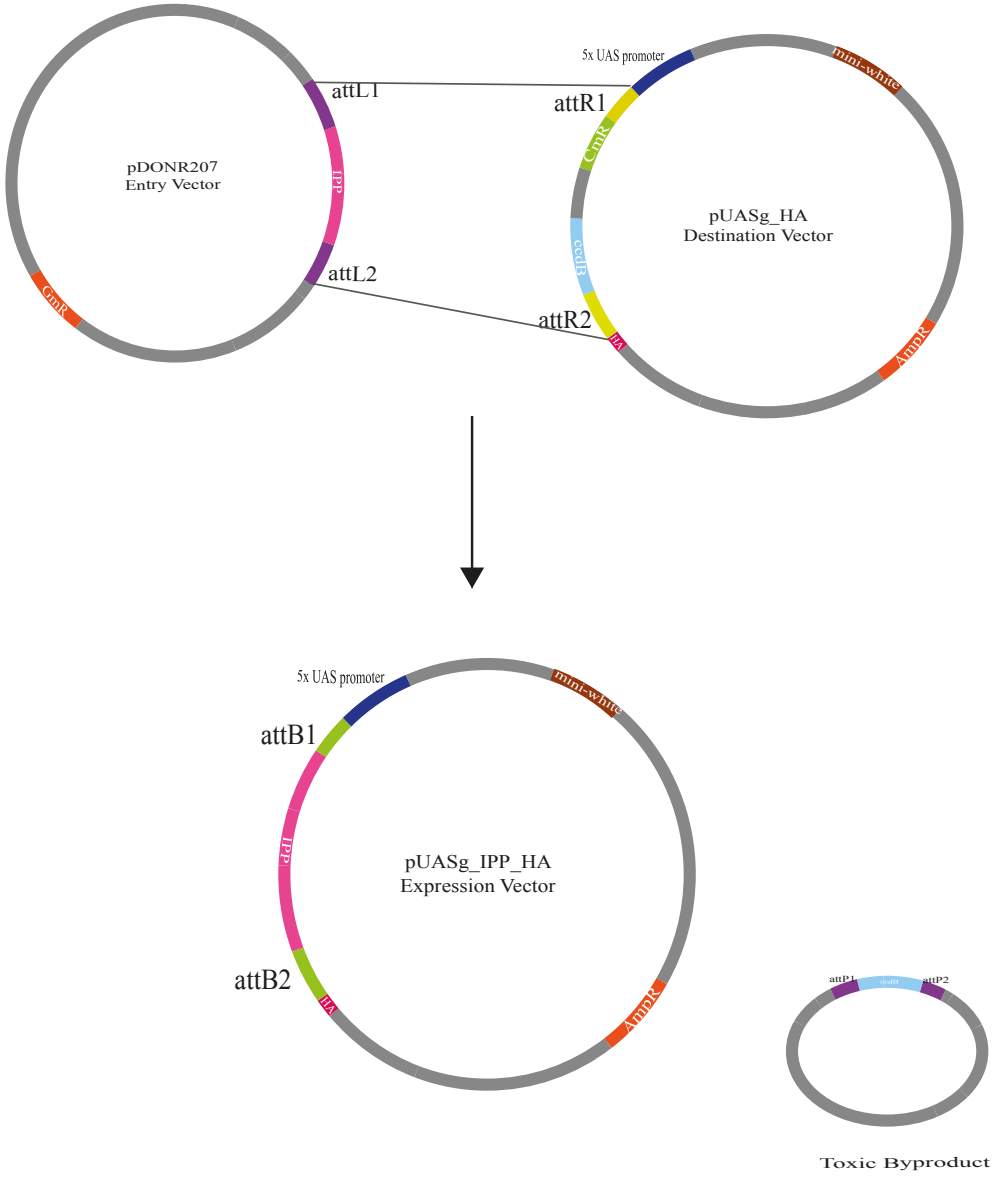

Figure 4.2. Schematic representation of IPP into pUASg::HA destination vector. IPP^{WT} and IPP^{G397R} was cloned into pUASg::HA vector via Gateway LR Cloning method. IPP^{WT} was cloned into pDONR207 vector which has two attP sites. IPP^{G397R} was produced by site directed mutagenesis method with PCR. ccdB region between two attL sites expected to be integrated into pDONR207 vector and form a toxic byproduct if the clonings succeed.

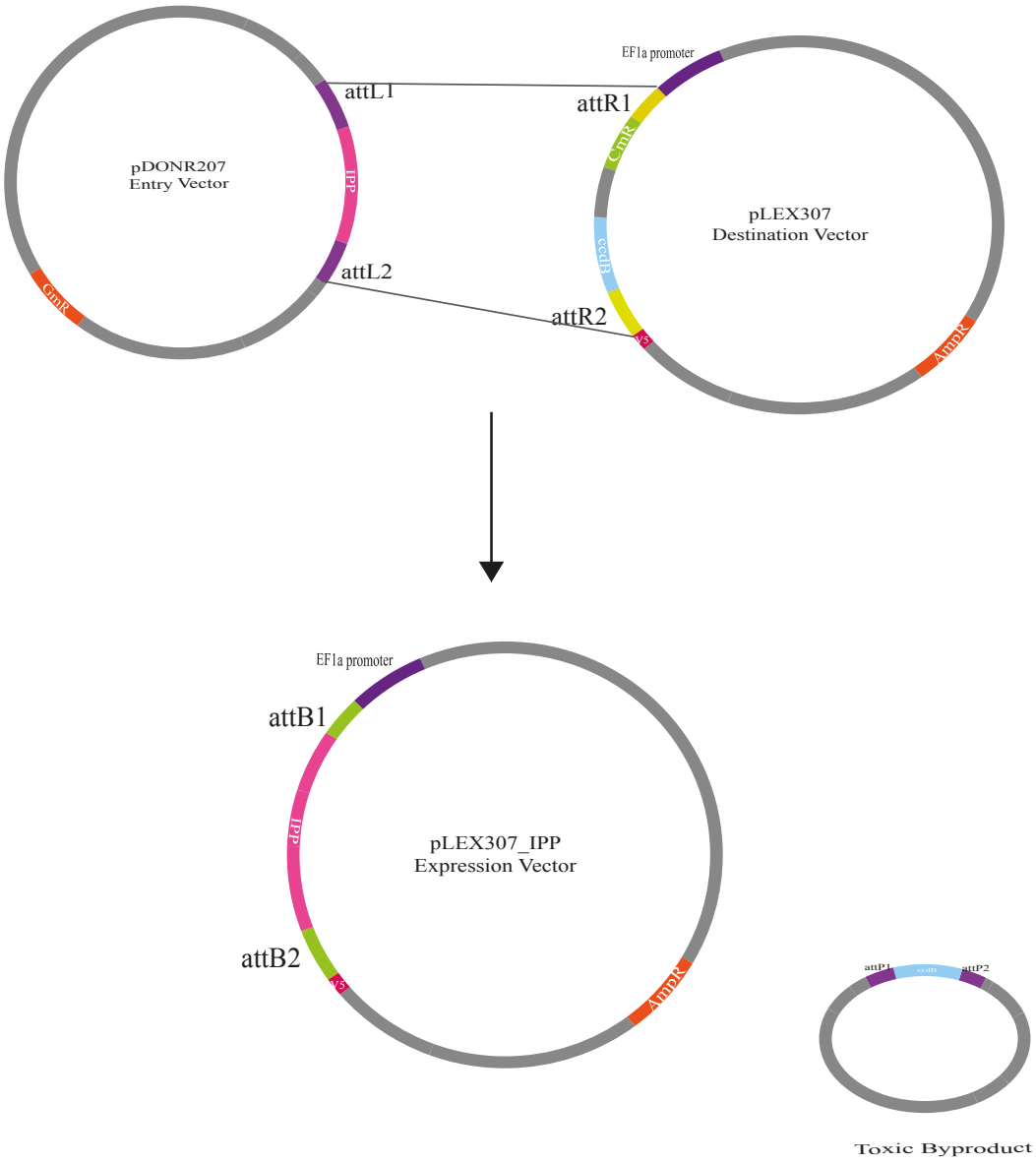

Figure 4.3. Schematic representation of Gateway LR Cloning into pLEX vector. IPP^{WT} and IPP^{G397R} was cloned into pLEX307 vector via Gateway LR Cloning method. IPP^{WT} was cloned into pDONR207 vector which has two attP sites. IPP^{G397R} was produced by site directed mutagenesis method with PCR. ccdB region between two attL sites expected to be integrated into pDONR207 vector and form a toxic byproduct if the clonings succeed.

2 µl of reactions was added into 50 µl competent cell aliquots and incubated in wet ice for 20 minutes. After incubation, heat shock was applied to cells for 42 seconds at 42°C. Cells were then directly put back into ice and kept in for 5 minutes. Then 250 µl SOC medium was added and tubes were kept in 37°C for 1.5 hours. After 1.5 hours, tubes were centrifuged 5 minutes at 12.000 rpm, supernatant was discarded. The pellet was resuspended by vortexing and spread on LB-Agar plates prepared with antibiotics that vectors are resistant to. (Gentamycin for pDonr207, Ampicillin for pUASg::HA and pLEX307 vectors). Plates were kept in 37°C overnight. Transparent colonies were picked and were grown in 5 ml Broth LB with antibiotics that vectors are resistant to at 30°C for 24 hours for vectors transformed into Stbl3 and Db3.1 and at 37°C for 16 hours for the vectors transformed into DH5α cells.

4.9. Plasmid Isolation

Zymo Zyppy Mini Prep Kit was used for plasmid isolation. Culture tubes were kept in ice for 30 minutes in ice to enhance the precipitation, tubes were then centrifuged at 4000 rpm 4°C for 15 minutes. Supernatants were discarded, pellets were resuspended by vortexing. Around 100-150 µl of pellet suspensions was obtained from overnight incubations. Suspensions were transferred to 1.5 ml tubes. 40 µl Lysis Buffer was added to each tube, tubes were inverted 6-8 times, then before exceeding 2 minutes, 140 µl Neutralization Buffer was added, tubes were inverted until homogenous yellow color obtained. Tubes were centrifuged at 10.000 rpm 24°C for 3 minutes, then centrifuged once more after placing them in reverse orientation at 12.000 rpm 24°C for 3 minutes. Supernatants were carefully pipetted without disturbing the pellet and transferred to the supplied columns. Columns were centrifuged at 10.000 rpm for 3 minutes, the flow-through was discarded. 80 µl Endo-Wash Buffer was applied to each column. Columns were centrifuged at 10.000 rpm for 3 minutes the flow-through was discarded. 160 µl Zyppy-Wash Buffer was applied to each column. Columns were centrifuged at 10.000 rpm for 3 minutes the flow-through was discarded. Columns were centrifuged at 10.000 rpm for a minute to get rid of residual wash buffer. For eluting the DNA, 20 µl dH_2O was applied to each column. Columns were incubated at 60°C for 10 minutes, then centrifuged at 10.000 rpm for 3 minutes. Another 20 µl dH_2O was applied to each column. Columns were once

again incubated at 60°C for 10 minutes, then centrifuged at 10.000 rpm for 3 minutes. Concentrations of isolated plasmids were measured with NanoDrop Spectrophotometer.

4.10. Restriction Digestion

To verify each isolation and cloning step, vectors were digested with *Pst*I restriction enzyme. For 10 µl reaction, 100 ng/µl vector of interest, 1 µl NEB 3.1 buffer for the specific enzyme, 0.1 µl enzyme and up to 10 µl dH_2O were mixed. Reaction tubes were kept in 37°C overnight. After incubation 3 µl of each reaction was mixed with 1 µl 6X Loading Dye and were loaded on the gel.

4.11. Transduction & Immunocytochemistry

Transduction of pLEX307_IPP^{WT} and pLEX307_IPP^{G397R} vectors into HeLa cells was conducted by Elif Darbuka Tula. Transduced cells residing on the 12 well plates were washed with PBS then fixed with 300 µl 4%PFA at 37°C for 10 minutes. Cells were then washed with PBS 3 times for 5 minutes each to get rid of the fixative solution. Cells were kept in PBST for 30 minutes to enable membrane permeabilization. Then blocked with 5% BSA in PBS for 1 hour. Primary antibody incubation was done overnight at 4°C. After incubation, primary antibody was washed from the cells 3 times with PBST wash buffer. Cells were then incubated with secondary antibody 1:1000 for 2 hours at room temperature. Residual secondary antibody was by 3 times 5-minute PBST washes. For nuclear staining DAPI was used in 1:1000 concentration. Incubation was done for 10 minutes. Cells were washed once again with PBST and were finally mounted with mounting medium.

4.12. Plasmid Injection into Fly Embryos

PhiC31 Embryo injection and transformant selection were performed at GenetiVision (USA, Inc.). pUAS_IPP^{WT} and pUAS_IPP^{G397R} constructs were injected into 200 embryos of the *Drosophila melanogaster* strain *yw*; attB (VK37 line).

4.13. Protein Extraction from Adult Flies

15 female and 20 male flies were isolated for each strain and frozen in -80°C freezer prior to extraction. Flies were homogenized by adding 150 µl RIPA Buffer with 1mM PMSF and 1x Proteinase Inhibitor on ice and kept on ice for 40 minutes. Lysates were then centrifuged at 13000 rpm for 20 minutes at 4°C. Mid clear phase between the pellet and upper lipid phase was transferred to another tube. Lysates were diluted 10x and 20x in 25 µl volume (4 µl from the lysate 36 µl dH2O for 10x; 12.5 µl 10x + 12.5 µl dH2O for 20x; 2.5 µl of 10x dilutions were discarded to adjust the volume) 60 µl of each remaining lysate was mixed with 30 µl 3x Laemmli Buffer (7.5% beta-mercaptoethanol) boiled at 99°C for 5 minutes on ThermoMixer.

BioRad Protein Assay was used to measure the protein concentration in each lysate. Reagent A' was prepared with 50x Reagent S and preheated Reagent A. First 125 µl of Reagent A' then 1 ml of Reagent B were added to 25 µl of diluted lysate. Blank sample was prepared with 25 µl dH_2O plus 125 µl Reagent A' plus 1 ml Reagent B. BSA was used as a standart for the calibration curve. Reactions were vortexed and kept in dark for 10 minutes. Following that incubation OD at 750 nm was measured using Spectrophotometer. Calibration curve was built measuring OD of the reactions 0.2, 0.4, 0.8, 1.2, 1.6 and 2 mg/ml BSA. Concentrations of lysates were calculated according to the OD values and were adjusted prior to loading on the gel in order to load 100 µg of the total protein to the well.

4.14. SDS-Polyacrylamide Gel Electrophoresis

7.5 % resolving gel and 4 % stacking gel were prepared according to the recipe given in the 3.2.6. First, the resolving gel was poured into the space created between the glass plates and dH_2O was added on top of it to protect the resolving gel from air contact and to smoothen the top edge of the gel before it polymerizes. Once the resolving gel is set, dH_2O was discarded from the top. Onto the set resolving gel, the stacking gel was poured carefully, and an appropriate comb was quickly inserted in the stacking gel between the glass plate before it polymerizes. 2 µl of Ladder, 8 µl of samples were loaded in the wells. For

electrophoresis, the polyacrylamide gel is clamped and inserted in the buffer tank. The tank was filled with 1X Running Buffer, which was prepared by diluting 10X Running Buffer with distilled water. The samples were loaded in separate wells along with the prestained protein ladder at the first well to be able to assess the size of the proteins after the electrophoresis. Electrophoresis was performed using constant voltage U = 80 V until the front reached to the resolving gel, then 120 V until the front reached end of the resolving gel.

4.15. Western Blot

Resolving gel was briefly rinsed with dH_2O and transferred into the BioRad cassette with a PVDF membrane which was preactivated with methanol, in between sponges and Whatman papers. The cassette was placed into the tank filled with 1x Transfer Buffer. Transfer was performed at 4°C with constant current set in range I = 200-220 mA current to reach corresponding voltage U = 90–100 V. After transfer, the membrane was briefly washed with dH_2O, then stained with Ponceau S for 15 minutes. After Ponceau S staining, membrane is initially washed with dH_2O to visualize the bands, then with 0.1% SDS to wash out Ponceau S dye. Membrane was then washed with TBS-t for 5 minutes 6 times. Blocked with %5 Milk for an hour, then incubated in primary antibody solution in milk overnight at 4°C. After overnight incubation, membrane was washed from the primary antibody with TBS-t for 5 minutes 6 times and with TBS for 5 minutes 2 times. Right before the visualization process membrane was transferred to dH_2O. To prepare ECL mix, the equal volumes of Westernbright Sirius and Westernbright Peroxide solutions were mixed. Half of the mixture poured on the transparent plastic sheet membrane was placed on the ECL mix then the membrane was covered with the rest of the solution, another plastic sheet was was placed into the SynGene Visualizer. Visualization of the membrane was performed as a series of images with incrementing exposure time and visual marker.

4.16. Fly Husbandry and Crosses

Flies were maintained at 25°C and constant 40% humidity in the culture vials with 5-10 ml fly food. Fly food was prepared with dH_2O, agar, corn flour, yeast, and molasses. Tegosept and propionic acid were added to prevent bacterial and fungi contamination.

In most of the experiments that used flies as model, UAS-Gal4 bivalent system was used. UAS is an upstream enhancer. Gal4 driver line and UAS reporter line of interest were anesthetized with CO_2, 5 virgin females from one line and 5 males from the other line were placed in plastic vials with fly food and kept in 25°C. After 7-8 days as the pupae form on the walls of the vial, adults are discarded or flipped into another vial in order to prevent mixing the parent with the progeny. After 11 days, the progeny is expected to start emerging, by following markers of the balancers and insertions, flies the genotype of interest can be collected and analyzed.

4.17. Immunohistochemistry

For brain staining, 5-7 days old flies were selected carefully and kept on ice to keep them inactive. The dissection step should be maximum 40 minutes for adult brains and 20 minutes for larval brains to prevent tissue deterioration. Tissues were dissected in cold 1X PBS and were kept in a black cuvette filled with PBS on ice. As dissection time ends, dissected tissues were transferred to a 500 ml Eppendorf tube with pre-PBST washed tips (to prevent tissues stick on the tips) and fixed in cold 4% PFA for 25 minutes at room temperature, constantly shaking on the nutating mixer. After fixation, PFA was removed and the tissues were washed first one time for a minute to get rid of excessive amount of fixative solution, then for 3 times for 20 minutes with 0.03% PBS-T (~300 µL) on the nutating mixer. After washes, tissues were then blocked with PAXD for 30 minutes at room temperature incubation to prevent unspecific binding of antibodies. Primary antibody solutions were prepared according to the recommended dilutions by manufacturer in PAXD. Primary antibody incubation was done overnight at 4°C. upon incubation, primary antibody solution was removed, and the tissues were washed three times for 20 minutes with 0.03% PBS-T. Secondary antibody solutions were prepared according to the recommended dilutions by manufacturer (1:800) and added to the tubes after the washing steps. The tissues were put into black boxes to prevent light exposure as much as possible and incubated in the secondary antibody solution overnight at 4°C. After the secondary antibody incubation, the tissues were washed with 0.3% PBST three times for 20 minutes and two washes for 20 minutes with 1X PBS was done at room temperature. Tissues were then placed on microscope slides and excess amount of PBS was removed by micropipette. Tissues were mounted on a microscope slide with 70 % glycerol and covered with coverslip. Each corner

and side of the coverslip was coated with nail polish to protect tissues from drying. Slides were kept in 10°C fridge in opaque boxes up until visualization under confocal microscopy.

5. RESULTS

5.1. Verification of CRIMIC Construct Induced Knockout of *CG9426*

Loss of function assays were conducted to understand the function of CG9426. *CG9426* knockout mutants was generated by Bellen Lab using the CRIMIC method (details provided in Section 1.11). The CRIMIC lines contain a cassette with several functional sequences that are inserted into the intronic region of the gene of interest. This insertion resulted in the disruption of transcription due to the presence of polyA sequence. The viability rate of the homozygous $CG9426^{CRIMIC}$ flies was approximately 2.7%, and the viable adults had a maximum lifespan of only 5 days. To verify that the CRIMIC cassette is indeed integrated into the *CG9426* gene and that the low viability rate of homozygous mutants is caused by this integration, a complementation analysis was performed using BAC^{99C18}, *Df(2L)* and *Dp(2;3)* lines.

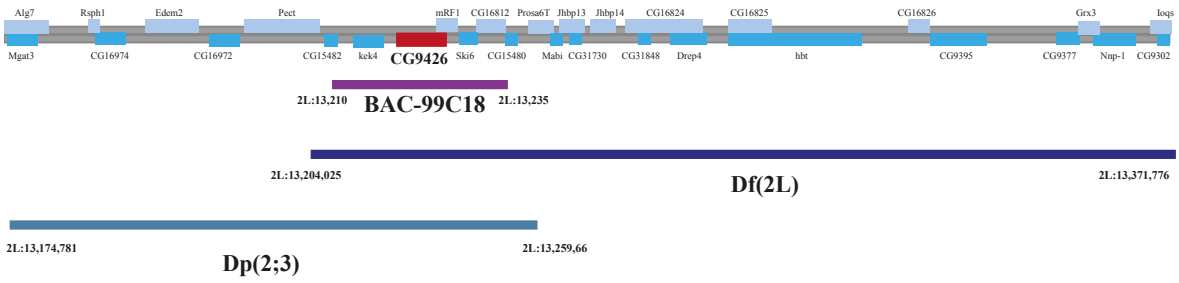

Figure 5.1. Genomic region of complementation constructs. The BAC^{99C18} construct has an additional copy of the genomic region between 2L:13,210 and 2L:13,235 including *CG9426*. The *Df(2L)* deficiency line has a massive deletion between coordinates 2L:13,204,025 and 2L:13,371,776, which encompasses 34 genes. The *Dp(2,3)* line carries an insertion from the 2nd chromosome within coordinates 2L:13,174,781 and 2L:13,259,661 on the 3rd chromosome.

A Bacterial Artificial Chromosome (BAC) is a large construct created through site-specific transgenesis mediated by the phiC31 integrase (Venken, 2009). The *BAC^{99C18}* construct encompasses a substantial genomic region, including *CG9426*, and was integrated into the 3rd chromosome of flies by the GenetiVision company. The rescue ratio for the low viability rate of homozygous *CG9426^{CRIMIC}* mutants by *BAC^{99C18}* was analyzed using the cross scheme represented in Figure 5.2.

Initially, a balanced heterozygous *CG9426^{CRIMIC}* line was crossed with a balanced *BAC^{99C18}* line, resulting in a lineage that carried the *C9426^{CRIMIC}* allele on the second chromosome and the BAC^{99C18} insertion on the third chromosome in the F1 generation. Subsequently, this F1 generation was crossed with the balanced *CG9426^{CRIMIC}* line. The ensuing F2 generation was categorized into three groups: F2.1 with heterozygous *C9426^{CRIMIC}* carrying *BAC^{99C18}* on the 3rd chromosome; F2.2 with homozygous *C9426^{CRIMIC}* carrying *BAC^{99C18}* on the 3rd chromosome; and F2.3 with heterozygous or homozygous *C9426^{CRIMIC}* without *BAC^{99C18}* on the 3rd chromosome. Notably, homozygous *CyO/CyO* lines should be lethal, so they are not depicted on the scheme and are not taken into consideration in calculations.

The effect of *BAC^{99C18}* on the viability rate of homozygous *CG9426^{CRIMIC}* mutants was determined by calculating the ratio of F2.1 to the sum of F2.1 and F2.2. GFP fluorescence in the eyes was utilized as a marker for the *CG9426^{CRIMIC}* allele, while w+ phenotype was used as the marker of the presence of *BAC^{99C18}* construct. The selection against the *CyO* balancer, which bears a curly wing marker, was applied to isolate homozygous *CG9426^{CRIMIC}* mutants. Among the 92 flies observed, 16 exhibited straight wings and red eyes, indicating that they were homozygous *CG9426^{CRIMIC}* mutants carrying *BAC^{99C18}*. As illustrated in the purple-colored column of Figure 5.6, the presence of one copy of the *BAC^{99C18}* construct increased the viability rate of homozygous *CG9426^{CRIMIC}* mutants from 2.7% to 17.4%.

To statistically evaluate the significance of the difference in the ratios of these genotypes within the populations, a Fisher’s exact t-test was conducted, resulting in a p-value of less than 0.0001. Fisher's exact provides an exact p-value calculation.

Although 17.4% might not appear as a high viability rate, it is important to emphasize that this analysis was limited to balanced lines to ensure homozygosity tracking. Moreover, considering Mendelian genetics, the expected maximum ratio of homozygous *CG9426*^{CRIMIC} flies is 33% due to the lethal nature of *CyO/CyO* lines. On the graph in Figure 5.6, the ratios were aligned according to this theoretical expectation.

The *Df(2L)* deficiency line has a massive deletion between coordinates 2L:13,204,025 and 2L:13,371,776, which encompasses 34 genes including *CG9426*. The *Dp(2,3)* line carries an insertion from the 2nd chromosome within coordinates 2L:13,174,781 and 2L:13,259,661 on the 3rd chromosome. This construct includes 25 duplicated genes, including *CG9426*. The *Df(2L)* line is homozygous lethal. Given that the duplicated region in *Dp(2;3)* significantly overlaps with and includes most of the genes deleted in the *Df(2L)* line, it was expected that the duplication could compensate for the lethality seen in the deficiency line.

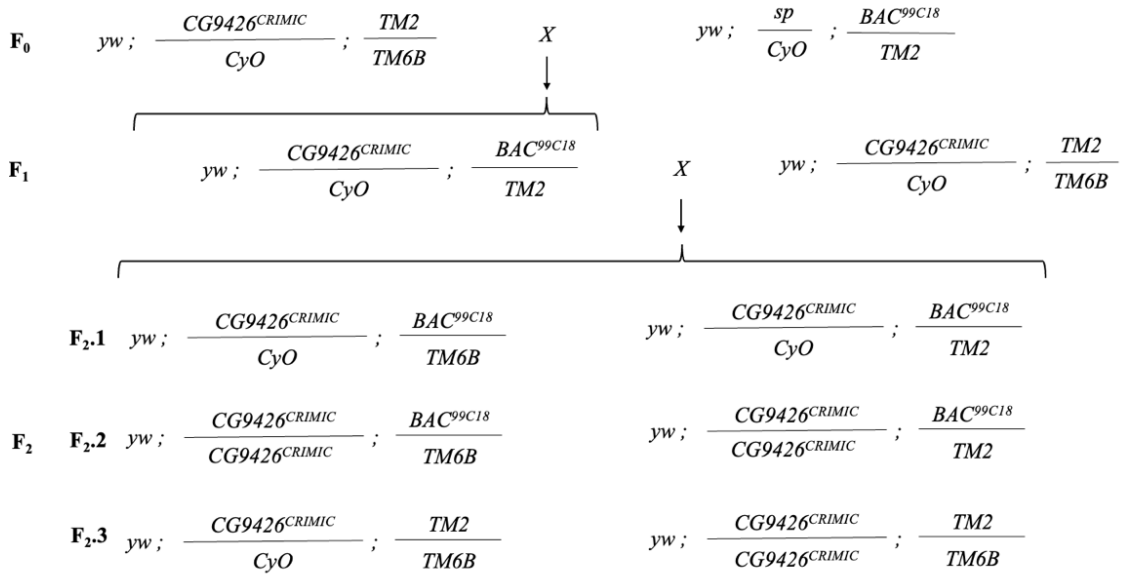

Figure 5.2. Cross scheme to analyze the rescue of homozygous *CG9426*^{CRIMIC} mutants by *BAC*^{99C18}. A balanced heterozygous *CG9426*^{CRIMIC} line was crossed with a balanced *BAC*^{99C18} line. The resulting progeny carrying both constructs were then crossed with a balanced heterozygous *CG9426*^{CRIMIC} line. The ratio of F2.2 over the sum of F2.1 and F2.2 was calculated to measure the viability rate of homozygous mutants in the progeny.

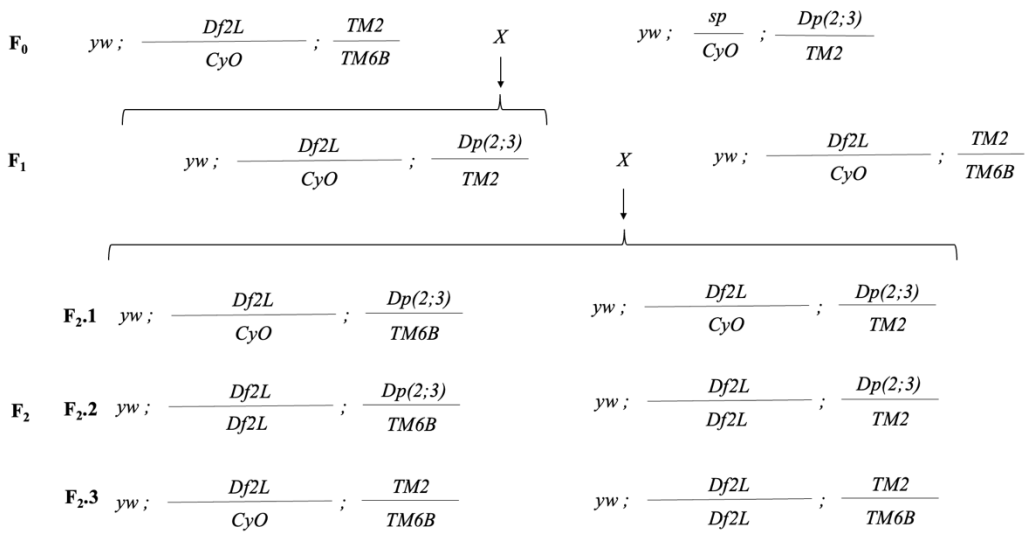

Figure 5.3. Cross scheme to analyze the rescue of low viability rate in the *Df(2L)* line by *Dp(2;3)*. A balanced heterozygous *Df(2L)* line was crossed with a balanced *Dp(2;3)* line. The progeny carrying both constructs were then crossed with a balanced heterozygous *Df(2L)* line. The ratio of F2.2 over the sum of F2.1 and F2.2 was calculated to determine the viability rate of homozygous mutants.

The ratio of *Df(2L)* homozygous mutants rescued by *Dp(2;3)* was analyzed using the cross scheme depicted in Figure 5.3. A balanced *Df(2L)* line was crossed with a balanced *Dp(2,3)* line, resulting in progeny carrying *Df(2L)* on the second chromosome and *Dp(2;3)* on the third chromosome in the F1 generation. Then, the F1 generation was crossed with a balanced *Df(2L)* line. The F2 generation can be divided into three groups: F2.1 heterozygous *Df(2L)* with *Dp(2;3)* on the 3rd chromosome; F2.2 homozygous *Df(2L)* with *Dp(2;3)* on the 3rd chromosome; and F2.3 heterozygous or homozygous *Df(2L)* without *Dp(2;3)* on the 3rd chromosome. As homozygous *CyO/CyO* lines should be lethal, they are neither shown on the scheme nor taken into consideration in calculations. The effect of *Dp(2;3)* on the viability rate of homozygous *Df(2L)* was calculated as the ratio of F2.1 to the sum of F2.1 and F2.2.

Based on the phenotypic markers, it was observed that 29 out of the 121 flies had straight wings and red eyes. As depicted on the indigo-colored column in Figure 5.6, the presence of the *Dp(2;3)* construct increased the viability rate of homozygous *Df(2L)* mutants from 0% to 24%.

The rescue ratio of the low viability rate in homozygous *CG9426*^{CRIMIC} mutants by *Dp(2;3)* was analyzed using the scheme depicted in Figure 5.4. A balanced *CG9426*^{CRIMIC} line was crossed with a balanced *Dp(2;3)* line to generate progeny with *CG9426*^{CRIMIC} on the second chromosome and *Dp(2;3)* on the third chromosome in the F1 generation. Subsequently, the F1 generation was crossed with a balanced *CG9426*^{CRIMIC} line. The F2 generation was categorized into three groups: F2.1 represented heterozygous *CG9426*^{CRIMIC} with *Dp(2;3)* on the third chromosome; F2.2 depicted homozygous *CG9426*^{CRIMIC} with *Dp(2;3)* on the third chromosome; and F2.3 included heterozygous or homozygous *CG9426*^{CRIMIC} without *Dp(2;3)* on the third chromosome. It's important to note that homozygous *CyO/CyO* lines, which should be lethal, were neither displayed on the scheme nor considered in calculations. As previously mentioned, the homozygous *CG9426*^{CRIMIC} line could not reach the adult stage, resulting in a viability rate of 2.7% for homozygous mutants. The impact of the gene *Dp(2;3)* on the viability rate of homozygous *CG9426*^{CRIMIC} was determined by calculating the ratio of F2.1 to the sum of F2.1 and F2.2. The ratio of homozygous *CG9426*^{CRIMIC} lines was determined by observing flies without curly wings, tracking the presence of *sp*, *CyO*, *TM2*, and *TM6B* balancers, and confirming eye color, which should be red in the presence of the *Dp(2;3)* construct. Additionally, flies were examined under a fluorescent microscope to detect the GFP signal associated with the CRIMIC construct insertion. Among the 107 flies analyzed, 16 exhibited straight wings and red eyes. These flies were also double-checked under the fluorescent microscope. As illustrated in the plum-colored column of Figure 5.6, the presence of the *Dp(2;3)* construct increased the viability rate of homozygous *CG9426*^{CRIMIC} mutants from 2.7% to 15%. A Fisher's t-test was conducted to determine whether there was a significant difference between the viability rates of *CG9426*^{CRIMIC} and *Df(2L)* lines. The calculated p-value was less than 0.098. Notably, *Dp(2;3)* was able to rescue the low viability rate in both of the lines.

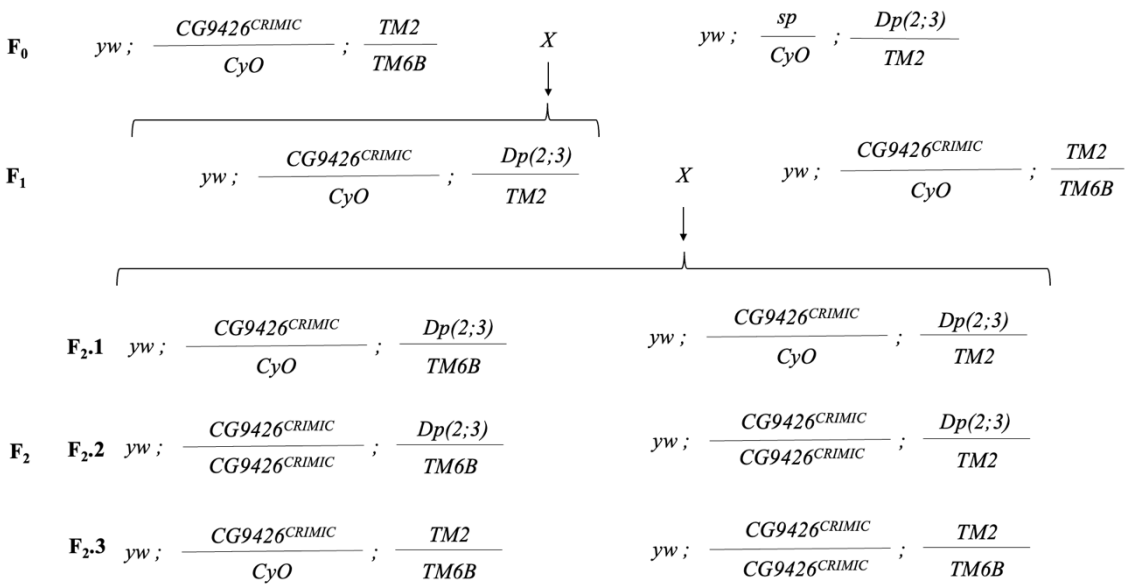

Figure 5.4. Cross scheme to analyze complementation of the *C9426*^{CRIMIC} allele by *Dp(2;3).* A balanced heterozygous *C9426*^{CRIMIC} line was crossed with a balanced *Dp(2;3)* line. The progeny that carried both constructs was then crossed with a balanced heterozygous *C9426*^{CRIMIC} line. The ratio of F2.2 over F2.1 and F2.2 was calculated to determine the viability rate of homozygous mutants.

Complementation analysis with *CG9426*^{CRIMIC} and *Df(2L)* lines was conducted following the scheme depicted in Figure 5.5. Initially, a balanced *CG9426*^{CRIMIC} line was crossed with a balanced *Df(2L)* line. In the F1 generation, *Df(2L)/CyO* flies were identified by their red eyes, while *CG9426*^{CRIMIC}*/CyO* flies were selected based on the absence of red eye color and the presence of GFP signal in their eyes. Flies carrying both *CG9426*^{CRIMIC} and *Df(2L)* were expected to exhibit straight wings. Out of the 130 flies analyzed, the viability rate of homozygous mutants was determined to be 2.7%. The viability rate of *CG9426*^{CRIMIC}*/Df(2L)* flies was calculated by considering the ratio of F1.1 over the sum of F1.1, F1.2, and F1.3.

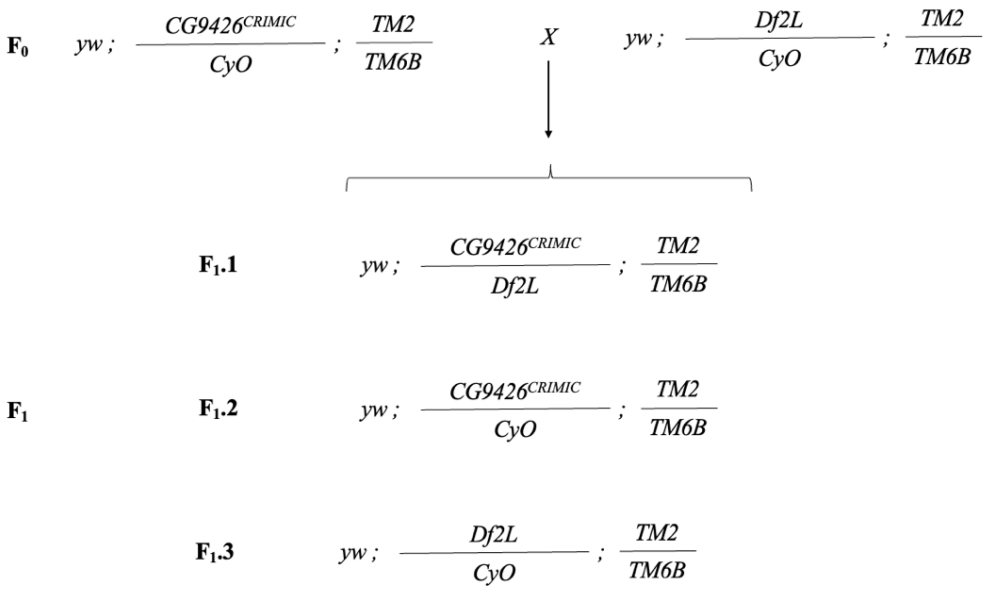

Figure 5.5. Cross scheme to analyze complementation of *CG9426*^{CRIMIC} mutants by the *Df(2L)* allele. A balanced heterozygous *C9426*^{CRIMIC} line was crossed with a balanced *Df(2L)* line. The ratio of viable lines carrying both constructs was determined by calculating the ratio of $F_{1.}2$ over the total number of progeny.

Upon observation, none of the 130 flies exhibited straight wings, indicating that *Df(2L)* did not complement the *CG9426*^{CRIMIC} mutation. This suggests that the *CG9426*^{CRIMIC} mutation is likely located within a genomic region different from 2L:13,204,025 to 2L:13,371,776 on the second chromosome. To statistically assess the difference in viability rates between homozygous *CG9426*^{CRIMIC} and *CG9426*^{CRIMIC}*/Df(2L)* lines, a Fisher's t-test was performed. The analysis indicated no significant difference in viability rates between these two lines, with a calculated p value of 0.06.

Significant increase in the viability rate of homozygous *CG9426*^{CRIMIC} lines in the presence of *BAC*^{99C18} and *Dp(2;3)* constructs was accepted as a convincing result to conclude that the low viability rate observed in the *CG9426*^{CRIMIC} line is due to transcriptional arrest of *CG9426* but no other gene.

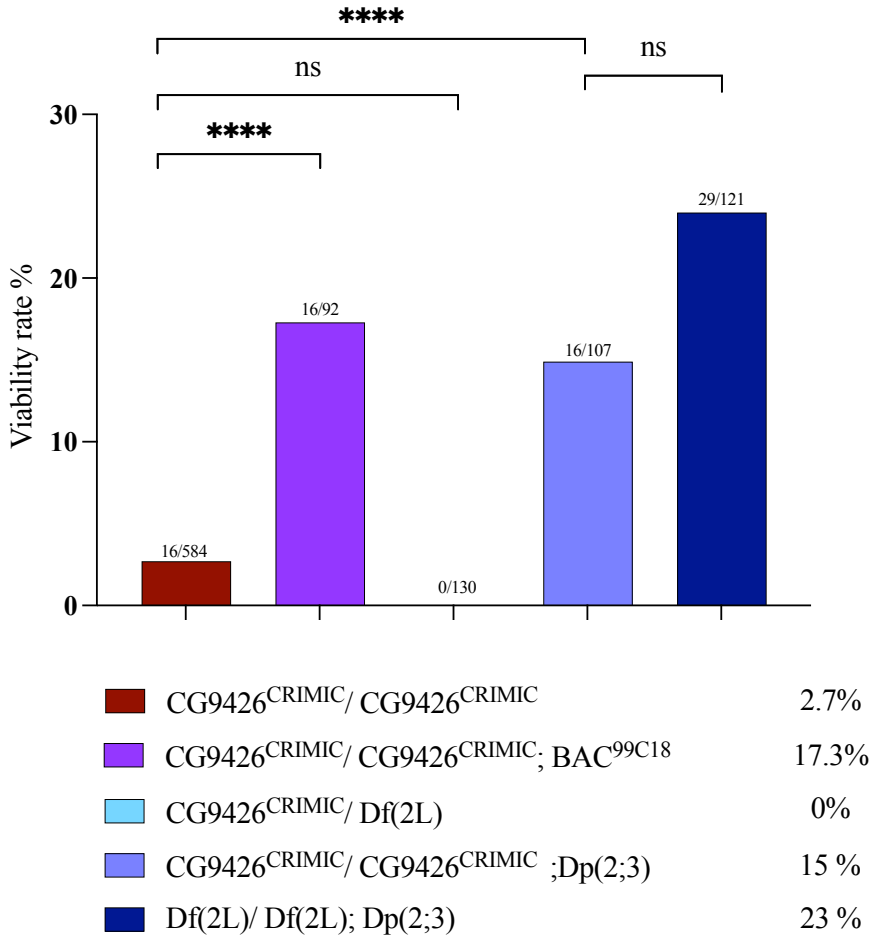

Figure 5.6. Graphical representation of the ratios of viable homozygous of *CG9426* mutants with complementation constructs. Viability rate homozygous $CG9426^{CRIMIC}$ for each construct is given below the graph. The ratios of each genotype is labeled above each bar. Fisher's t-test was conducted to analyze the significance of the difference between the viability rates.
****= $p<0.0001$, ns=non-significant.

5.2. Morphological Analysis of the Mushroom Bodies in $CG9426^{CRIMIC}$ Knockout Mutants in *D. melanogaster*

Morphological analysis of mushroom bodies was also conducted with $CG9426^{CRIMIC}$ line in order to observe whether loss of function of *CG9426* has impact on the learning and memory centers of the flies. Brains of homozygous $CG9426^{CRIMIC}$ adult flies aged between 2 and 5 days were dissected. The mushroom body was visualized in homozygous mutants using an immunohistochemistry method. Mushroom bodies are axon bundles that can be

stained with the anti-FasII antibody that is specific to the axonal protein Fasciclin 2 (Kurusu *et al*., 2002).

Distinct phenotypes observed in $CG9426^{CRIMIC}/CG9426^{CRIMIC}$ mutants are illustrated in Figure 5.7. Some mushroom bodies exhibited a complete loss of lobes (Figure 5.7. I, J, K, and L), while others displayed extreme thinning of α and β lobes (Figure 5.7. F, G, and J). Among the homozygous mutants, 18 out of 27 brains showed undeveloped alpha or beta lobes. As a control, 16 adult brains were dissected from the *yw;;* line. None of the 16 control brains showed lobe thinning or loss.

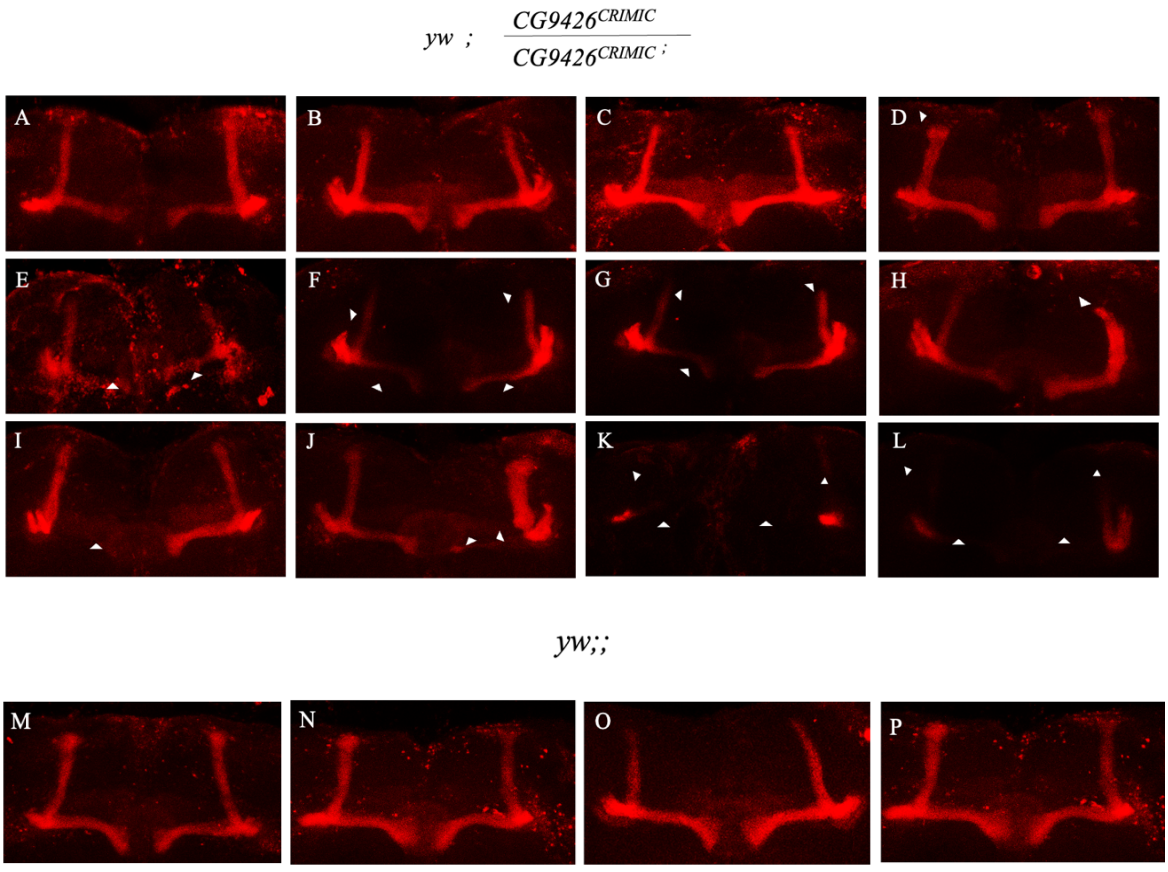

Figure 5.7. Mushroom body morphology of homozygous $CG9426^{CRIMIC}$ mutants. anti-FasII were employed to visualize the mushroom body morphology. A total of 27 flies from the homozygous $CG9426^{CRIMIC}$ line were dissected, and significant phenotypes are depicted in images A to L. As a control, yw flies were used. A total of 16 flies were dissected from this control group, and no defects were observed (M-P).

Mushroom bodies of heterozygous *CG9426*^{CRIMIC} flies were also stained in order to observe whether similar phenotypes in homozygous mutants are present or not. No morphological defect was detected (Figure 5.8). This result indicates that single copy of *CG9426* is sufficient for proper mushroom body formation.

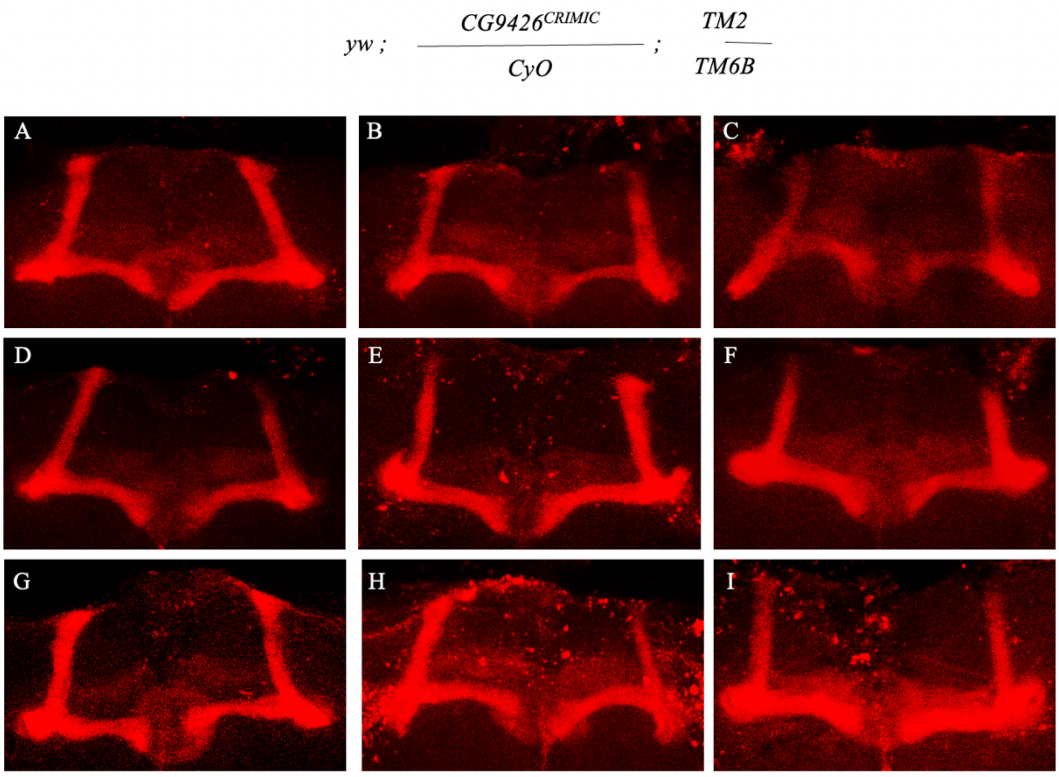

Figure 5.8. Mushroom body morphology of heterozygous *CG9426*^{CRIMIC} / *CyO* flies. A 1:50 dilution of anti-FasII mouse primary antibody and a 1:800 dilution of Alexa Fluor 647-conjugated anti-mouse secondary antibody were employed to visualize the mushroom body morphology. No morphological abnormalities were detected in the heterozygous lines.

5.3. Analysis of CG9426 Expression in the Nervous System of *D. melanogaster*

The aim of this study was to identify the *CG9426* expression pattern in the fly brain for a better understanding of its role in neurodevelopment. For this purpose, the bivalent UAS-Gal4 system was used. To generate the CG9426-Gal4 line, a former member of our lab, Çiğdem Soysal, utilized the Gateway Cloning method to insert the 5' upstream region of *CG9426* into the pBPGUw vector (Addgene#17575, Pfeiffer *et al*., 2008). This vector harbors a Gal4 sequence downstream of the integration site. The resultant plasmid was then

introduced into fly embryos by GenetiVision to generate the line. This line could subsequently be crossed with UAS lines relevant to the focus of the experiment (Figure 5.9). In this study, the CG9426 expression pattern was assessed by crossing the *CG9426*-Gal4 line with *UAS-nLacZ* nuclear reporter and *UAS-mCD8::GFP* membrane reporter lines. Both larval and adult brains were subjected to immunohistochemical staining and subsequently observed using a confocal microscope.

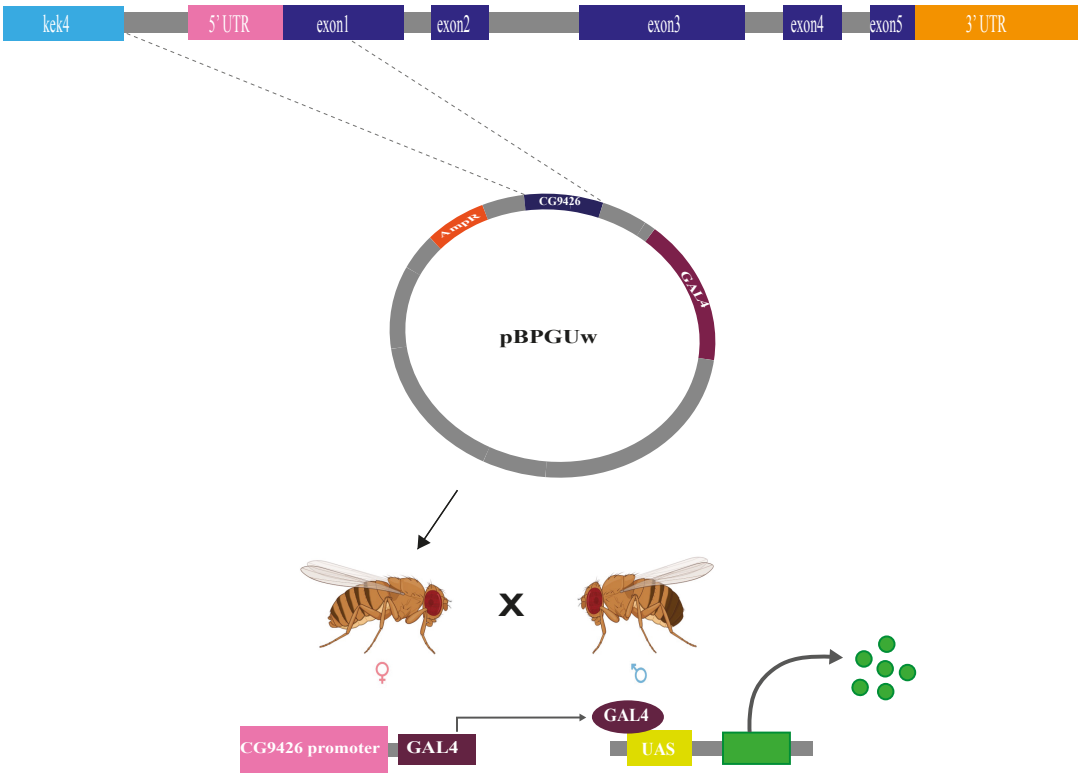

Figure 5.9. Generation of the *CG9426*-Gal4 line. The promoter and 5' UTR region of *CG9426* (pink) were inserted upstream of the GAL4 gene in the pBPGUw vector. The resulting vector was then injected into the embryos to establish the *CG9426*-Gal4 expressing line. This line was used in expression and knockdown analyses through crosses with UAS reporter lines (green).

The expression pattern of *CG9426* in the larval brain was analyzed using the UAS-Gal4 system. The *CG9426*-Gal4 line was crossed with the *UAS*-nlacz line, and brains from 16 larvae were dissected and stained with antibodies specific to Elav, Repo, and βgal. In Figure 5.11 the localization patterns of anti-Elav (the nuclear marker of neurons, blue), anti-Repo (the nuclear marker of glial cells, red) and n-βgal (the nuclear reporter of CG9426 expression, green) are shown. *CG9426* exhibited dense expression where optic lobe neuroblasts reside. The larval brain was kept intact with the eye imaginal discs and expression of *CG9426* was also observed in eye imaginal discs. The localization patterns of n-βgal, Elav, and Repo did not overlap, suggesting that *CG9426* is not expressed in either neurons or glial cells. Comparison with the neuroblast expression pattern scheme (Figure 1.2) indicates that the *CG9426* expression in the larval brain and ventral cord is highly consistent with the neuroblast expression pattern. Further analysis using neuroblast-specific antibodies could provide a more precise understanding of this pattern.

CG9426 is also expressed in the dorsomedial region where two larval brain hemispheres are held together (Figure 5.12) and where Central Brain Type II neuroblasts reside (Figure 1.2).

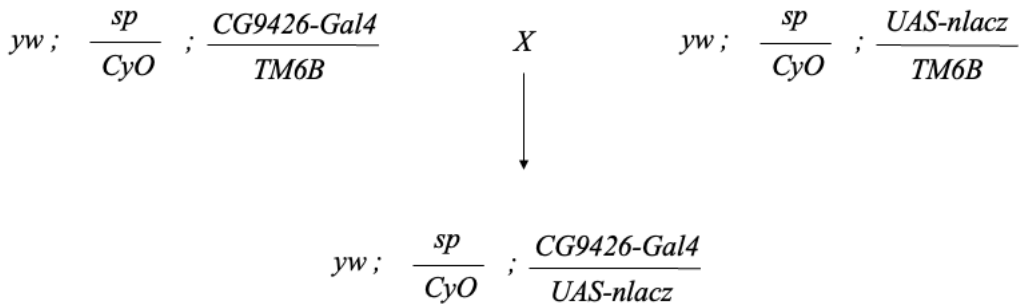

Figure 5.10. Schematic representation of the cross between *CG9426*-Gal4 and UAS-nLacZ lines to analyze the expression pattern of *CG9426*. UAS-nlacz was selected as a nuclear reporter.

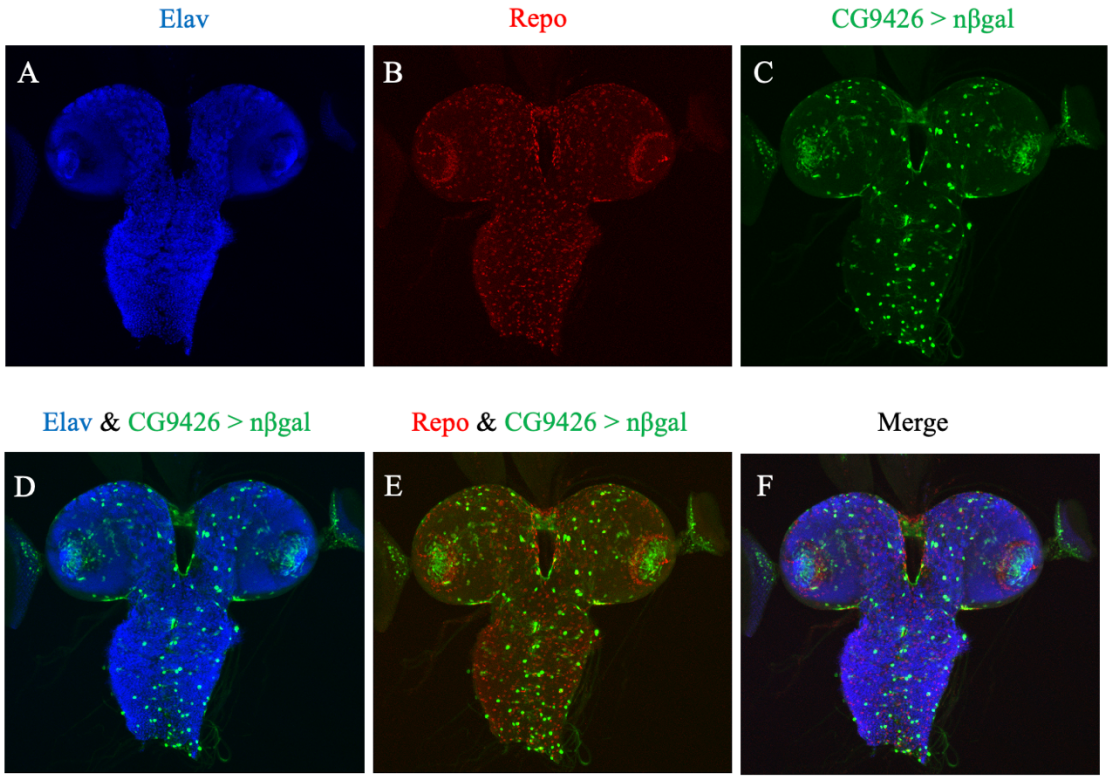

Figure 5.11. Expression pattern analysis of *CG9426* in the larval brain. A) Nuclei of neurons were stained using anti-Elav antibody (blue). B) Nuclei of glia were stained with anti-repo antibody (red). C) *CG9426*-driven nlacz expressing cells ere stained using anti-βgal antibody (green). D) Merged signals from *CG9426* expressing cells and neurons. E) Merged signals from *CG9426* expressing cells and glia. F) Merged signals from neurons, glia, and *CG9426* expressing cells.

In Figure 5.13, the expression pattern of *CG9426* in the adult brain is depicted. *CG9426*-Gal4/UAS-nlacz lines were co-stained with anti-Elav, anti-Repo and anti-βgal antibodies. Anti-Elav was utilized to label the nuclei of neurons and anti-Repo was used to label the nuclei of glial cells. In Figure 5.13 A-C expression patterns of Elav (blue), Repo (red), and *CG9426*-driven β-gal (green) are illustrated. When the colocalization patterns of *CG9426* with neuronal cells and glial cells were combined (Figure 5.13 D-F), it became evident that in the adult fly brain, *CG9426* is predominantly expressed in glial cells but not in neurons.

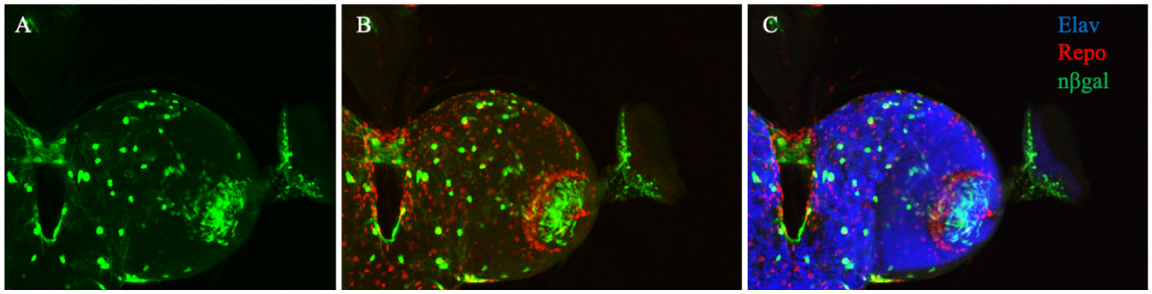

Figure 5.12. Expression pattern of *CG9426* in larval brain hemisphere. A) CG9426 -driven expression of βgal in larvae (green). B) Merged signals from *CG9426*-expressing cells and glia. C) Merged signals from neurons, glia and *CG9426* expressing cells. Staining was performed using a 1:5000 anti-β-galactosidase antibody, and Alexa Fluor 555-linked anti-rabbit antibody was used as the secondary antibody. Anti-Elav and anti-Repo antibody stainings are shown.

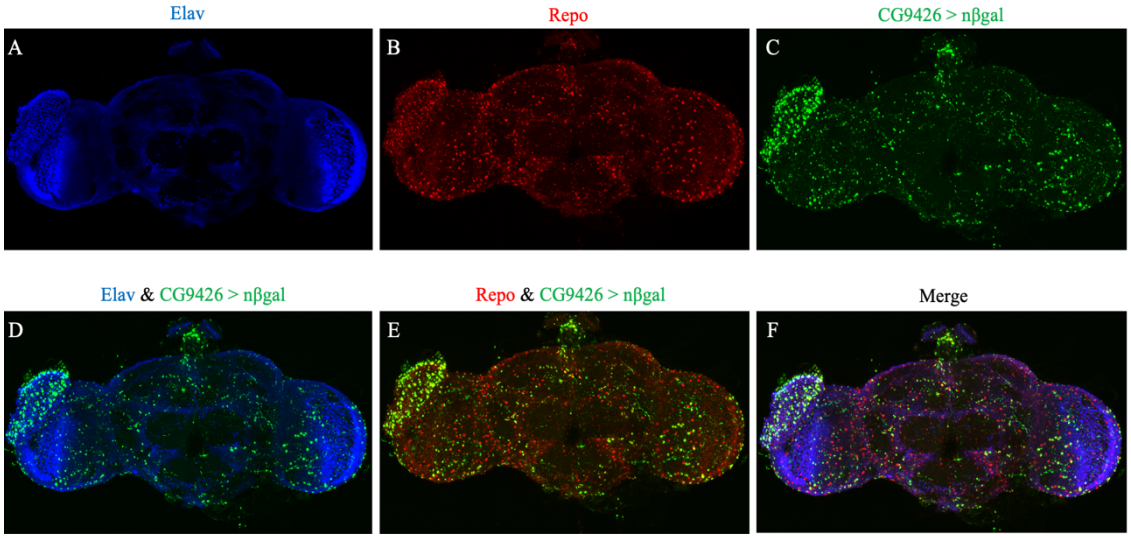

Figure 5.13. Expression pattern of *CG9426* in the adult brain. A) Neural expression pattern in the adult brain (blue). B) Glial expression pattern in the adult brain (red). C) *CG9426* expression in adult brain (green). D) Merged signals of n-βgal expression with the neural marker Elav. E) Merged signals of nβ-gal expression with the glial marker Repo. F) Merged signals corresponding to the expression patterns of nβ-gal, Elav, and Repo.

Although *CG9426* shows a widespread expression pattern in the adult brain a noticeable intensity is observed in the lamina. The neural and glial expression patterns of *CG9426*-Gal4; *UAS*-nlacz line were analyzed separately. Figure 5.14 depicts the signals

from *CG9426* expressing cells do not colocalize with laminal neurons, but rather with laminal glia.

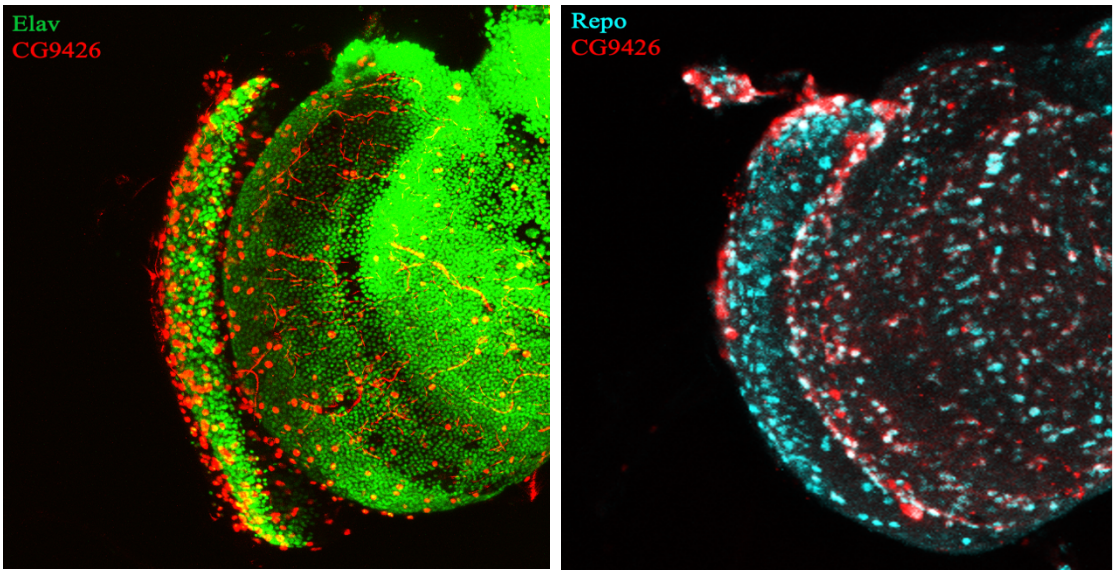

Figure 5.14. Expression pattern of *CG9426* in the optic lobes of the adult brain. The neural cell nuclei were labeled using anti-Elav antibody. The Elav expression pattern is indicated in green. Glial cell nuclei were stained using anti-Repo antibody. The Repo expression pattern is depicted in cyan. The cells expressing lacZ under the control of the *CG9426*-Gal4 × UAS-nlacz cross are highlighted in red.

$$yw\ ;\ \frac{sp}{CyO}\ ;\ \frac{CG9426\text{-}Gal4}{TM6B} \quad X \quad yw\ ;\ \frac{sp}{CyO}\ ;\ \frac{UAS\text{-}mD8::GFP}{TM6B}$$

$$\downarrow$$

$$yw\ ;\ \frac{sp}{CyO}\ ;\ \frac{CG9426\text{-}Gal4}{UAS\text{-}mCD8::GFP}$$

Figure 5.15. Schematic representation of the cross performed with *CG9426*-Gal4 and UAS-mCD8::GFP to analyze the nuclear expression pattern of *CG9426* using a membrane reporter.

.

As shown in Figure 5.13 there is also significant expression of *CG9426* in the dorsolateral region of the central brain, where the mushroom body-the olfactory learning and memory center-resides. To gain a better understanding of the interaction between *CG9426*-expressing cells and mushroom body, the *CG9426*-Gal4 line was crossed with the *UAS*-mCD8::GFP membrane reporter line (Figure 5.15). The desired phenotype was obtained as illustrated in Figure 5.16. For the analysis, 12 flies that were 5-7 days old were dissected and stained with anti-FasII and anti-GFP primary antibodies. The results, depicted in Figure 5.16 C and D, indicate that *CG9426*-expressing cells surround the mushroom body. The membranes of *CG9426*-expressing cells are shown in green, and the α and β lobes of the mushroom body are shown in magenta.

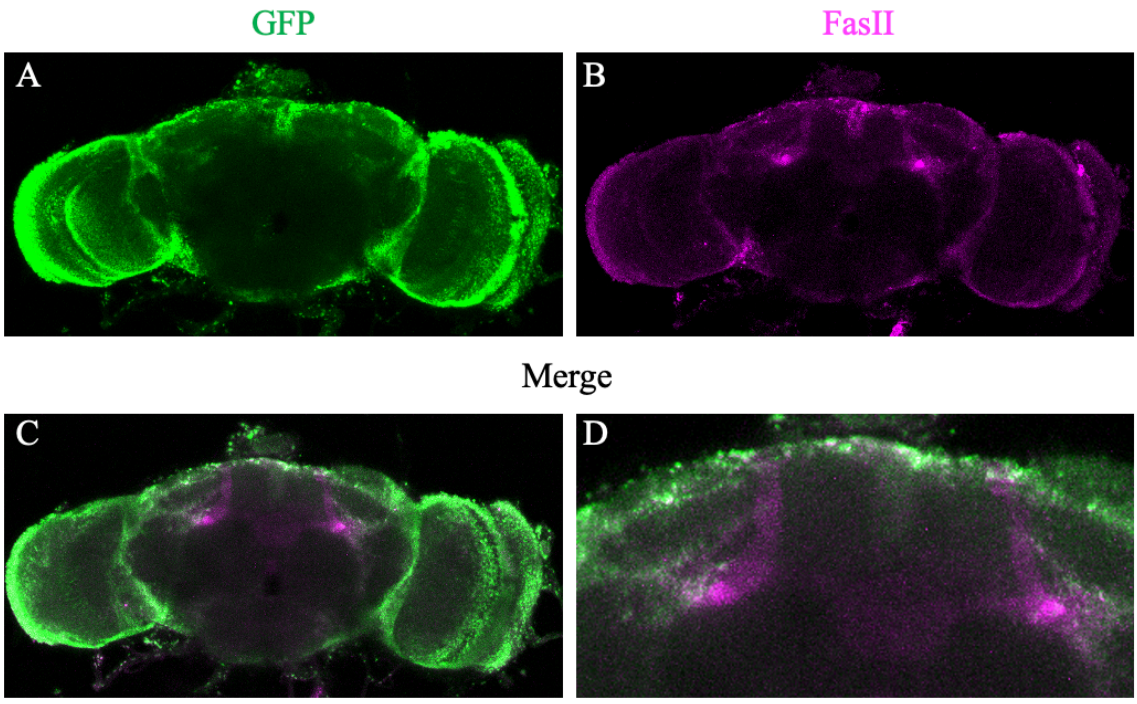

Figure 5.16. Analysis of the *CG9426* expression pattern with membrane-specific reporter *UAS*-mCD8::GFP. The membranous expression pattern of *CG9426*-expressing cells (green) was shown using anti-GFP antibody. α and β lobes of the mushroom body were stained using anti-FasII antibody (green).

Figures 5.13 and 5.16 emphasize the expression in the central brain, which resembles the expression pattern of neuropil glia. To address if *CG9426* expression resembles the neuropil glia, the expression pattern of astrocyte-like glia-specific driver *Alrm*-Gal4 was analyzed with UAS-mCD8::GFP and nlacz reporters to be compared with *CG9426*-Gal4 expression pattern (Figure 5.17). In conclusion, *CG9426* is expressed in glial cells in adult fly brain. Glial cells are as crucial as their neural counterparts for the proper functioning of nervous system.

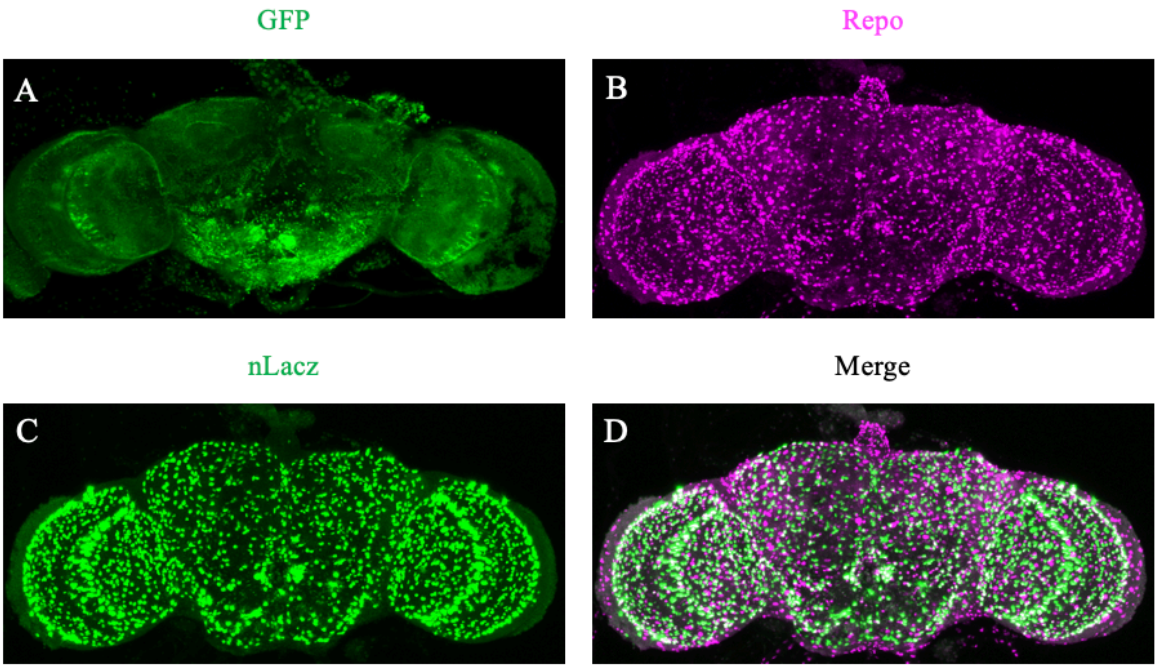

Figure 5.17. Astrocyte-like glia expression pattern. The astrocyte-like glia-specific driver Alrm-Gal4 was used to analyze the astrocyte-like glia expression pattern. A) Membranous expression pattern of astrocyte-like glia obtained through the *Alrm*-Gal4 x *UAS*-mCD8::GFP cross. B-C-D) Nuclear expression pattern analysis of astrocyte-like glia.

5.4. Morphological Analysis of the Mushroom Bodies of the Flies with Cell-Specific Knockdown of *CG9426*

As mentioned earlier, the viability rate of homozygous knockout mutants was very low, which prevented an in-depth morphological and behavioral analysis. Thus, RNAi was used to perform cell-specific knockdown analysis. The knockdown of *CG9426* was performed using the UAS-Gal4 system. The *UAS-CG9426*^{RNAi} line was crossed with Elav-

Gal4 for neuron-specific knockdown, Repo-Gal4 for glia-specific knockdown, Alrm-Gal4 for astrocyte-like glia specific knockdown, *CG9426*-Gal4 for knockdown in *CG9426* expressing cells, and $CG9426^{CRIMIC}$ to provide a knockdown under control of endogenous *CG9426* promoter in heterozygous mutants. The *UAS-*$CG9426^{RNAi}$, which expresses dsRNA for RNAi of CG9426 under UAS control. The BL36303 line which carries the pVALIUM20 vector without any dsRNA sequence inserted into the 3rd chromosome with the same attP docking site for phiC31 integrase-mediated transformation was used as a control to distinguish between possible phenotypes resulting from the knockdown of *CG9426* and those that could arise from transgene insertion.

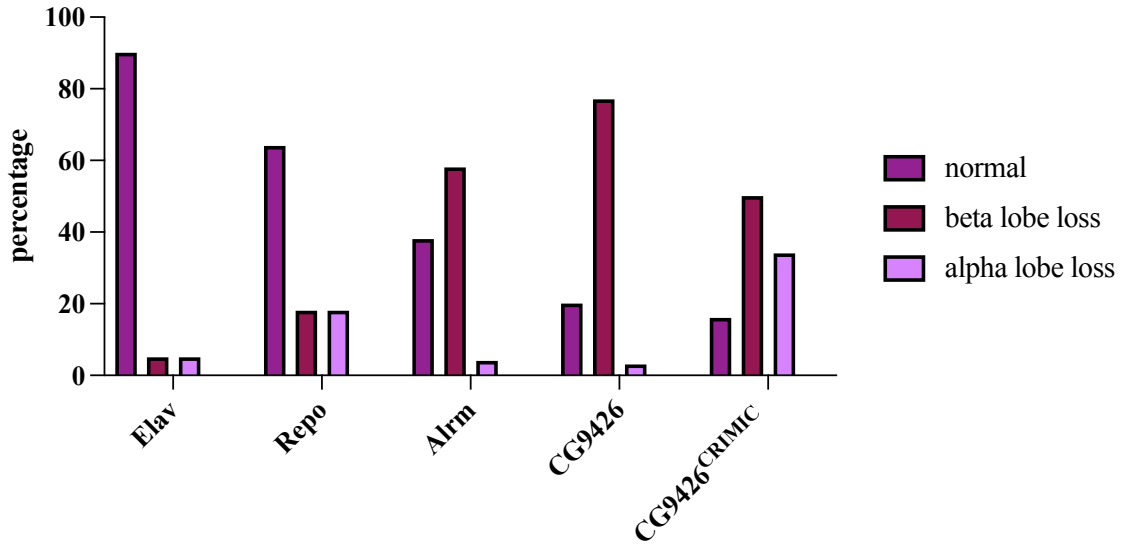

Figure 5.18. Graphical distribution of observed phenotypes in cell specific *CG9426* knockdown. $CG9426^{RNAi}$ line was crossed with *Elav*-Gal4, *Repo*-Gal4, *Alrm*-Gal4, *CG9426*-Gal4 and $CG9426^{CRIMIC}$ lines.

Overall, most frequently observed phenotypes in all progenies were α lobe loss and β lobe loss (Figure 5.18). Percentages of these morphological defects in neuron specific knockdown of *CG9426* were 5% for each. Loss of α and β lobes was more frequently observed in glia specific knockdown of *CG9426* which was 18% for each. Interestingly, although Alrm-Gal4 induced knockdown of *CG9426* solely in a subset of glial cells, prevalence of α lobe loss was much higher when compared to Repo-Gal4 induced knockdown. 58% of mushroom bodies have shown α lobe loss and 4% have shown β lobe

loss. *CG9426*-Gal4 and *CG9426*^{CRIMIC} lines were utilized to observe morphological defects in case of the knockdown of *CG9426* in *CG9426* expressing cells. *CG9426*-Gal4 induced knockdown resulted with 77% α lobe loss and 3% β lobe loss in the mushroom bodies of observed flies. Utilizing *CG9426*^{CRIMIC} construct which induced knockdown of *CG9426* in the flies which already express only one full copy of *CG9426* resulted with 50% α lobe loss and 34% β lobe loss in the mushroom bodies of observed flies.

Table 5.1. Percentages of mushroom body phenotypes observed in cell specific CG9426 knockdown.

Knockdown Driver	normal	α lobe loss	β lobe loss
Elav	90	5	5
Repo	64	18	18
Alrm	38	58	4
CG9426	20	77	3
CG9426^{CRIMIC}	16	50	34

5.4.1. Neuronal-Specific Knockdown of *CG9426*

For neuron-specific knockdown, the Elav-Gal4 and *UAS-CG9426*^{RNAi} lines were crossed, and 9 brains were dissected. These brains were stained with mushroom body specific anti-FasII antibody. In addition, 9 pairs of mushroom bodies from the *Elav-Gal4/BL36303* line were used as the control in this experiment (Figure 5.19). Among the brains analyzed, one exhibited a complete loss of α and β lobes, while no other distinct phenotypes were observed.

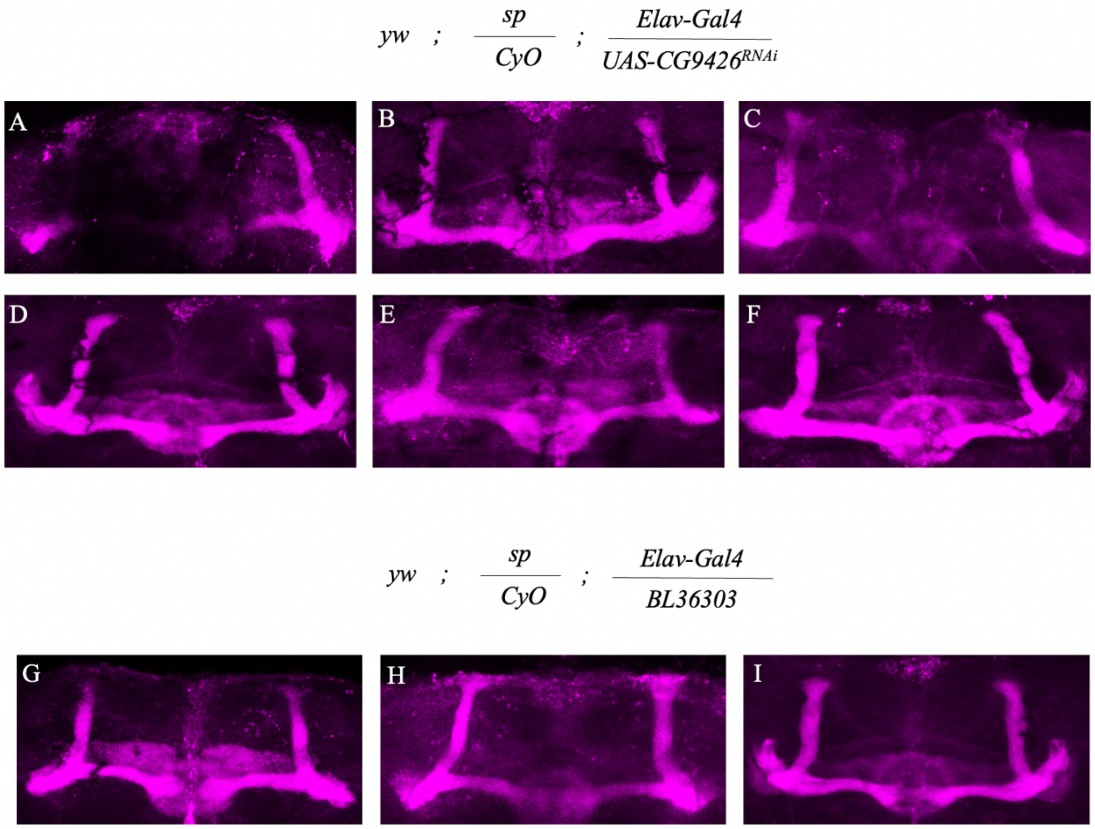

Figure 5.19. Mushroom body morphology of flies with *CG9426* knockdown in neural cells. To visualize the mushroom bodies, a 1:50 dilution of anti-FasII mouse primary antibody and a 1:800 dilution of Alexa Fluor 647-conjugated anti-mouse secondary antibody were utilized.

5.4.2. Glia-Specific Knockdown of *CG9426*

For glia-specific knockdown of *CG9426*, *Repo*-Gal4 and *UAS-CG9426*^{RNAi} lines were crossed. Mushroom bodies from 11 brains were stained with mushroom body specific anti-FasII antibody and visualized. Mushroom bodies from 15 flies of the *Repo*-Gal4/BL36303 line were used as the control (Figure 5.20). Two of the flies showed thinned lobes (Figure 5.13 C-D); no other distinct morphological defect could be noted.

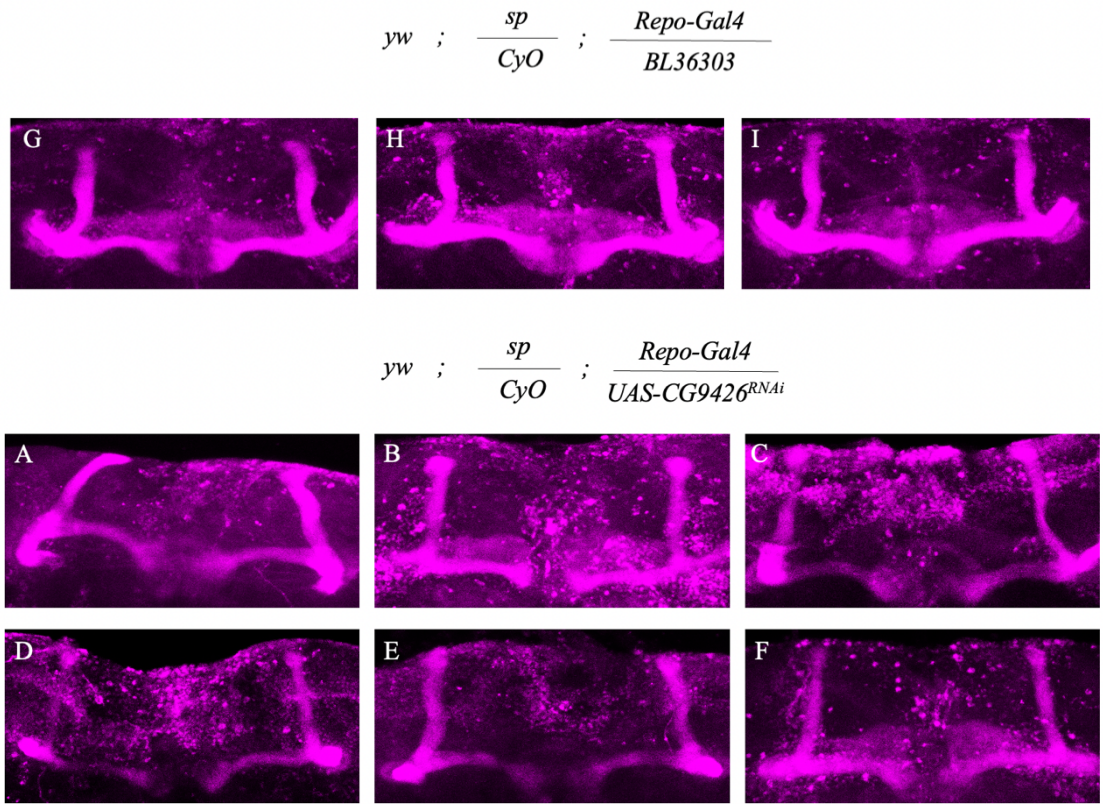

Figure 5.20. Morphological analysis of knockdown of *CG9426* in glial cells by *Repo*-Gal4 x *UAS-CG9426*^{RNAi} cross. 1:50 anti-FasII mouse primary antibody and 1:800 Alexa mouse 647 secondary antibody were used to analyze the mushroom boy morphology.

5.4.3. Astrocyte-like Glia Specific Knockdown of *CG9426*

For astrocyte-like glia-specific knockdown, *Alrm*-Gal4 and *UAS-CG9426*^{RNAi} lines were crossed. Mushroom bodies of 11 flies were visualized using anti-FasII antibody. Mushroom bodies from 12 flies of the *Alrm*-Gal4/ BL36303 line were used as the control (Figure 5.21). Significant defects in the β lobe development were observed in the mushroom bodies of 7 flies (Figure 5.14. A, C, D, G-I).

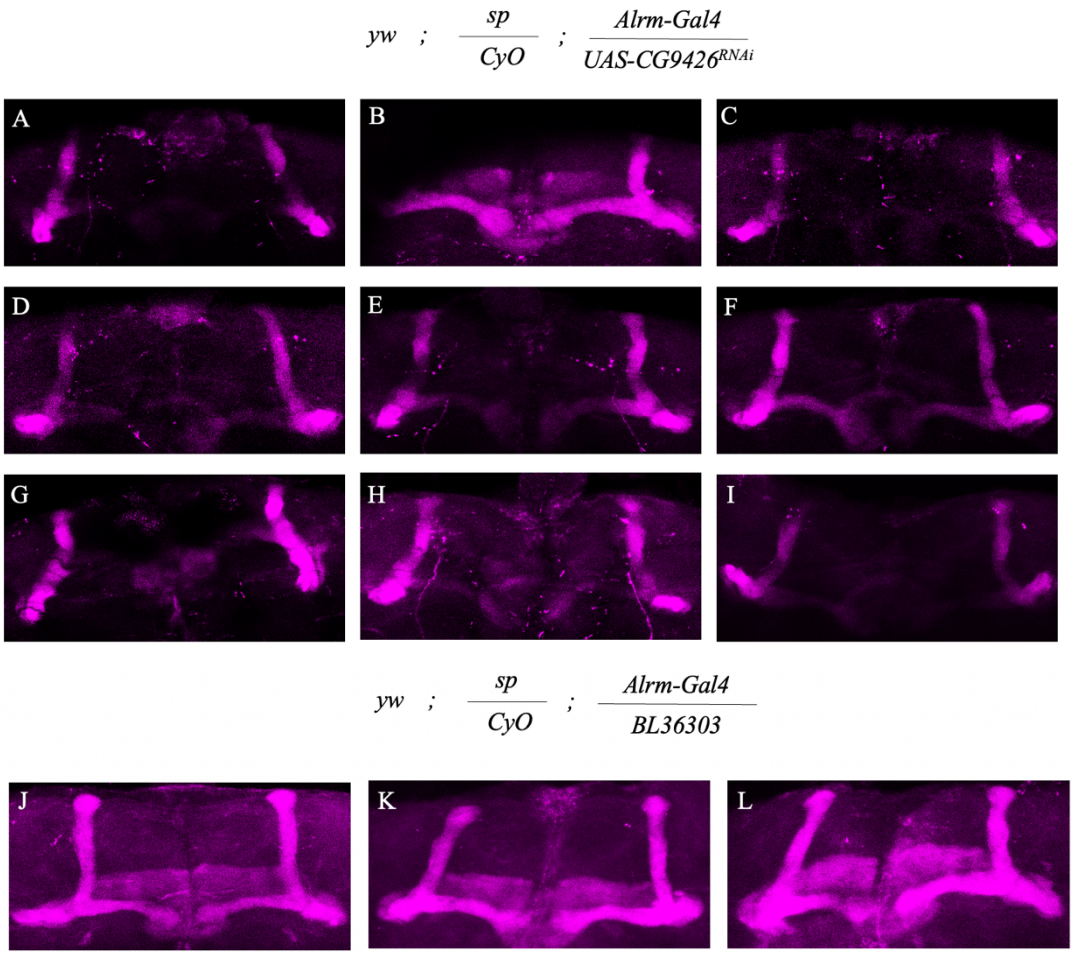

Figure 5.21. Morphology of the mushroom bodies of the flies with *CG9426* knockdown in astrocyte-like glial cells. 1:50 anti-FasII mouse primary antibody and 1:800 Alexa Fluor 647 conjugated anti-mouse secondary antibody were used to analyze the mushroom bodies.

5.4.4. Knockdown of *CG9426* in CG9426-Expressing Cells

To specifically knockdown *CG9426* in the cells where it is normally expressed *CG9426*-Gal4 and *UAS-CG9426*^{RNAi} were crossed. 30 brains of the progeny were dissected and stained with mushroom body specific anti-FasII antibody (Figure 5.22). Among the samples, one brain showed complete loss of α and β lobes (Figure 5.22 L), another exhibited loss of only β lobes (Figure 15.22 K), and six of them displayed thinned β lobes (A, E, F, I-J).

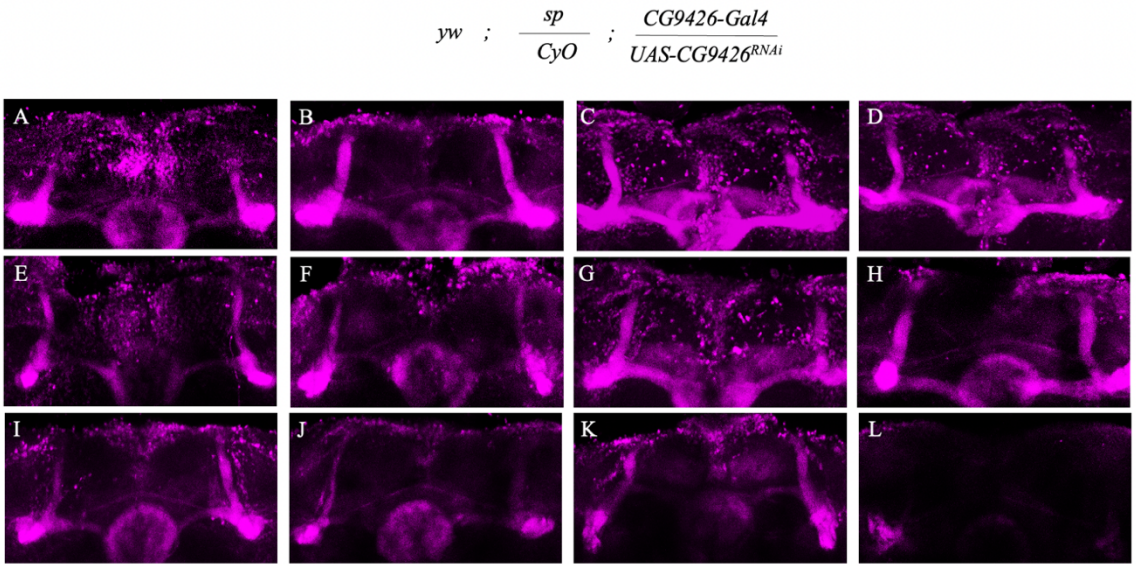

Figure 5.22. Mushroom body morphology of the flies with *CG9426* knockdown in *CG9426*-expressing cells. Anti-FasII mouse primary antibody (1:50) and Alexa Fluor 647 conjugated anti-mouse secondary antibody (1:800) were employed to visualize the mushroom bodies.

5.4.5. Knockdown of *CG9426* in *CG9426*-Expressing Cells of $CG9426^{CRIMIC}$

To achieve knockdown of *CG9426* under control of its endogenous promoter in heterozygous mutants, the $UAS\text{-}CG9426^{RNAi}$ line was crossed with the $CG9426^{CRIMIC}$ line. A total of 26 brains were dissected, stained with mushroom body specific anti-FasII antibody. 12 of them are presented in Figure 5.23. Developmental defects in α and β lobes can be observed in Figure 5.23 A, E and K. Some samples demonstrated a reduction in the FasII signal strength (Figure 5.23 E-I, L).

5.5. Generation of Humanized Fly Lines Expressing IPP^{WT} and IPP^{G397R}

To clone the plasmids containing the IPP gene, the Gateway Cloning method was employed. Initially, IPP was amplified from cDNA, and then attB sites were introduced to the IPP sequence through PCR as detailed in Section 4.1. IPP, flanked by attB sites on both its 5' and 3' ends, was subsequently inserted into the pDonr207 vector containing an attP site, resulting in the generation of the plasmid $pDONR207\text{-}IPP^{WT}$ with attR sites (see Section 4.4 for details).

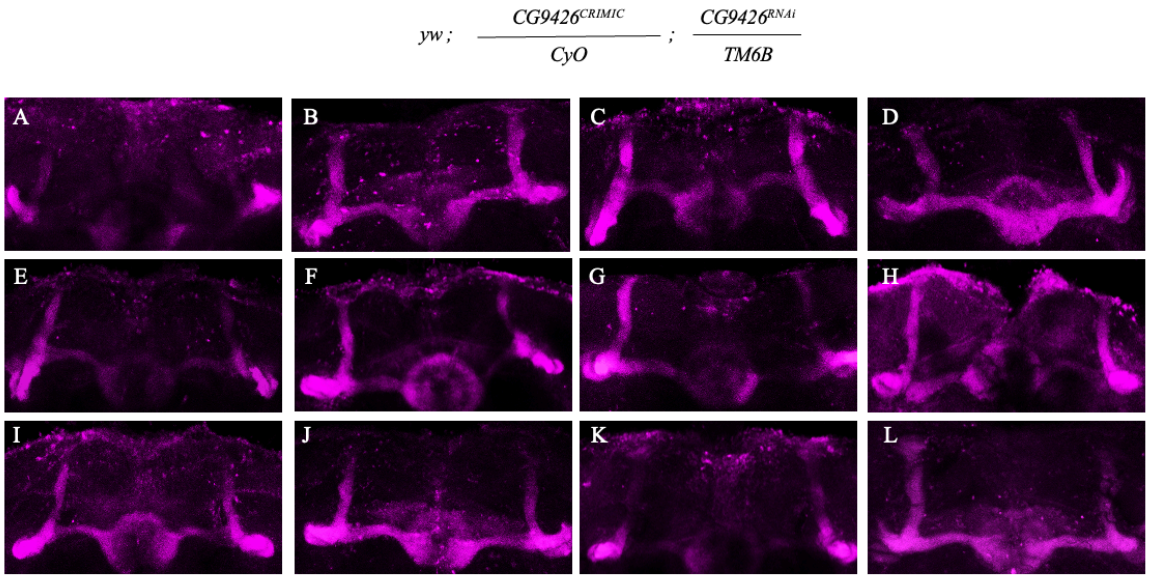

Figure 5.23. Morphology of mushroom bodies of flies with *CG9426* knockdown under control of endogenous *CG9426* promoter. A 1:50 dilution of anti-FasII mouse primary antibody and a 1:800 dilution of Alexa Fluor 647-conjugated anti-mouse secondary antibody were used to visualize the mushroom bodies.

As one of the objectives of the study was to understand whether the p.G397R mutation observed in one of the Iranian families had an impact on the function of IPP, the mutation was introduced using the site-directed mutagenesis method via PCR as explained in Section 4.5. The plasmids pDONR207_IPP^{WT} and pDONR207_IPP^{G397R}, containing the wildtype and mutant IPP sequences, respectively, were then utilized to clone these genes into the pUASg::HA vector. This vector allows for the expression of genes of interest under the control of the UAS promoter and in frame with 3xHA tag within the genomes of flies carrying the attP site, as outlined in Section 4.7. The correctness of the expression vectors was confirmed through restriction digestion (Figure 5.24) and sequencing before being sent for injection into the embryos of flies with the w^{1118};; background.

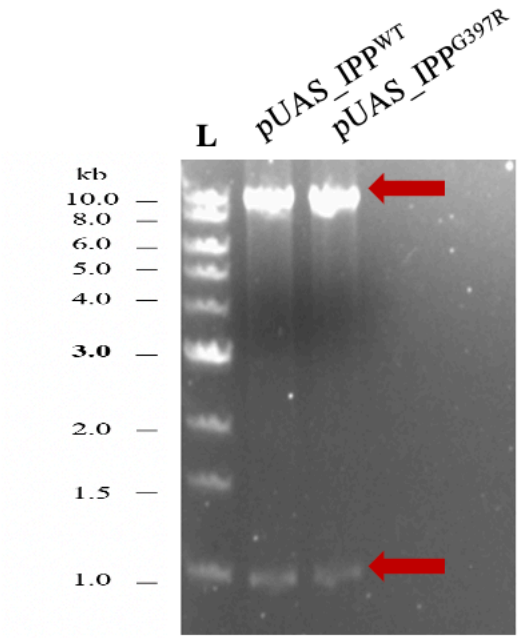

Figure 5.24. Electrophoretogram of pUASg_IPP::HA plasmids digested with the *Pst*I endonuclease. Bands corresponding to sizes of 10 kb and 1 kb, confirming the successful insertion, are indicated with red arrows.

The obtained transgenic flies were balanced and then crossed with Actin-Gal4 to verify the expression of HA-tagged IPP in both male and female flies using the Western Blot method (Figure 5.25). The expected molecular weight of IPP is 66 kDa. Surprisingly, no band corresponding to this size was detected in males, and the band corresponding to this size in females was also present in the negative control that lacks UAS-IPP::HA sequence in its genome. The bands observed in 65-70 kDa were considered to be nonspecific. As a conclusion, no specific signal of IPP-HA was detected using Western Blot analysis.

The expression of HA-tagged IPP in transgenic lines was subsequently addressed using the immunohistochemistry method. *UAS-IPP::HA* lines were crossed with the long GMR-Gal4 line. Long GMR-Gal4 is a robust driver for the *glass (gl)* gene, which is expressed in photoreceptor cells. Eye imaginal discs of the 3rd instar larval progeny were dissected and stained with anti-Elav and anti-HA antibodies. However, no specific HA signal was detected in the photoreceptor cells.

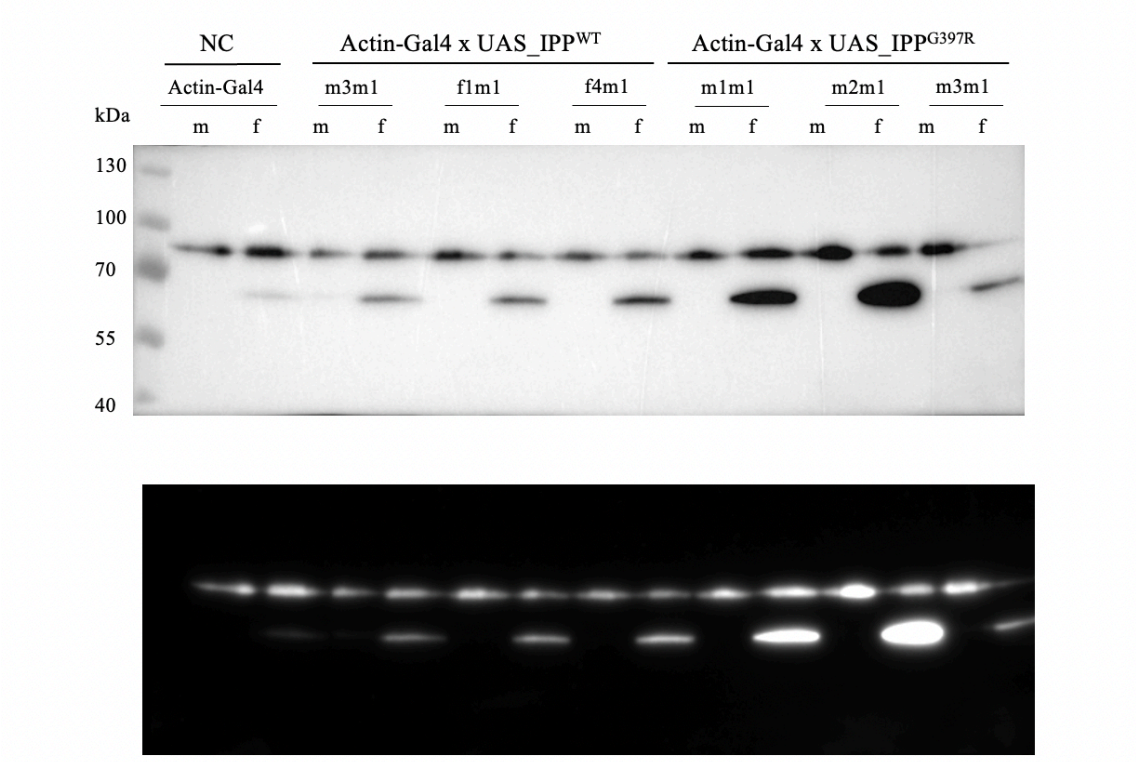

Figure 5.25. Western Blot of lysates of transgenic flies that were expected to express HA-tagged IPP under control of Actin-Gal4 driver. A 1:5000 dilution of anti-HA (rabbit) primary antibody was used, followed by 1:5000 HRP-linked anti-rabbit secondary antibody. The Actin-Gal4 line was used as the negative control.

Next, IPP expression was assessed using an anti-IPP antibody. Eye imaginal discs from the 3rd instar larval progeny of the *longGMR*-Gal4 x *UAS*-IPP^{WT} and *longGMR*-Gal4 x *UAS*-IPP^{G397R} crosses were dissected and subjected to staining with both anti-IPP and anti-Elav antibodies. The longGMR-Gal4 line served as a negative control. Eight imaginal discs were mounted and visualized from each line. Interestingly, an IPP-specific signal could be detected in *UAS-IPP^{WT}::HA* line, but not in the *UAS-IPP^{G397R}::HA* when expressed under the control of the *longGMR*-Gal4 driver.

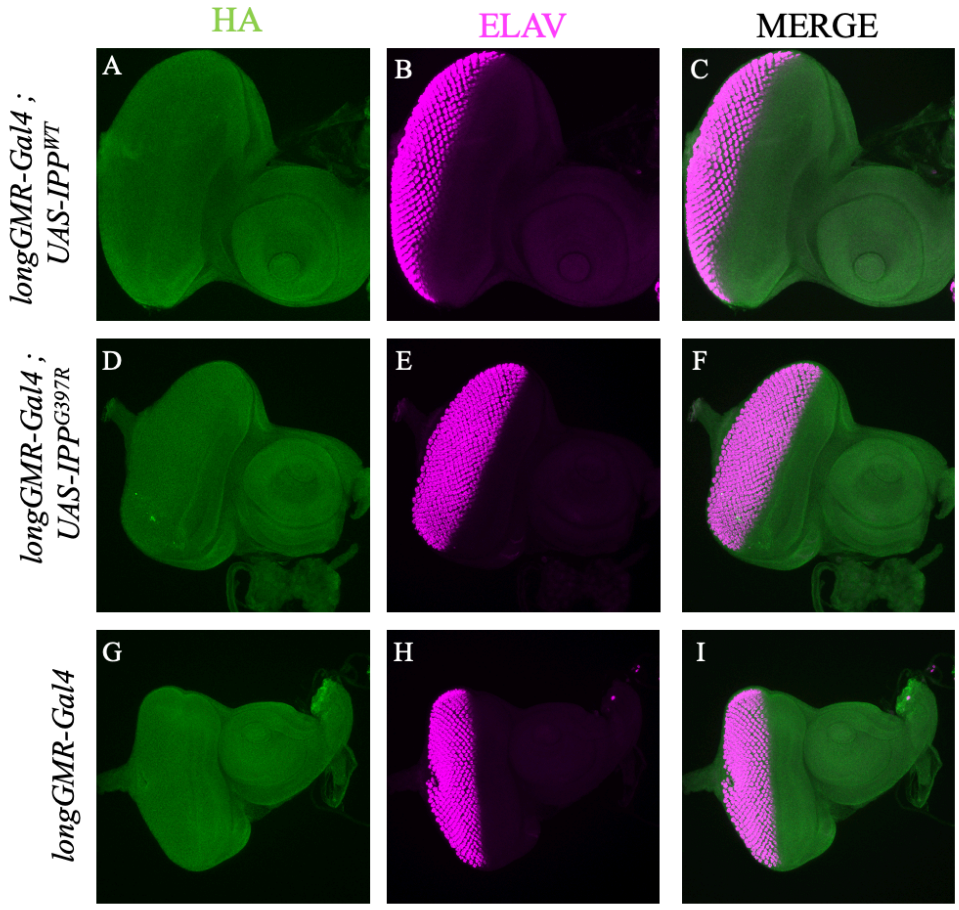

Figure 5.26. IPP expression analysis in eye imaginal discs of transgenic larvae. The anticipated expression of IPP was regulated by the eye-specific longGMR-Gal4 driver. Anti-HA antibody was employed to monitor IPP expression, as IPP is tagged with 3xHA. However, no distinct HA expression could be observed in IPPWT and IPPG397R lines (green). Neural expression in eye imaginal discs was visualized using anti-Elav antibody (magenta).

5.6. Rescue Assay for the *CG9426*^{CRIMIC} Knockout Lines

Drosophila is a convincing model for investigating neurodevelopmental diseases. In this study, we aimed to have a better understanding on the role of *IPP* mutation in ID, utilizing *Drosophila* as a model organism. While the *IPP* gene possesses a predicted ortholog in flies based on the sequence similarity known as CG9426, the functional orthology between these two genes needed further exploration. To address this, a rescue assay was carried out.

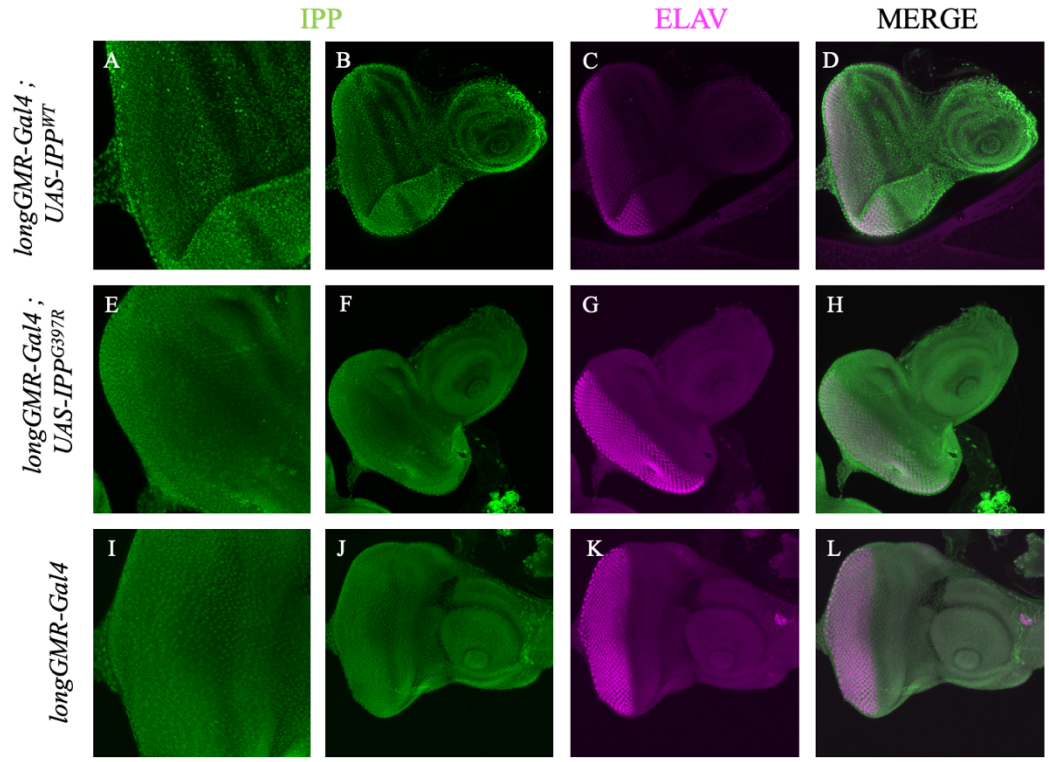

Figure 5.27. IPP^{WT}::HA and IPP^{G397R}::HA expression analysis in eye imaginal discs of transgenic larvae under the control of eye-specific longGMR-Gal4 driver. Anti-IPP primary antibody was utilized for IPP expression visualization. anti-Elav antibody was employed to label photoreceptor cells within the eye imaginal discs (magenta).

The knockout mutant kindly provided by H. Bellen, was generated through the integration of the CRIMIC cassette (Kanca *et al*., 2017; also see 1.11 for details) in the intronic region of *CG9426*. This insertion resulted in the disruption of transcription due to the presence of polyA sequence. Notably, the CRIMIC cassette incorporates a Gal4 gene, which enables transcription of Gal4 under the control of the endogenous *CG9426* promoter and can be used to express a transgene or a reporter using the Gal4-UAS system. To ascertain the functional orthology between IPP and CG9426, *UAS-IPP^{WT}* and *UAS-IPP^{G397R}* lines were generated as described above.

5.6.1. Rescue of Low Viability Rate in Homozygous *CG9426^{CRIMIC}* Mutant with *UAS-IPP::HA* and *BAC* Constructs

The rescue ratio for the low viability rate of homozygous *CG9426^{CRIMIC}* mutants by *IPP^{WT}::HA* was analyzed using the scheme depicted in Figure 5.30. To achieve this, a balanced *C9426^{CRIMIC}* line was crossed with a balanced *UAS-IPP^{WT}::HA* line, generating an F1 generation with the *C9426^{CRIMIC}* allele on the second chromosome and the *UAS-IPP^{WT}::HA* transgene on the third chromosome. Subsequently, the F_1 generation was crossed with the balanced *CG9426^{CRIMIC}* line.

The F_2 generation can be divided into three groups: F_2.1 (heterozygous *C9426^{CRIMIC}* with *UAS-IPP^{WT}::HA* on the 3rd chromosome), F_2.2 (homozygous *C9426^{CRIMIC}* with *UAS-IPP^{WT}::HA* on the 3rd chromosome), and F_2.3 (heterozygous or homozygous *C9426^{CRIMIC}* without *UAS-IPP^{WT}::HA* on the 3rd chromosome). Importantly, homozygous *CyO/CyO* lines, which are lethal, are not shown on the scheme and are excluded from the calculations.

As previously mentioned, homozygous *CG9426^{CRIMIC}* mutants could not reach the adult stage, resulting in a viability rate of 2.7%. The impact of the human *IPP^{WT}* gene on the viability rate of homozygous *CG9426^{CRIMIC}* was determined by calculating the ratio of F_2.2 to the sum of F_2.1 and F_2.2. GFP fluorescence in the eyes was utilized as a marker for the *CG9426^{CRIMIC}* allele, while w^+ phenotype was used as the marker of *UAS-IPP^{WT}::HA* transgene. The selection against the CyO balancer, which bears a curly wing marker, was applied to isolate homozygous *CG9426^{CRIMIC}* mutants.

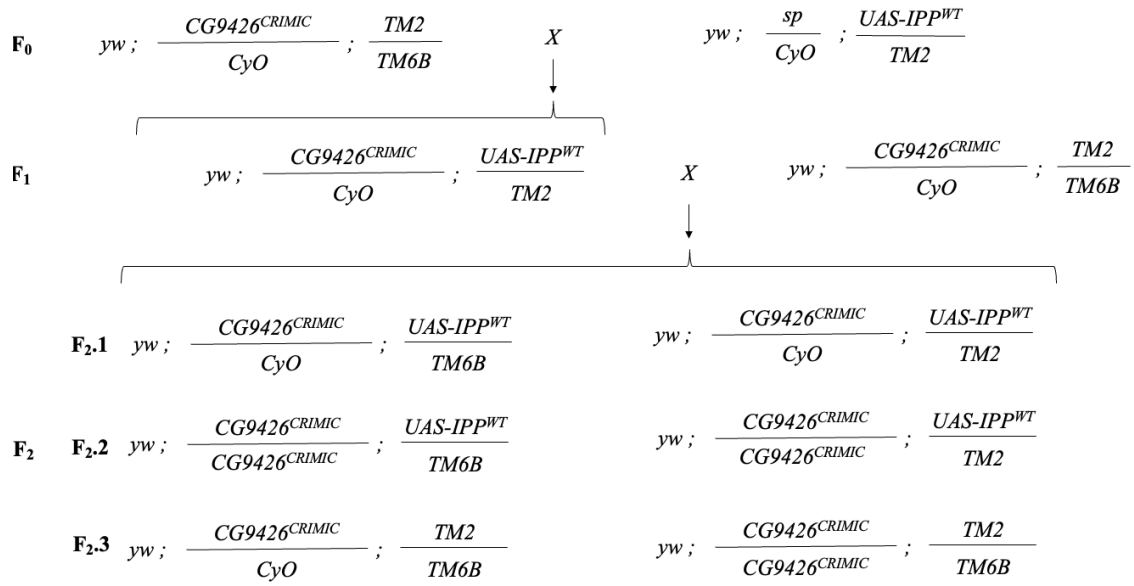

Figure 5.28. Cross scheme to analyze the rescue of the low viability rate of homozygous *CG9426^{CRIMIC}* mutants by *UAS-IPP*. Heterozygous *CG9426^{CRIMIC}* line was crossed with the UAS-IPP^{WT} line. The resulting progeny that carried both constructs were subsequently crossed with heterozygous *CG9426^{CRIMIC}* line. The ratio of F2.2 to the sum of F2.1 and F2.2 was calculated to quantify the effect of *UAS-IPP^{WT}* on the viability rate of homozygous mutants.

Based on the observed phenotypes, among the 114 flies, 21 were identified as homozygous for *CG9426^{CRIMIC}* and carried the *UAS-IPP^{WT}::HA* transgene. This data is presented in the pink column of Figure 5.30. The presence of the *UAS-IPP^{WT}* construct led to an increase in the viability rate of homozygous *CG9426^{CRIMIC}* flies from 2.7% to 18.42% which is as significant as the rescue results with the *BAC^{99C18}* construct.

Similarly, the rescue ratio of low viability rate in homozygous *CG9426^{CRIMIC}* mutants by *IPP^{G397R}::HA* was analyzed using the scheme depicted in Figure 5.29. Initially, a balanced heterozygous *C9426^{CRIMIC}* line was crossed with a balanced *UAS-IPP^{G397R}::HA* line to generate a line that carried *C9426^{CRIMIC}* on the second chromosome and *UAS-IPP^{G397R}::HA* on the third chromosome in the F_1 generation. This F_1 generation was then crossed with the balanced CG9426^{CRIMIC} line. The resulting F_2 generation can be categorized into three groups: F_2.1 (heterozygous *C9426^{CRIMIC}* with *UAS-IPP^{G397R}* on the 3rd chromosome), F_2.2 (homozygous *C9426^{CRIMIC}* with *UAS-IPP^{G397R}::HA* on the 3rd chromosome), and F_2.3 (heterozygous or homozygous *C9426^{CRIMIC}* without *UAS-IPP^{G397R}::HA* on the 3rd

chromosome). Note that homozygous *CyO/CyO* lines should be lethal, thus they are not depicted on the scheme and are not taken into consideration in calculations.

The effect of the human gene *IPP^{G397R}::HA* on the low viability rate of homozygous *CG9426^{CRIMIC}* was calculated by comparing the ratio of F_2.1 to sum of F_2.1 and F_2.2 with the ratio of homozygous *CG9426^{CRIMIC}* flies in the *CG9426^{CRIMIC}/CyO* line. The ratio of homozygous *CG9426^{CRIMIC}* lines was tracked similarly as described above for the *UAS-IPP^{WT}::HA* line. According to the observed phenotypes, 15 of the 109 flies were homozygous *CG9426^{CRIMIC}* carrying the *UAS-IPP^{G397R}::HA* transgene. As indicated in the plum-colored column in Figure 5.30, the presence of the *UAS-IPP^{G397R}::HA* construct increased the viability rate of homozygous *CG9426^{CRIMIC}* from 2.7% to 13.7%.

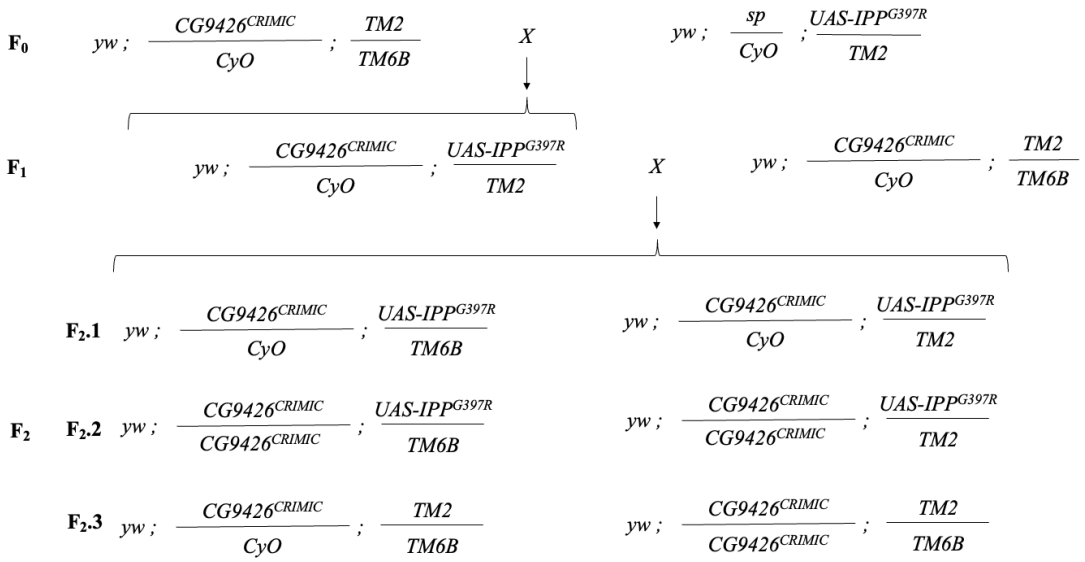

Figure 5.29. Cross scheme to analyze the rescue of low viability rate by *UAS-IPP*. A balanced heterozygous *CG9426^{CRIMIC}* line was crossed with a balanced *UAS-IPP^{WT}::HA* line. The resulting progeny carrying both constructs were then crossed with a balanced heterozygous *CG9426^{CRIMIC}* line. The ratio of F2.2 over the sum of F2.1 and F2.2 was calculated to measure the viability rate of homozygous mutants.

Overall, IPP expression compensated the low viability rate and decreased the ratio of mushroom body defects in *CG9426* knockout mutants. These results support the idea that CG9426 and IPP are functional orthologs, and *Drosophila melanogaster* can be a suitable model to understand the causative of role of IPP in intellectual disability.

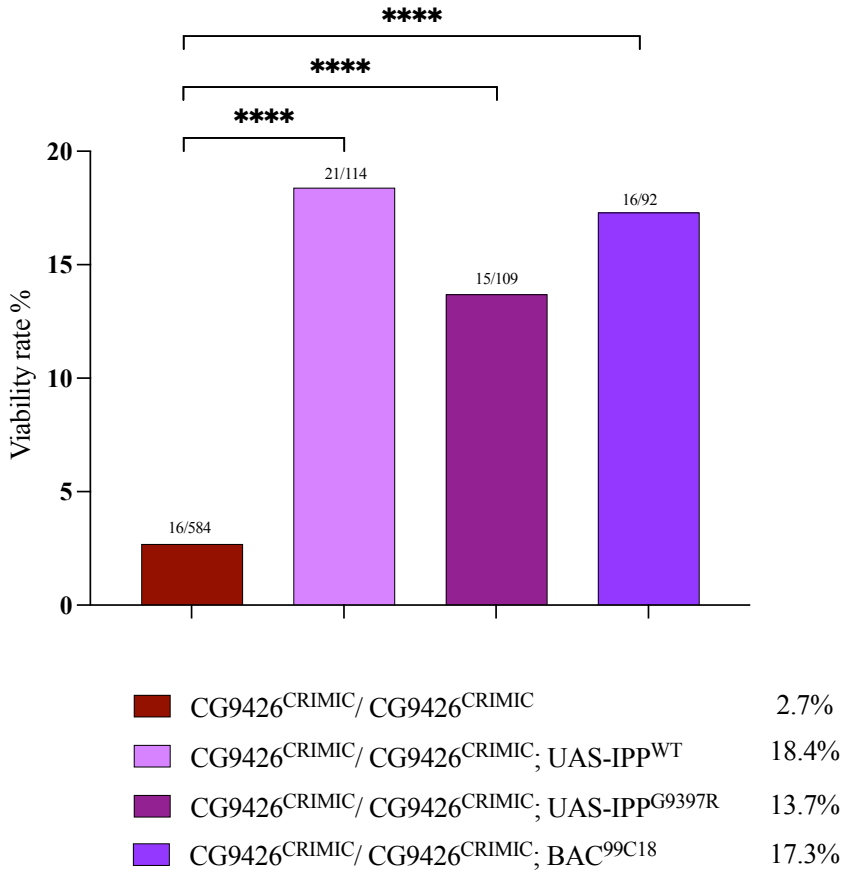

Figure 5.30. Graphical representation of the ratios of viable homozygous of *CG9426* mutants with transgenic lines constructs. The viability rate of homozygous *CG9426*^{CRIMIC} for each construct is indicated below the graph. Fisher's t-test was performed to analyze the significance of the differences between the viability rates. ****= $p<0.0001$, ns=non-significant.

5.6.2. Rescue of Mushroom Body Phenotype

Analysis of morphological defects in the *CG9426^{CRIMIC}* homozygous mutants was complicated due to the very low viability of these flies. The homozygous mutants that reached adulthood did not survive for more than 5-7 days. Subsequently, the mushroom bodies of homozygous *CG9426^{CRIMIC}* lines carrying the transgenic constructs *UAS-IPP^{WT}::HA* and *UAS-IPP^{G397R}::HA* were examined. Table 5.2 presents the distribution of the most frequently observed phenotypes, which included α lobe loss, β lobe loss, and β lobe fusion. A total of 27 brains were dissected from adult flies of the *CG9426^{CRIMIC}/CG9426^{CRIMIC}* line (representative images for the most frequent phenotypes: Figure 5.32 A, D, G), 29 from the *CG9426^{CRIMIC}/CG9426^{CRIMIC}; UAS-IPP^{WT}::HA* line (representative images for the most frequent phenotypes: Figure 5.32 B, E, H), and 27 from the *CG9426^{CRIMIC}/CG9426^{CRIMIC}; UAS-IPP^{G397R}::HA* line (representative images for the most frequent phenotypes: Figure 5.32 C, F, I).

Table 5.2. Distribution of phenotypes observed in homozygous *CG9426^{CRIMIC}* mutants rescued with transgenic *UAS-IPP::HA* constructs. yw;; line was used as a negative control.

genotype	normal	α lobe loss	β lobe loss	β lobe fusion	total
yw;;	18	1	-	-	19
CG9426^{CRIMIC}/ CG9426^{CRIMIC};	9	9	9	0	27
CG9426^{CRIMIC}/ CG9426^{CRIMIC}; UAS-IPP^{WT}	15	3	6	5	29
CG9426^{CRIMIC}/ CG9426^{CRIMIC}; UAS-IPP^{G397R}	13	9	5	0	27

1:50 anti-FasII (mouse) primary antibody and 1:800 Alexa Fluor 647 conjugated with anti-mouse secondary antibody were utilized to stain the α and β lobes of the mushroom body. The ratios of morphological phenotypes observed in homozygous *CG9426^{CRIMIC}/CG9426^{CRIMIC}* mutants were 33% normal, 33% α lobe loss, and 33% β lobe loss. For *CG9426^{CRIMIC}/CG9426^{CRIMIC}; UAS-IPP^{WT}::HA* constructs, the ratios of morphological mushroom defects were 50% normal, 10% α lobe loss, 20% β lobe loss, and 20% β lobe fusion. In the case of *CG9426^{CRIMIC}/CG9426^{CRIMIC}; UAS-IPP^{G397R}::HA* constructs, the ratios of morphological mushroom defects were 47% normal, 33% α lobe loss, and 20% β lobe loss. Schematic representations of these ratios are illustrated in Figure 5.31. Although expression of *IPP^{WT}* and *IPP^{G397R}*, in the homozygous *CG9426^{CRIMIC}/CG9426^{CRIMIC}* mutants increased the percentage of normal mushroom body, they failed to rescue the whole phenotype. In addition to that, beta lobe fusion was observed in 20% of the mushroom bodies from *CG9426^{CRIMIC}/CG9426^{CRIMIC}; UAS-IPP^{WT}::HA* line which was not noted in the loss of function experiments.

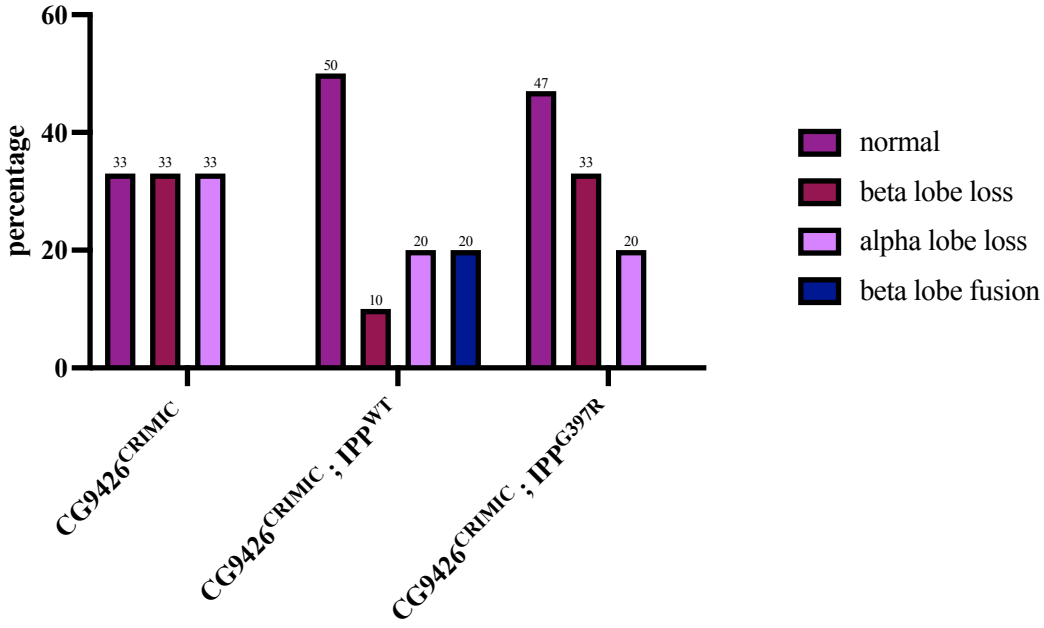

Figure 5.31. Graphical representation of the mushroom body phenotypes observed in knockout mutants and rescue constructs. Percentages of most frequently observed mushroom body phenotypes are given above each column: normal (purple), beta lobe loss (burgundy), alpha lobe loss (lilac), beta lobe fusion (indigo).

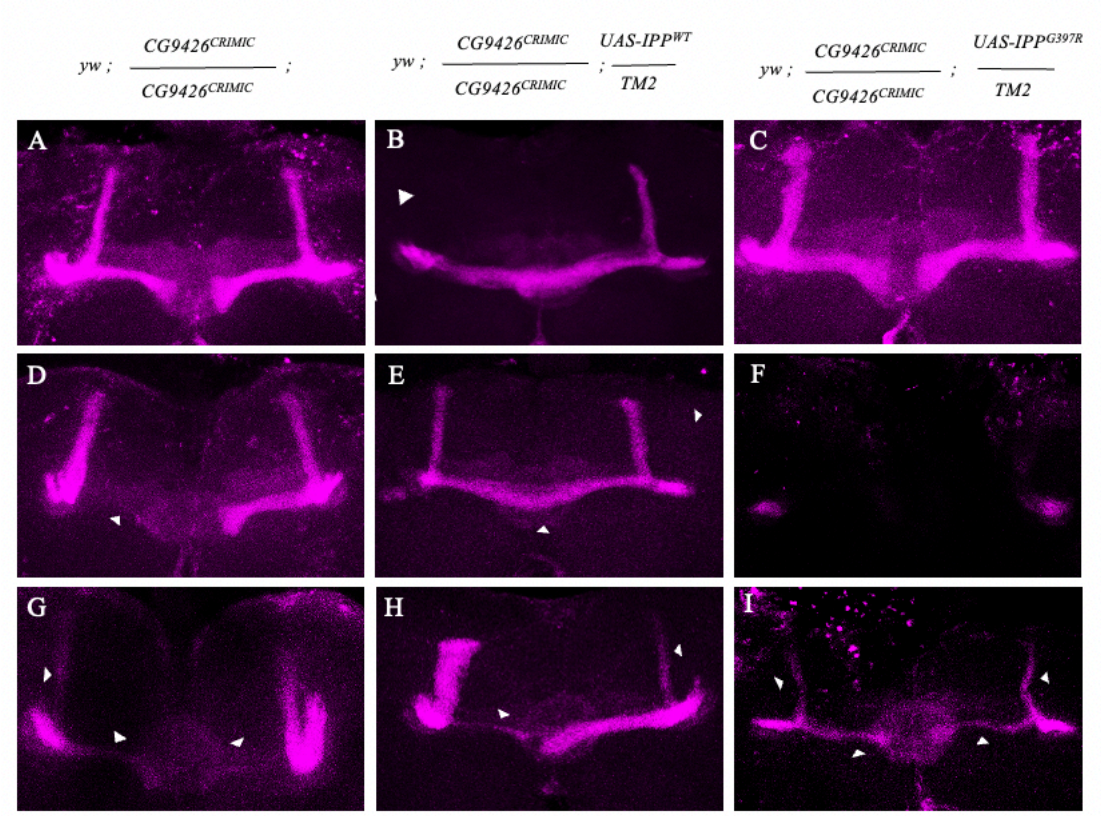

Figure 5.32. Examples of mushroom body phenotypes observed in *CG9426^{CRIMIC}/ CG9426^{CRIMIC}* (n=27, representative images for most frequent phenotypes: A,D,G), *CG9426^{CRIMIC}/ CG9426^{CRIMIC}; UAS-IPP^{WT}::HA* (n=29: B,E,H) and *CG9426^{CRIMIC}/ CG9426^{CRIMIC}; UAS-IPP^{G397R}* (n=27: C,F,I) lines. Staining of the α and β lobes of the mushroom body was conducted using a 1:50 anti-FasII antibody.

In order to assess whether the overexpression of *IPP^{WT}::HA* and *IPP^{G397R}::HA* under the control of the endogenous CG9426 promoter could impact mushroom body morphology, dissected brains from heterozygous *CG9426^{CRIMIC}/CyO* lines carrying transgenic *UAS-IPP::HA* constructs on their 3rd chromosome were examined. Out of the 19 brains analyzed in the *CG9426^{CRIMIC}/CyO*; *UAS-IPP^{WT}::HA* line: one of them showed beta lobe fusion phenotype (Figure 5.33 C), and another displayed axonal stalling (Figure 5.33 F). Conversely, among the 10 brains analyzed from the *CG9426^{CRIMIC}/CyO*; *UAS-IPP^{G397R}::HA* line, no defects in mushroom body morphology were observed.

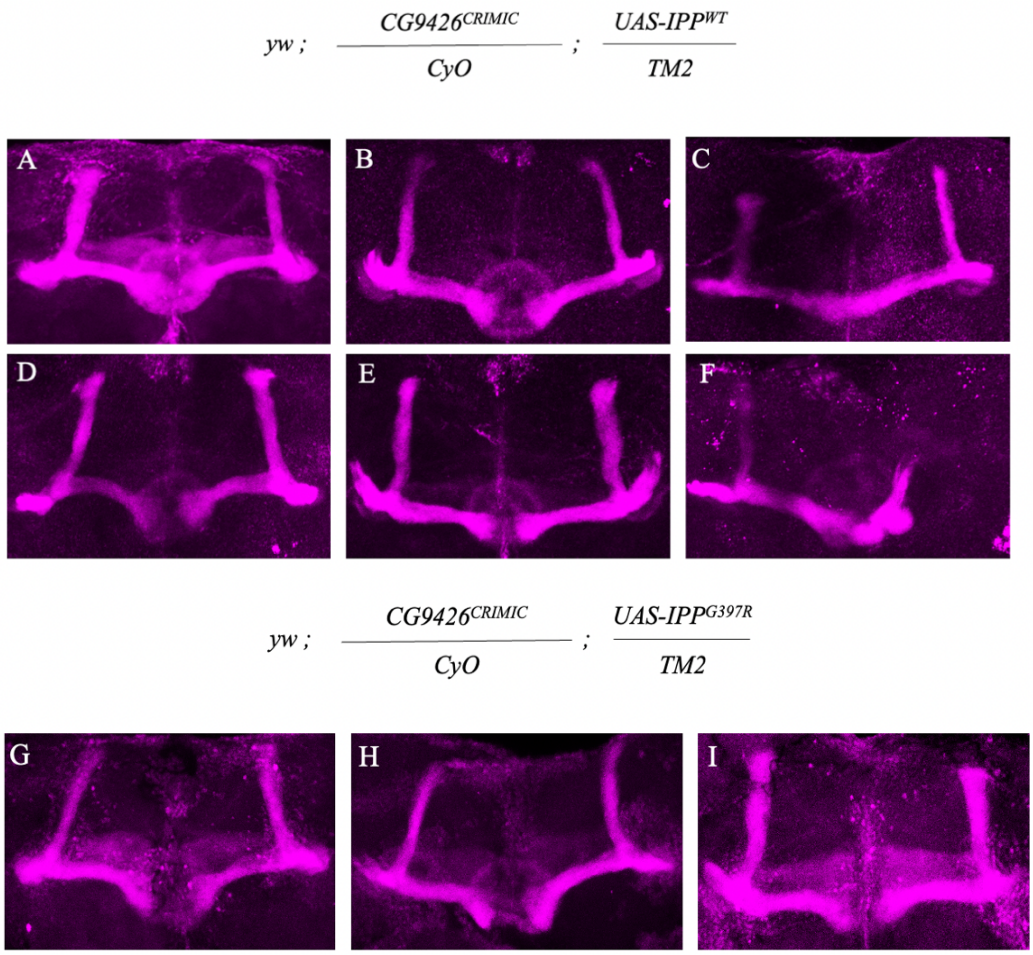

Figure 5.33. Examples of the mushroom body phenotypes observed in the heterozygous *C9426^{CRIMIC}/CyO; UAS-IPP^{WT}::HA* and *C9426^{CRIMIC}/CyO; UAS-IPP^{G397R}::HA* lines. anti-FasII was employed targeting the α and β lobes. In the *C9426^{CRIMIC}/CyO; UAS-IPP^{WT}::HA* line (n=19), one exhibited β lobe fusion (C), one displayed axon stalling in one of the α lobes (F). In the *C9426^{CRIMIC}/CyO; UAS-IPP^{G397R}::HA* line (n=10), no significant defects were observed.

5.7. Analysis of IPP^{WT} and IPP^{G397R} Localization in Mammalian Cells

To elucidate the function of IPP we focused on the characterization of its subcellular localization. *IPP^{WT}* and *IPP^{G397R}* were incorporated into the pLEX307 lentiviral vector via LR reaction, as outlined in Section 4.7. The resulting cloning reactions were subsequently transformed into Stbl3 competent cells. Plasmids were then isolated from the resulting transformants and subjected to digestion with the *Pst*I enzyme to confirm the successful integration of *IPP^{WT}* and *IPP^{G397R}* sequences into the vector. The gel electrophoresis result

of the digested plasmids is shown in Figure 5.31, wherein the expected bands were observed at 8025 and 1232 bp.

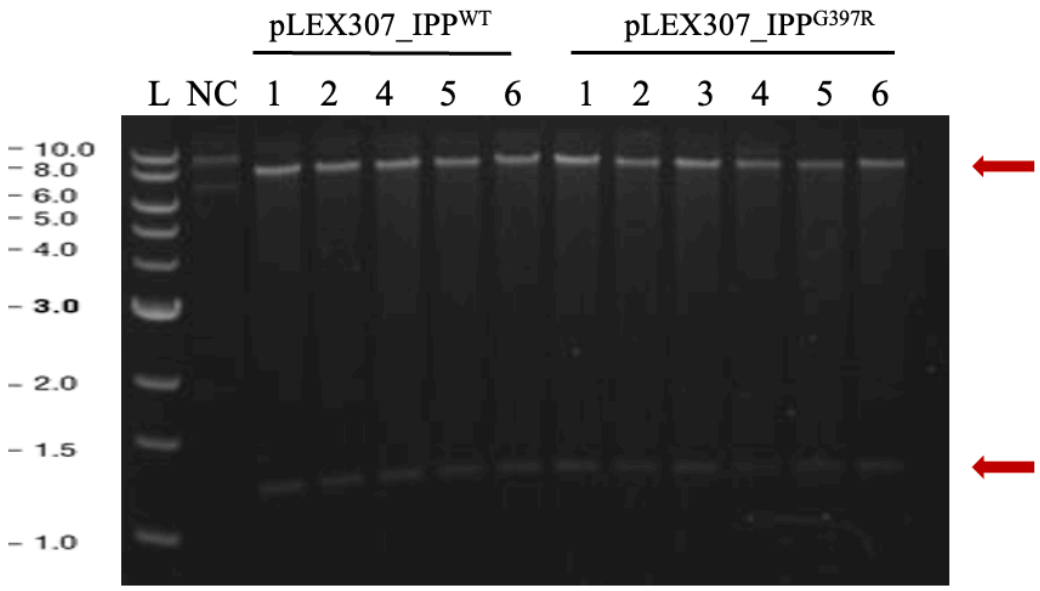

Figure 5.34. Electrophoregram of the restriction digestion reactions of pLEX307_IPP::V5 and pLEX307_IPP::V5 plasmids using the *Pst*I endonuclease. The pLEX307 plasmid was used as the negative control. The expected bands of 8025 and 1232 bp length are indicated by the red arrows. The bands of the expected sizes were successfully identified in all the analyzed plasmids.

The lentiviral packaging plasmid psPAX2, a 2nd generation component, and the envelope-expressing plasmid VSV-G were both amplified through transformation into Stbl3 competent cells. These plasmids were subsequently co-introduced with the pLEX307_IPP vectors into HEK293 cells for further analysis.

The next step involved transduction of HeLa cells with the viruses isolated from the HEK293 cells and isolation of cells stably expressing IPP. This experiment was conducted by Elif Darbuka Tula. The pLEX307 vector facilitated the transcription of the IPP gene, with a V5 tag incorporated at its C-terminus. Immunostaining experiments were initially conducted using an anti-V5 antibody and DAPI. During this initial staining process, a widespread IPP expression was observed in both the cytoplasm and the nucleus. Moreover, certain cells exhibited a nodular-like localization either on or near the plasma membrane

surface, resembling filopodial structures. It's worth noting that the expression pattern was not consistent across all cells, which might indicate a dynamic localization pattern of IPP during different cellular stages.

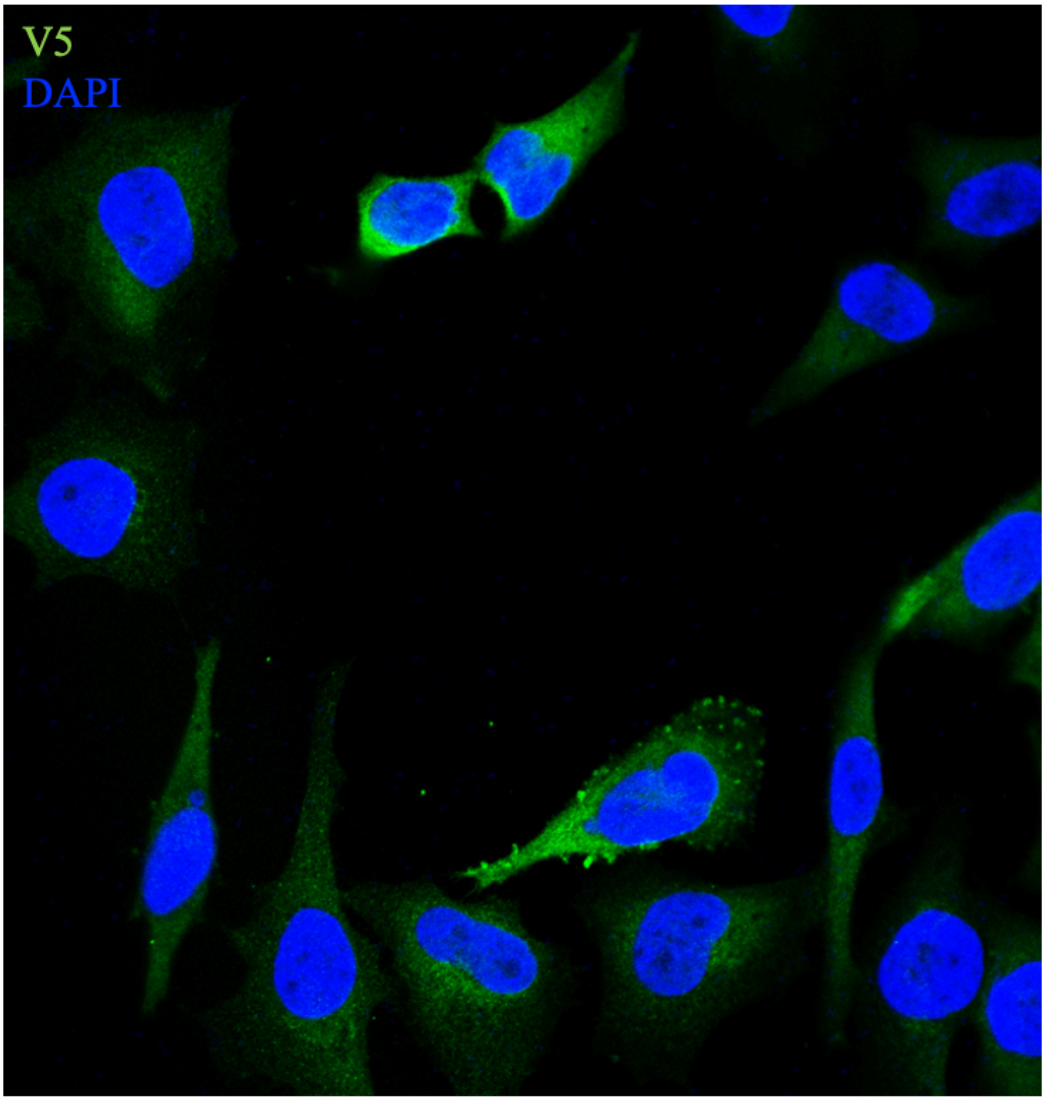

Figure 5.35. Localization pattern of IPP in mammalian cells. IPP was labeled using an anti-V5 mouse primary antibody, with Alexa Fluor 488 conjugated anti-mouse secondary antibody highlighting IPP (in green), while DAPI dye was employed for nuclei staining (in blue). The cells exhibited varied localization patterns of IPP-V5 at different stages.

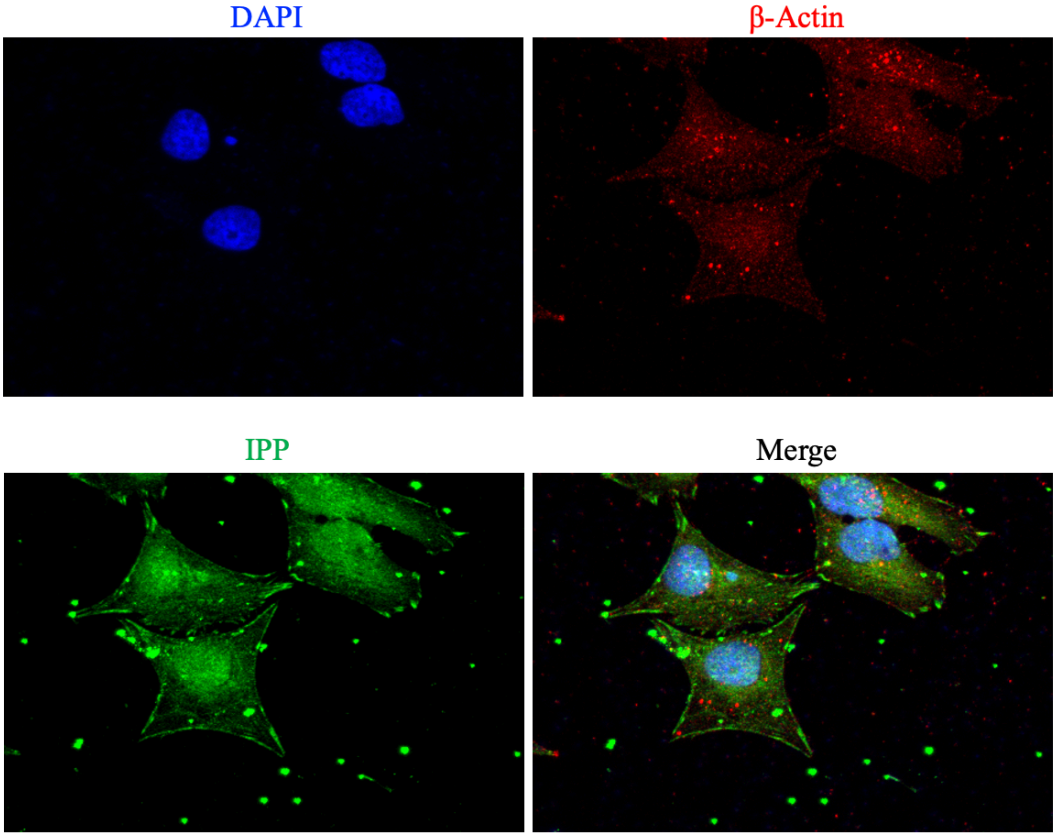

Figure 5.36. Expression pattern of IPP in mammalian cells. An anti-IPP (rabbit) primary antibody and Alexa Fluor 488-conjugated anti-rabbit secondary antibody were utilized to visualize IPP expression (green), while DAPI dye was applied for nuclei staining (blue), β-actin (mouse) primary antibody and Alexa Fluor 647-conjugated anti-mouse secondary antibody were used to label globular actin (red).

Another staining was conducted using an anti-IPP antibody to examine the expression in non-transduced HeLa cells. Cell nuclei were stained with DAPI, while globular Actin was highlighted using a β-Actin antibody. In this subsequent IPP antibody staining, a filamentous localization pattern was observed in near proximity to the plasma membrane, along with a substantial diffused but intense signal within the nucleus. To illustrate the colocalization of IPP with the actin cytoskeleton, β-Actin staining was performed (Figure 5.36). Identified filamentous localization pattern close to the plasma membrane was consistent with previous studies showing the interaction of IPP with actin filaments (Kim *et al*., 1999).

6. DISCUSSION

IPP was previously characterized as an actin-binding protein (Kim *et al*., 1999). Many actin-binding proteins play crucial roles in neurodevelopment, and genes encoding these proteins have been identified as causative factors for neurodevelopmental diseases (Luo, 2002; Liaci *et al*., 2021). Nevertheless, the specific role of IPP in the nervous system remains uncharacterized. This project aimed to uncover the role of IPP in learning and memory mechanisms using the fruit fly as a model organism. To achieve this goal, it was essential to establish functional orthology between human *IPP* and the fly *CG9426* genes. While the function of CG9426 has been predicted, it has not been fully characterized. Thus, to understand the role of CG9426 in the *Drosophila* nervous system, this study examined the expression pattern of *CG9426* in the fly brain and investigated the effects of *CG9426* mutations on mushroom body morphology. Additionally, the cellular localization of IPP in HeLa cell lines was analyzed to shed light on its potential cellular function.

6.1. *CG9426* is Expressed in Neuroblasts and Glia

The expression pattern of *CG9426* in larval and adult brains was investigated using the UAS-Gal4 system to gain a better understanding of its function. The Gal4 line was cloned by Çiğdem Soysal, a former member of our laboratory. The upstream intergenic region including the 5'UTR region presumably containing the *CG9426* promoter was cloned into the pBPGUw vector. The resulting vector was then integrated into the 3rd chromosome of flies, generating the *CG9426*-Gal4 fly line.

However, one limitation of this approach is that certain upstream enhancers or repressors located beyond the cloned upstream region might be missing or truncated, potentially leading to discrepancies between the expression patterns of the gene of interest and Gal4 (Jory *et al*., 2012). In contrast, the CRIMIC method enables GAL4 expression under the control of the endogenous promoter, including all distant regulatory elements of the gene of interest. Given these considerations, $CG9426^{CRIMIC}$ emerged as the preferable tool for characterizing the *CG9426* expression pattern.

Unfortunately, crosses between *CG9426*^{CRIMIC} and nuclear reporter lines *UAS-StingerRFP* and *UAS-nlacz* did not yield progeny carrying both constructs. This outcome is speculated to be due to the potential toxic effects of nuclear reporters driven by the GAL4 of the CG9426^{CRIMIC} construct. Efforts to use a GFP-tagged membrane reporter also faced challenges, as the CRIMIC construct already incorporates a GFP gene as a marker under the control of the P3 promoter. Notably, the P3 promoter is specific to the eye, being expressed in the compound eyes and single eyes of flies and is active in certain brain neurons as well (Figure 6.1).

To circumvent these hurdles, expression analysis with the *CG9426*^{CRIMIC} line was carried out by crossing it with *UAS-lacZ* and *UAS-mCD8::RFP* reporter lines. The results consistently aligned with the expression patterns obtained from crosses involving *CG9426*-Gal4 with *UAS-nlacZ* and *UAS-mCD8::GFP*, confirming that *CG9426* is expressed in the lamina and medulla regions of the optic lobes, as well as the dorsomedial region of the central brain.

When the *CG9426* expression pattern in the *CG9426-Gal4/UAS-nlacZ* line larval brain was analyzed, no expression in either neurons or glial cells was detected (Figure 5.11 D and E). During the third instar larval stage, the expression pattern of *CG9426* was noted to resemble the neuroblast expression pattern (Egger *et al*., 2008; Figure 1.2; Figure 5.11). IPP has been identified as an actin binding protein (Kim *et al*., 1999). It would be a solid approach to interpret the function of IPP and CG9426 in neuroblasts by considering prior knowledge about them. Mechanical forces induced by actin filaments (F-actin) are required for the development and differentiation of stem cells (Fan *et al*., 2019). Microfilaments are known to convey intracellular signals from external mechanical forces. In a previous study investigating the role of actin filaments in cell specialization, actin networks showed a higher nucleus-to-cytoplasm ratio in embryonic stem cells and induced pluripotent stem cells compared to differentiated cells (Pralong *et al*., 2006). Profilin, another actin-binding protein, regulates germline stem cell attachment to the apical hub by controlling JAK-STAT signaling in the *Drosophila* testis (Shields *et al*., 2014). *CG9426* is known to be expressed in the ovary and testis of *Drosophila* (Hudson *et al*., 2015). Although much more research is needed for a concrete conclusion, considering the known activity of actin-binding proteins in neuroblasts, the expression of *CG9426* in neuroblasts might indicate that it shares a similar

role with other actin-binding proteins expressed in glial cells and participates in the differentiation of neuroblasts. The larval brain of *Drosophila* has different subtypes of neuroblasts, including optic lobe neuroblasts and central brain neuroblasts (Fan *et al*., 2019; Figure 1.2). Based on the expression pattern of *CG9426* observed in this study, it can be speculated that CG9426 is expressed in all NB subtypes. However, further analysis using neuroblast-specific antibodies is necessary to reach a definite conclusion. Type II neuroblasts are precursors of astrocyte-like and ensheathing glia. As discussed below, the expression of CG9426 in adult flies resembles the expression pattern of astrocyte-like glia (Figure 5.17). The expression of *CG9426* might be conserved through differentiation from neuroblast to glial cells.

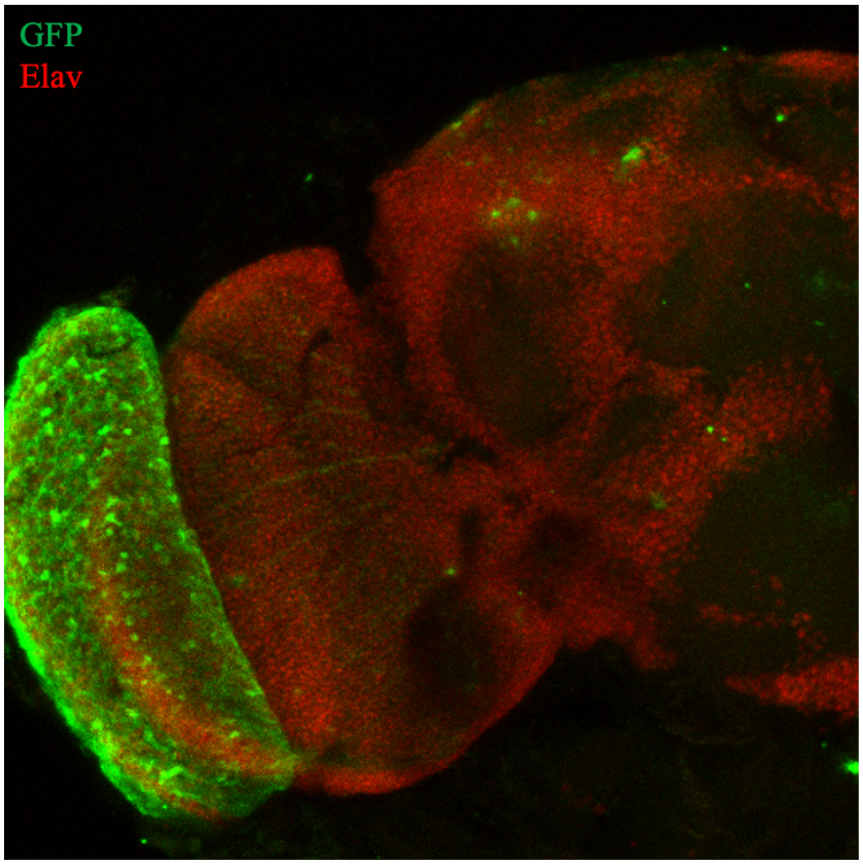

Figure 6.1. Expression pattern of GFP under the control of the 3xP3 promoter in the $CG9426^{CRIMIC}$ line. Neurons are labeled using a 1:50 anti-Elav (rat) primary antibody and a 1:800 Alexa Fluor 647-conjugated anti-rat secondary antibody (red). GFP expression is indicated using a 1:1000 anti-GFP (rabbit) primary antibody and a 1:800 Alexa Fluor 488-conjugated anti-rabbit secondary antibody (green).

The expression pattern of *CG9426* in the adult fly brain was characterized using the *CG9426^{CRIMIC}* driver and *UAS-lacZ* and *UAS-mCD8::RFP* reporter lines. The β-galactosidase (β-gal) signal pattern showed strong expression of *CG9426* in the lamina and medulla regions of the optic lobes and the protocerebral region of the central brain (CB). Despite our initial expectations for an ortholog of an ID-related gene, no expression of *CG9426* was detected in the cell bodies or axons of Kenyon cells that form the mushroom body (MB). However, *CG9426* expression was observed in the dorsolateral region of the brain, showing a pattern in which *CG9426*-expressing cells surrounded the mushroom body lobes and the peduncle. Due to the lethality associated with the expression of nuclear reporters under the control of Gal4 inserted in the *CG9426^{CRIMIC}* construct, the *CG9426*-Gal4 line was utilized. After crossing the *CG9426*-Gal4 line with the UAS-nlacz nuclear reporter line, strong β-gal signals were detected from the lamina and medulla regions of the optic lobes, the dorsolateral region around where the mushroom body resides, and mild signals from the region surrounding the antennal lobes and suboesophageal ganglia regions (Figure 5.13). Colocalization analysis with neuron-specific Elav and glia-specific Repo markers revealed that *CG9426* is expressed in glial cells but not neural cells in the adult brain.

Since IPP is an ID-causative gene encoding an actin-binding protein, it is plausible that its role in intellectual disability (ID) could be linked to actin remodeling processes in neurons, which are highly dynamic and essential for memory and learning (Konietzny *et al*., 2017; Korobova *et al*., 2010). Actin remodeling is well understood in neurons; however, the role of actin in glial cells is not as extensively explored. Similar to various cell types, the actin cytoskeleton in glial cells exhibits dynamic behavior and adapts to external and internal signals that mediate a multitude of functions. This includes facilitating morphological changes, enabling migration, supporting ensheathment of neurons, and facilitating communication with neurons (Thomason *et al*., 2020; Baorto *et al*., 1992). Actin filaments have been recognized as important during the differentiation of neural stem cells into radial glial cells (Sheilds *et al*., 2014). Actin dynamics regulate the movement of astrocytes; during neuroinflammation, for example, astrocytes transition to a more active state and transform their F-actin fibers into the globular G-actin form (Nishida *et al*., 2007; Hansson *et al*., 2015). It is reasonable to speculate that IPP might govern glia-neuron interactions by modulating actin dynamics in glial cells.

The membranous expression pattern reveals that *CG9426*-expressing cells enwrap the mushroom body (MB) lobes and the peduncle region, resembling the localization pattern of astrocyte-like and ensheathing glia (Figure 5.8; Yıldırım *et al*., 2019). Previous studies have demonstrated that astrocytes play a critical role in clearing γ axon fragments of the mushroom body during developmental axon fragmentation (Hakim *et al*., 2014; Watts *et al*., 2004; Awasaki, 2004). Axon pruning is a conserved mechanism in the remodeling of neuronal interactions throughout development, and this process is tightly regulated by astrocyte-like glia in the *Drosophila* mushroom body (Hakim *et al*., 2014).

To further explore the expression pattern of astrocyte-like glia, I employed the astrocyte-like glia-specific driver *Alrm*-Gal4 (Figure 5.21). However, the astrocyte-glia expression pattern does not perfectly align with the expression pattern of *CG9426* according to my results. To gain a more comprehensive understanding of the subtypes of glial cells where *CG9426* is expressed, co-staining experiments using specific antibodies like anti-Ran2 could provide more detailed insights (Jessen and Mirsky, 1983). Analyzing the expression pattern of *CG9426* throughout development is essential to decipher its role in axonal pruning in the mushroom body. The degeneration of initially projected axons occurs during the pupal stage. Therefore, analyzing the expression pattern of astrocyte-like and ensheathing glia during larval and pupal stages and comparing it with the expression pattern of *CG9426* will be valuable.

The primary focus of this study was to investigate the role of *CG9426* as an ortholog of an ID-causative gene, specifically in relation to the functioning of the mushroom body. The expression pattern of *CG9426* in the lamina region, as described in this study (Figure 5.14), was not within the scope of this investigation. Nevertheless, exploring the expression pattern in various brain regions may provide valuable insights into the cellular function of IPP.

It's worth noting that Cullin3 is an identified interaction partner of IPP, both in humans and flies (Arama *et al*., 2007; Kouranti *et al*., 2022). While IPP has not been extensively studied, there are numerous studies related to Cullin3. In *Drosophila* eye development, protein degradation mechanisms are mediated by Cul1 and Cul3 (Ou *et al*., 2002). The interaction between CG9426 and Cul3 in the fly brain, similar to what is observed in testes

and ovaries (Hudson, 2017), remains unknown. However, considering its membership in the Kelch protein family, CG9426 might act as an adaptor for Cul3, facilitating the ubiquitination of its targets in the fly brain (Kim *et al*., 1999).

6.2. Loss of Function of CG9426 Causes α and β Lobe Loss in the MB

To characterize the role of *CG9426* in neurodevelopment, this study employed two loss-of-function strategies: knockdown and knockout. The $CG9426^{RNAi}$ line was used for tissue-specific knockdown through RNA interference. For knockout, a mutant was generated in H. Bellen's lab using CRIMIC technology. This involved the insertion of the *SA-T2A-GAL4-polyA* cassette into the intronic region of *CG9426*, leading to disrupted transcription and the production of a truncated protein. The most notable phenotype observed in both knockout and knockdown approaches was the loss of MB lobes.

The viability rate of homozygous mutants was exceedingly low, with viable homozygous mutants surviving for no more than 7 days. Due to the limited sample size, morphological analysis in this study was confined to investigating the α and β lobes of the mushroom body. Brains of adult flies with homozygous mutant genotypes were dissected, and their mushroom bodies were visualized through FasII staining. The majority displayed loss of either an α lobe, β lobe, or both. Notably, no morphological defects were observed in heterozygous $CG9426^{CRIMIC}$ flies, implying that a single copy of *CG9426* is sufficient to maintain proper mushroom body formation.

To explore whether similar morphological defects in the mushroom body would arise if the efficiency of *CG9426* expression was reduced in specific tissues, the *UAS-*$CG9426^{RNAi}$ line was crossed with driver lines including *Elav*-Gal4, *Repo*-Gal4, *Alrm*-Gal4, *CG9426*-Gal4, and $CG9426^{CRIMIC}$.

According to the expression analysis conducted in this study, *CG9426* is not expressed in neurons. While the knockdown phenotypes induced by *Elav*-Gal4, *CG9426*-Gal4, or $CG9426^{CRIMIC}$ were not as severe or frequent as those induced by *Alrm*-Gal4, it was observed that Elav-Gal4-induced *CG9426* knockdown also resulted in mushroom body defects. Elav is considered as a common neuron specific marker. However, a previous study has shown

that in *Drosophila* embryos elav is transiently expressed in neuroblasts and glial cells (Berger *et al*., 2007). Considering the results I obtained from expression pattern analysis, as it seems to be expressed in neuroblasts; mushroom body defects observed in *Elav*-Gal4 induced knockdown might be due to a specific function of *CG9426* in CNS during early developmental stages. To ascertain whether these observed phenotypes are exceptions or consistent outcomes, increasing the sample size would provide more clarity.

Repo is expressed in all glial cell types except midline glia, and *Alrm*-Gal4 is a specific driver for astrocyte-like glia (Xiong *et al*., 1994). Interestingly, the knockdown induced by *Alrm*-Gal4 led to much more pronounced phenotypes compared to those resulting from *Repo*-Gal4 knockdown, despite *Alrm*-Gal4 targeting a smaller subset of cells. This effect could be attributed to differences in the expression levels of *Alrm*-Gal4 and *Repo*-Gal4. Gal4 constructs do not universally possess the same efficiency, as it depends on the included upstream regulatory sites and the activity of the gene's promoter.

Knockdown of *CG9426* using the Gal4 driver under the control of its own regulatory region also resulted in defects in mushroom body morphology. Depletion of *CG9426* expression led to a thinning of mushroom body lobes, aligning with the defects observed in homozygous $CG9426^{CRIMIC}$ mutants.

As expected, the $CG9426^{CRIMIC}$ construct, under the control of the endogenous *CG9426* promoter, induced knockdown in flies expressing only one fully transcribed copy of the gene. This resulted in severe lobe loss in their mushroom bodies, providing further support for the critical role of IPP and its fly ortholog CG9426 in the proper functioning of learning and memory mechanisms.

Unfortunately, the immunostainings conducted with the anti-FasII antibody in the knockdown experiments yielded a relatively weak signal in the central brain region. This raises concerns about the antibody's penetration efficiency, and extending the duration of FasII staining could be considered to enhance the signal penetration.

The efficiency of RNAi can vary among different organisms; however, it generally functions effectively in insects, eliciting a robust response (Zhu *et al*., 2020). While the results obtained from the knockout and knockdown analyses are coherent, a quantitative analysis of *CG9426* expression levels in the knockdown experiments should be carried out to determine the effectiveness of gene downregulation.

Mushroom body lobes consist of axonal projections from Kenyon cells. Axonal pruning is a highly regulated process that plays a pivotal role in the remodeling of neuronal interactions during neurodevelopment in the *Drosophila* mushroom body (Hakim *et al*., 2014). Previous studies have demonstrated the importance of glial cells in clearing mushroom body γ axon fragments during the developmental axon fragmentation process (Watts *et al*., 2004; Awasaki *et al*., 2004). However, it remains uncertain whether excessive axonal pruning occurred in *CG9426* knockdown and knockout lines, or if the observed morphological defects in the mushroom bodies were linked to a reduction in Kenyon cell numbers or the underdevelopment of axons on these cells.

The Dachshund gene encodes a transcription factor that is expressed in Kenyon cells and is essential for the proper development of mushroom bodies (Martini and Davis, 2005). Dachshund serves as a marker for Kenyon cells in *Drosophila* (Kurusu *et al*., 2000). Therefore, performing anti-Dachshund staining could offer insights into the nature of the morphological defects observed in the mushroom bodies of *CG9426* mutant and knockdown flies.

It's worth noting that the mushroom body is not the exclusive region associated with learning and memory in the fly brain. Approximately 40 genes have been linked to olfactory short-term memory, and among them, some are involved in visual and place memory, while others are specific to certain types of memory formation. It's possible that undisclosed defects may exist in other brain regions that were not explored in this study (Kahsai *et al*., 2011).

The mushroom body is particularly associated with short-term olfactory learning. Behavioral assays, such as the T-maze olfactory conditioning assay, conducted on knockout and knockdown lines, could provide further evidence supporting the hypothesis that the loss of *CG9426* function leads to learning and memory defects. Other assays, like a flight simulator for visual pattern recognition and a heat box for place memory, could also contribute to a deeper understanding of the effects of *CG9426* loss of function in the nervous system.

CRIMIC is based on the CRISPR system, which introduces the possibility of off-target cassette integration. Primers spanning exons 2-3 were designed for qPCR verification, which could determine whether the cassette disrupts expression if necessary. However, since the expression patterns observed from *CG9426*-Gal4 and $CG9426^{CRIMIC}$ were consistent, verification was deemed unnecessary. Additionally, second-site mutations were also a potential concern. This could be addressed through rescue analysis with a *UAS-CG9426* line, which would serve as a positive control for our rescue experiments.

A complementation assay was performed to confirm that the lethality observed in the *CG9426* knockout is indeed caused by the *CG9426* mutation. Both *Df(2L)* and *Dp(2;3)* lines used for complementation of the $CG9426^{CRIMIC}$ allele contain numerous genes that could be affected. The results of the complementation assay supported the hypothesis that the reduced viability of $CG9426^{CRIMIC}$ homozygous mutants is a consequence of the mutation in the *CG9426* gene itself, rather than off-target effects from the CRISPR technique.

It remains uncertain whether the low viability rate of homozygous *CG9426* mutants is attributed to a nervous system defect or not. Some insight could be gained through a mosaic analysis that induces a nervous system-specific knockout of *CG9426*. For this purpose, the bivalent UAS-Gal4 and FLP-FRT systems facilitated by the CRIMIC construct could be employed. Reversion of the CRIMIC cassette insertion can be achieved using the FLP-FRT system. Gal4 would enhance UAS-FLP expression, leading to the excision of the cassette in cells where the *CG9426* promoter is active. To maintain the insertion in specific cell types, a cell-type-specific Gal80 suppressor should be employed. Initially, I had planned to perform this mosaic analysis with a neuron-specific suppressor, *nSyb*-Gal80, before identifying

CG9426's expression pattern. However, given that CG9426 is expressed in glia rather than neurons, I would recommend using a glia-specific Gal80 construct instead.

Overall, CRIMIC proves to be a valuable strategy that can be employed with UAS-cDNA of the gene of interest, UAS-RNAi, UAS-reporter constructs, and can be utilized for functional analysis of both human and fly genes, along with their potential variants (Chao *et al*., 2017; Chen *et al*., 2016; Luo *et al*., 2017; Sandoval *et al*., 2014; Wangler *et al*., 2017; Yoon *et al*., 2017).

In conclusion, glial cells are of equal importance to their neural counterparts in maintaining the proper function of the nervous system. Consequently, it is not surprising that a disturbance in glia-specific gene expression can lead to abnormalities in learning and memory-related interactions within the fly brain. *CG9426*, identified to be expressed in cortex glia through expression analysis, could potentially play a role in the axonal pruning of Kenyon cells. Cortex glia within the central nervous system possess an actin-rich cytoskeleton that is pivotal in shaping glial processes and facilitating interactions with neurons and other glial cells.

6.3. Generation of IPP^{WT} and IPP^{G397R} Expressing Transgenic Lines

Drosophila serves as a convenient model for studying neurodevelopmental diseases. The fly ortholog of IPP, CG9426, shares 37% identity and 54% similarity with IPP. They display a high orthology score of 14/15 in DIOPT. However, the orthology relationship between CG9426 and IPP largely relies on sequence similarity. In this study, one of the objectives was to validate the functional orthology between CG9426 and IPP in order to simulate IPP-related impairments using CG9426 in *Drosophila*. To achieve this, transgenic lines were generated carrying *UAS-IPP^{WT}::HA* and *UAS-IPP^{G397R}::HA* constructs. *UAS-IPP^{G397R}* was designed to investigate whether the mutation identified in patients with ID in Family 2 (as described in Section 1.7 and Figure 1.3) would also manifest in flies.

Expression of IPP in the transgenic lines was initially assessed via Western Blot. Three biological replicates of *UAS-IPP^{WT}::HA* and *UAS-IPP^{G397R}::HA* were crossed with Actin-Gal4 to achieve ubiquitous expression. Lysates were prepared from the entire bodies of the flies, and HA antibody was utilized to detect IPP expression. Despite confirming that the 3x HA tag was in frame with both IPP^{WT} and IPP^{G397R} in pUAS vectors through sequencing, no band corresponding to the size of the tagged IPP could be identified in male flies. This Western Blot analysis was conducted twice using different Actin-Gal4 drivers, yielding consistent results. The bands observed in females were deemed nonspecific, as a similar band of the same size was also present in the negative control. Similar bands of the same size were previously noted in Western Blot results of distinct transgenic lines (Kahraman, 2022). It appears that the anti-HA antibody may be binding nonspecifically to a protein expressed in female flies. We have previously observed exceedingly low expression levels for certain UAS-transgenes, where inefficiency of expression was specific to particular coding sequences. Increasing the copy number of transgenes by generating homozygous lines for the transgene enabled the detection of the gene product (Fokina A., unpublished results). Hence, the absence of the HA-tagged IPP band in the Western Blot could potentially stem from IPP's expression level being below the detection threshold for both the wildtype and the mutant.

Transgenic lines were crossed with a robust photoreceptor-specific driver, longGMR-Gal4. Larval eye imaginal discs from these crosses were dissected and subjected to initial staining with anti-HA antibody. However, no specific HA expression was observable in either of the lines. In line with the Western blot findings, anti-HA antibody staining failed to reveal any expression for both constructs. Subsequently, the eye imaginal discs of larvae from the same *longGMR-Gal4; UAS-IPP::HA* lines were subjected to anti-IPP antibody staining. Interestingly, IPP expression was discernible in the line. However, no IPP expression was detectable in the *longGMR-Gal4; UAS-IPP^{G397R}::HA line*. It's possible that the IPP antibody might not recognize IPP^{G397R} due to a conformational change. To gain insight into IPP expression at the mRNA level, qPCR could be employed.

6.4. IPP and CG9426 are Functional Orthologs

Rescue analysis was carried out using generated transgenic lines expressing IPP^{WT} and IPP^{G397R} to explore the impact of human gene expression on the observed low viability rate and mushroom body dysmorphology in *CG9426* knockout mutants. The viability rate of $CG9426^{CRIMIC}$ homozygous mutants was markedly low, with only 2.7% of the adult flies being homozygous $CG9426^{CRIMIC}$. This value was over 10 times lower than the expected ratio of 33%. Expression of the human gene, both the wildtype and the mutant forms, led to an increase in the viability rate to approximately 14-17% in flies where CG9426 expression was disrupted. While the expression of IPP^{WT} was confirmed through IHC methods, validation of IPP^{G397R} expression could not be achieved. Interestingly, even though no expression of IPP was detectable via Western Blot or IHC, $UAS\text{-}IPP^{G397R}$ managed to rescue the lethality stemming from the absence of *CG9426*, comparable to the rescue by IPP^{WT}. The CRIMIC construct results in a complete knockout of *CG9426*, disrupting the transcription of both BTB and Kelch domains. On the contrary, IPP^{G397R} carries a point mutation in its third Kelch domain. Given that the low expression levels impeded the detection of IPP^{G397R} expression through WB and IHC analyses, yet this transgene successfully rescued the low viability rate in *CG9426* knockout mutants, it can be deduced that the lack of the BTB domain might be the primary cause of lethality in $CG9426^{CRIMIC}$ mutants. Furthermore, this lethality can be alleviated by expressing the IPP^{G397R} transgene, which retains a functional BTB domain while lacking functional Kelch repeats.

The aim of rescuing the low viability rate of knockout mutants was also pursued using a BAC construct, which encompasses the *CG9426* genomic region along with its regulatory sequences. The introduction of the BAC construct increased the viability rate of flies lacking *CG9436* expression from 2.7% to 18%, mirroring the effects observed with the *UAS-IPP::HA* constructs. This outcome reinforced the notion that IPP and CG9426 indeed function as orthologs. For a more robust positive control in lethality rescue, an improved construct could involve solely the integration of *UAS-CG9426* into the same landing site as the *UAS-IPP::HA* lines, providing a more refined basis for comparison with the transgenic *UAS-IPP::HA* constructs.

Throughout the genetic experiments in this study, viability tracking of genotypes and fly selection through phenotypic markers of the balancers was essential. Nevertheless, it's important to acknowledge that the balancers themselves might have exerted a significant influence on the emergence of homozygous *CG9426^{CRIMIC}* lines. Interestingly, the stocks resulting from *CG9426^{CRIMIC}/CG9426^{CRIMIC}; UAS-IPP, CG9426^{CRIMIC}/CG9426^{CRIMIC}; BAC^{99C18},* and *CG9426^{CRIMIC}/CG9426^{CRIMIC}; Dp(2;3)* crosses eventually lost the balancers and remained viable.

Regarding the rescue analysis for the observed morphological defects in homozygous mutants, UAS-IPP constructs were also employed. While they did reduce the occurrence of mutant phenotypes in the mushroom bodies, they did not achieve complete rescue of these phenotypes. Notably, the expression of *UAS-IPP^{WT}::HA* (but not *UAS-IPP^{G397R}::HA*) in the homozygous *CG9426^{CRIMIC}* mutant led to a new phenotype, specifically β lobe fusion. This outcome raises the possibility that IPP's role in protein degradation associated with axonal pruning could be perturbed due to overexpression, thereby resulting in insufficient pruning and subsequent lobe fusion.

6.5. IPP Shows Filamentous Localization Pattern in HeLa Cells

In order to gain deeper insights into the function of IPP, a comprehensive analysis of its subcellular localization was deemed essential. Cloning of IPP^{WT} and IPP^{G397R} was carried out within the lentiviral vector pLEX307, which ensures the expression of a V5 tag in alignment with the integrated gene. The V5 tag is a small entity that generally does not induce conformational changes in the tagged protein's structure. The success of the cloning procedure was confirmed through restriction digestion and subsequent sequencing. Transduction of cells was performed by Elif Darbuka Tula. The initial set of transduced cells underwent staining with anti-V5 antibodies, Phalloidin, and DAPI. Unfortunately, Phalloidin staining failed, thereby rendering the analysis of V5 signal colocalization with F-actin impossible. The visualization of IPP's distribution through anti-V5 staining unveiled a rather diffuse pattern within the cells. Distinct distribution patterns of signals were observed in cells at varying stages, signifying the dynamic nature of IPP's involvement in cellular processes. Certain cells exhibited node-like accumulations on the extracellular side of the membrane, resembling a vesicular expression pattern.

Subsequently, a repetition of staining was undertaken, employing anti-IPP and anti-β actin antibodies. β actin was chosen due to the initial staining, which revealed a globular IPP localization as opposed to a filamentous one. In contrast, a highly filamentous IPP pattern, particularly proximate to the membrane regions, was observed. This staining aimed to uncover both the transduced tagged IPP and endogenously expressed non-tagged IPP in HeLa cells. While the expression pattern of IPP appeared analogous to that of actin filaments, co-staining with Phalloidin dye or anti-F actin antibodies should be performed for validation. Notably, nuclear localization of IPP was evident in both stainings; however, a disparity arose between the two signal distribution patterns – the V5 staining exhibited a globular pattern, whereas the IPP staining displayed a filamentous one.

Given the vital role of the actin cytoskeleton in glial cells for cell structure maintenance, mechanical support, and the facilitation of dynamic cellular processes, it's notable that previous experiments confirmed the expression of CG9426 in glial cells. Based on the filamentous subcellular localization pattern of IPP, a hypothesis emerges that both IPP and its *Drosophila* ortholog might take part in axonal pruning by binding to actin filaments in glial cells, thus modulating their interactions with neurons.

In an effort to ascertain whether the point mutation corresponding to the Kelch domain of IPP, identified in individuals with ID from an Iranian family (as depicted in Figure 1.3), has any impact on IPP localization, a repetition of immunostainings with anti-V5 antibodies should be conducted for cells transduced with pLEX307-IPP^{WT}::V5 and pLEX307-IPP^{G397R}::V5 vectors.

6.6. IPP is an Adaptor for UPS

There exists a functional commonality among proteins crucial for neurodevelopment, encompassing transcription and chromatin remodeling factors, cell adhesion molecules, RNA processing, modification, and transport, protein ubiquitination, as well as fatty acid metabolism functions. A growing body of evidence underscores that many proteins linked to intellectual disability (ID) are particularly enriched within synaptic compartments. Recent studies have highlighted the pivotal role of these synaptic proteins in regulating dendritic spine morphogenesis and synaptic activity (Cresto *et al*., 2019). The ubiquitin-proteasome

system (UPS) plays a significant role in governing various cellular processes, and malfunctions in this system can lead to serious human ailments such as cancers and neurodegenerative disorders (Wang *et al*., 2005).

Both IPP and CG9426 are known to interact with Cullin3 and its *Drosophila* ortholog (Arama *et al*., 2007; Kouranti *et al*., 2022). Cullin3 functions as a ubiquitin E3 ligase and possesses several substrates that play roles in the organization of cytoskeletal structures. Kelch proteins, acting as adaptors for E3 ubiquitin ligases, facilitate the proper interaction of these ligases with their substrates. A prime example of this mechanism is the Cullin3-Gigaxonin-TBCB interaction. Gigaxonin, a member of the kelch protein family, is implicated in the pathogenesis of the neurodegenerative disorder giant axonal neuropathy (GAN), characterized by cytoskeletal abnormalities and the accumulation of intermediate filaments and microtubules. Gigaxonin oversees the degradation of tubulin folding cofactor B (TBCB), a protein binding to alpha-tubulin and regulating its appropriate folding. Disruptions in the UPS pathway under the control of Gigaxonin and Cullin3 can result in TBCB accumulation, which is believed to underlie the cytoskeletal anomalies observed in GAN. Significantly, the TBCB protein functions as a negative regulator of axonal growth (Wang *et al*., 2005).

The Cullin3-Gigaxonin-TBCB interaction serves as a compelling example of the potential cellular role of IPP. We postulate that, as another member of the Kelch protein superfamily, IPP could function as an adaptor for Cullin3, facilitating its binding to a target involved in axonal pruning. In the event of a malfunction in this tripartite interaction, the Cullin3 target may not undergo proper degradation, leading to the accumulation of this target and resulting in excessive axonal pruning, as observed in the cases of homozygous $CG9426^{CRIMIC}$ mutants and specific knockdown analyses targeting astrocyte-like glia and CG9426-expressing cells.

REFERENCES

Adams, J., R. Kelso, L. Cooley, 2000, "The Kelch Repeat Superfamily of Proteins: Propellers of Cell Function", *Trends in Cell Biology*, Vol. 10, No. 1, pp. 17-24.

Alliance of Genome Resources, "CG9426", https://www.alliancegenome.org/gene/FB:FBgn0032485, accessed on July 28, 2023.

American Psychiatric Association, 1980, *Diagnostic and Statistical Manual of Mental Disorders,* Third Edition, American Psychiatric Association, Washington, DC.

Arama, E., M. Bader, G.E. Rieckhof, H. Steller, 2007, "A Ubiquitin Ligase Complex Regulates Caspase Activation During Sperm Differentiation in *Drosophila*", *PLoS Biology*, Vol. 5, No. 10, pp. 251.

Aromolaran, K.A., K.A. Benzow, L.L. Cribbs, M.D. Koob, E.S. Piedras-Rentería, 2012, "Elimination of the Actin-Binding Domain in Kelch-like 1 Protein Induces T-type Calcium Channel Modulation Only in the Presence of a Potential Waveforms", *Journal of Signal Transduction*, Vol. 2012, p. 505346.

Aso, Y., K. Grübel, S. Busch, A. B. Friedrich, I. Siwanowicz, H. Tanimoto, 2009, "The Mushroom Body of Adult *Drosophila* Characterized by GAL4 Drivers", *Journal of Neurogenetics*, Vol. 23, No. 1, pp. 156-172.

Awasaki, T., K. Ito, 2004, "Engulfing Action of Glial Cells is Required for Programmed Axon Pruning During *Drosophila* Metamorphosis", *Current Biology*, Vol. 14, No. 8, pp. 668-677.

Awasaki, T., S.L. Lai, K. Ito, T. Lee, 2008, "Organization and Postembryonic Development of Glial Cells in the Adult Central Brain of *Drosophila*", *Journal of Neuroscience*, Vol. 28, No. 51, pp. 13742-13753.

Baorto, D.M., W. Mellado, M.L. Shelanski, 1992, “Astrocyte Process Growth Induction by Actin Breakdown”, *The Journal of Cell Biology*, Vol. 117, No. 2, pp. 357-367.

Bateman, J.R., A.M. Lee, C.T. Wu, 2006, “Site-specific Transformation of *Drosophila* via ϕC31 Integrase-Mediated Cassette Exchange”, *Genetics*, Vol. 173, No. 2, pp. 769-777.

Bellen, H.J., S. Yamamoto, 2015, “Morgan’s Legacy: Fruit Flies and the Functional Annotation of Conserved Genes”, *Cell*, Vol. 163, No. 1, pp. 12-14.

Bello, B.C., N. Izergina, E. Caussinus, H. Reichert, 2008, “Amplification of Neural Stem Cell Proliferation by Intermediate Progenitor Cells in *Drosophila* Brain Development”, *Neural Development*, Vol. 3, pp. 1-18.

Besson, M.T., D.B. Ré, M. Moulin, S. Birman, 2005, “High Affinity Transport of Taurine by the *Drosophila* Aspartate Transporter dEAAT2”, *The Journal of Biological Chemistry*, Vol. 280, No. 8, pp. 6621–6626.

Berger, C., S. Renner, S., K. Lüer, G. M. Technau, 2007, “The Commonly Used Marker ELAV is Transiently Expressed in Neuroblasts and Glial Cells in the *Drosophila* Embryonic CNS”, *Developmental dynamics: an official publication of the American Association of Anatomists*, Vol. 236, No. 12, pp. 3562-3568.

Bittern, J., N. Pogodalla, H. Ohm, L. Brüser, R. Kottmeier, S. Schirmeier, C. Klämbt, 2021, “Neuron–Glia Interaction in the *Drosophila* Nervous System”, *Developmental Neurobiology*, Vol. 81, No. 5, pp. 438-452.

Bolduc, F.V., K. Bell, H. Cox, K.S. Broadie, T. Tully, 2008, “Excess Protein Synthesis in *Drosophila* Fragile X mutants Impairs Long-Term Memory”, *Nature Neuroscience*, Vol. 11, No. 10, pp. 1143-1145.

Brand, A.H., A.S. Manoukian, N. Perrimon, 1994, “Ectopic Expression in *Drosophila*”, *Methods in Cell Biology*, Vol. 44, pp. 635-654.

Byun, C.K., J.S. Lee, B.C. Lim, K.J. Kim, Y. S. Hwang, J. H. Chae, 2015, "FOXG1 Mutation is a Low-Incidence Genetic Cause in Atypical Rett Syndrome", *Child Neurology Open*, Vol. 2, No. 1, p. 68151.

Campos, J. A., V. Hartenstein, 1985, "The Embryonic Development of *Drosophila melanogaster*", *Biosynthesis, Metabolism and Mode of Action of Invertebrate Hormone,* Springer-Verlag, Berlin, pp. 218-225.

Campos-Ortega, J. A., Y.N. Jan, 1991, "Genetic and Molecular Bases of Neurogenesis in *Drosophila melanogaster*", *Annual Review of Neuroscience*, Vol. 14, No. 1, pp. 399-420.

Capelson, M., V.G. Corces, 2005, "The Ubiquitin Ligase dTopors Directs the Nuclear Organization of a Chromatin Insulator", *Molecular Cell*, Vol. 20, No. 1, pp. 105-116.

Chao, H. T., M. Davids, E. Burke, J.G. Pappas, J.A. Rosenfeld, A.J. McCarty, K. Splinter, 2017, "A Syndromic Neurodevelopmental Disorder Caused by de Novo Variants in EBF3", *The American Journal of Human Genetics*, Vol. 100, No. 1, pp. 128-137.

Chen, K., T.S.Y. Ho, G. Lin, K.L. Tan, M.N. Rasband, H.J. Bellen, 2016, "Loss of Frataxin Activates the Iron/Sphingolipid/PDK1/Mef2 Pathway in Mammals", *Elife*, Vol. 5, p. 20732.

Chia, W., W.G. Somers, H. Wang, 2008, "*Drosophila* Neuroblast Asymmetric Divisions: Cell Cycle Regulators, Asymmetric Protein Localization, and Tumorigenesis", *The Journal of Cell Biology*, Vol. 180, No. 2, pp. 267-272.

Chubak, M.C., K.C. Nixon, M.H. Stone, N. Raun, S.L. Rice, M. Sarikahya, S.G. Jones, T. A. Lyons, T. E. Jakub, R. L. Mainland, M. J. Knip, T. N. Edwards, and J. M. Kramer, 2019, "Individual Components of the SWI/SNF Chromatin Remodelling Complex Have Distinct Roles in Memory Neurons of the *Drosophila* Mushroom Body", *Disease Models and Mechanisms*, Vol. 12, No. 3, p. 37325.

Codina-Sola, M., 2015, "Integrated Analysis of Whole-Exome Sequencing and Transcriptome Profiling in Males with Autism Spectrum Disorders", *Molecular Autism*, Vol. 6, No. 21, pp 1-16.

Cox, A.D., J. Virues-Ortega, F. Julio, T.L. Martin, 2017, "Establishing Motion Control in Children with Autism and Intellectual Disability: Applications for Anatomical and Functional MRI", *Journal of Applied Behavior Analysis*, Vol. 50, No. 1, pp. 8-26.

Cresto, N., L.E. Pillet, P. Billuart, N. Rouach, 2019, "Do Astrocytes Play a Role in Intellectual Disabilities?", *Trends in Neurosciences*, Vol. 42*,* No. 8, pp. 518-527.

Crittenden, J.R., E.M. Skoulakis, E.S. Goldstein, R.L. Davis, 2018, "*Drosophila* Mef2 is Essential for Normal Mushroom Body and Wing Development", *Biology Open*, Vol. 7, No. 9, p. 35618.

Czech, B., G.J. Hannon, 2011, "Small RNA Sorting: Matchmaking for Argonautes", *Nature Reviews Genetics*, Vol. 12, No. 1, pp. 19-31.

Diao, F., W. Mena, J. Shi, D. Park, F. Diao, P. Taghert, P., B.H. White, 2016, "The Splice Isoforms of the *Drosophila* Ecdysis Triggering Hormone Receptor Have Developmentally Distinct Roles", *Genetics*, Vol. 202, No. 1, pp. 175-189.

Diao, F., B.H. White, 2012, "A Novel Approach for Directing Transgene Expression in *Drosophila*: T2A-Gal4 in-Frame Fusion", *Genetics*, Vol. 190, No. 3, pp. 1139-1144.

Dierssen, M., G.J. Ramakers, 2006, "Dendritic Pathology in Mental Retardation: from Molecular Genetics to Neurobiology", *Genes, Brain and Behavior*, Vol. 5, pp. 48-60.

Dimou L, M. Simons, 2017, "Diversity of Oligodendrocytes and Their Progenitors", *Current Opinion Neurobiology,* Vol. 47, pp. 73–79.

Doherty, J., M.A. Logan, O.E. Taşdemir, M.R. Freeman, 2009, “Ensheathing Glia Function as Phagocytes in the Adult *Drosophila* Brain”, *Journal of Neuroscience*, Vol. 29, No. 15, pp. 4768–4781.

Eckfeldt, C.E., E.M. Mendenhall, C.M. Verfaillie, 2005, “The Molecular Repertoire of the 'Almighty' Stem Cell”, *Nature Reviews Molecular Cell Biology*, Vol. 6, No. 9, pp. 726-737.

Egger, B., J.M. Chell, A.H. Brand, 2008, “Insights into Neural Stem Cell Biology from Flies”, *Philosophical Transactions of the Royal Society B: Biological Sciences*, Vol. 363, No. 1489, pp. 39-56.

El-Danaf, R.N., R. Rajesh, C. Desplan, 2023, “Temporal Regulation of Neural Diversity in *Drosophila* and Vertebrates”, *Seminars in Cell and Developmental Biology*, Vol. 142, pp. 13-22.

Fan, Y.L., H.C. Zhao, B. Li, Z.L. Zhao, X.Q. Feng, 2019, “Mechanical Roles of F-actin in the Differentiation of Stem Cells: a Review”, *ACS Biomaterials Science and Engineering*, Vol. *5*, No. 8, pp. 3788-3801.

Fire, A., S. Xu, M.K. Montgomery, S.A. Kostas, S.E. Driver, C.C. Mello, 1998, “Potent and Specific Genetic Interference by Double-Stranded RNA in *Caenorhabditis elegans*”, *Nature*, Vol. 391, No. 6669, pp. 806-811.

FlyBase, “CG9426”, https://flybase.org/reports/FBgn0032485, accessed on July 10, 2023.

Germani, F., C. Bergantinos, L. A. Johnston, 2018, “Mosaic Analysis in *Drosophila*”, *Genetics*, Vol. 208, No. 2, pp. 473-490.

Guo, S., K.J. Kemphues, 1995, “Par-1, a Gene Required for Establishing Polarity in *C. elegans* Embryos, Encodes a Putative Ser/Thr Kinase That is Asymmetrically Distributed”, *Cell*, Vol. 81, No. 4, pp. 611-620.

Gnerer, J.P., K.J. Venken, H.A. Dierick, 2015, "Gene-Specific Cell Labeling Using MiMIC Transposons", *Nucleic Acids Research*, Vol. 43, No. 8, p. 56.

Hakim, Y., S.P. Yaniv, O. Schuldiner, 2014, "Astrocytes Play a Key Role in *Drosophila* Mushroom Body Axon Pruning", *PLoS One*, Vol. 9, No. 1, p. 86178.

Hanesch, U., K.F. Fischbach, M. Heisenberg, 1989, "Neuronal Architecture of the Central Complex in *Drosophila melanogaster*", *Cell and Tissue Research*, Vol. 257, pp. 343-366.

Hansson, E., 2015, "Actin Filament Reorganization in Astrocyte Networks is a Key Functional Step in Neuroinflammation Resulting in Persistent Pain: Novel Findings on Network Restoration", *Neurochemical Research*, Vol. 40, pp. 372-379.

Herculano-Houzel, S., 2014, "The Glia/Neuron Ratio: How It Varies Uniformly Across Brain Structures and Species and What That Means for Brain Physiology and Evolution", *Glia*, Vol. 62, No. 9, pp. 1377-1391.

Hilu-Dadia, R., K. Hakim-Mishnaevski, F. Levy-Adam, E. Kurant, 2018, "Draper-Mediated JNK Signaling is Required for Glial Phagocytosis of Apoptotic Neurons During *Drosophila* Metamorphosis", *Glia*, Vol. 66, No. 7, pp. 1520–1532.

Hoz, L., M. Simons, 2015, "The Emerging Functions of Oligodendrocytes in Regulating Neuronal Network Behaviour", *Bioessays*, Vol. 37, pp. 60–69.

Hu, H., K. Kahrizi, L. Musante, Z. Fattahi, R. Herwig, M. Hosseini, H. Najmabadi, 2019, "Genetics of Intellectual Disability in Consanguineous Families", *Molecular Psychiatry*, Vol. 24, No. 7, pp. 1027-1039.

Hudson, A.M., K.M. Mannix, L. Cooley, 2015, "Actin Cytoskeletal Organization in *Drosophila* Germline Ring Canals Depends on Kelch function in a Cullin-RING E3 Ligase", *Genetics*, Vol. 201, No. 3, pp. 1117-1131.

Ito, K., K. Suzuki, P. Estes, M. Ramaswami, D. Yamamoto, N.J. Strausfeld, 1998, "The Organization of Extrinsic Neurons and Their Implications in the Functional Roles of the Mushroom Bodies in *Drosophila melanogaster* Meigen", *Learning and Memory*, Vol. 5, No. 1, pp. 52-77.

Jan, Y.N., L.Y. Jan, 2001, "Asymmetric Cell Division in the *Drosophila* Nervous System", *Nature Reviews Neuroscience*, Vol. 2, No. 11, pp. 772-779.

Jansen, S., L.E. Vissers, B.B. de Vries, 2023, "The Genetics of Intellectual Disability", *Brain Sciences*, Vol. 13, No. 2, p. 231.

Jessen, K. R., R.H.O.N.A. Mirsky, 1983, "Astrocyte-Like Glia in the Peripheral Nervous System: an Immunohistochemical Study of Enteric Glia", *Journal of Neuroscience*, Vol. 3, No. 11, pp. 2206-2218.

Jory, A., C. Estella, M.W. Giorgianni, M. Slattery, T.R. Laverty, G.M. Rubin, R.S. Mann, 2012, "A Survey of 6,300 Genomic Fragments for Cis-Regulatory Activity in the Imaginal Discs of *Drosophila melanogaster*", *Cell Reports*, Vol. 2, No. 4, pp. 1014-1024.

Kanca, O., H.J. Bellen, F. Schnorrer, 2017, "Gene Tagging Strategies to Assess Protein Expression, Localization, and Function in *Drosophila*", *Genetics*, Vol. 207, No. 2, pp. 389-412.

Kahraman A., 2022, *Characterization of the E3 Ubiquitin Ligase RNFT2 Ortholog CG13605 in Drosophila melanogaster*, M.S. Thesis, Bogazici University.

Kahsai, L., T. Zars, 2011, "Learning and Memory in *Drosophila*: Behavior, Genetics, and Neural Systems", *International Review of Neurobiology*, Vol. 99, pp. 139-167.

Katz, G., E. Lazcano-Ponce, 2008, "Intellectual Disability: Definition, Etiological Factors, Classification, Diagnosis, Treatment and Prognosis", *Salud Pública de México*, Vol. 50, No. 2, pp. 132-141.

Kim, D. W., F. Hirth, 2009, "Genetic Mechanisms Regulating Stem Cell Self-Renewal and Differentiation in the Central Nervous System of *Drosophila*", *Cell Adhesion and Migration*, Vol. 3, No. 4, pp. 402-411.

Kim, I.F., E. Mohammadi, R.C.C. Huang, 1999, "Isolation and Characterization of IPP, a Novel Human Gene Encoding an Actin-Binding, Kelch-Like Protein", *Gene*, Vol. 228, No. 1-2, pp. 73-83.

Kim, S., J. Kim, S. Park, J.J., Park, and S. Lee, 2021, "*Drosophila* Graf Regulates Mushroom Body β-Axon Extension and Olfactory Long-Term Memory", *Molecular Brain*, Vol. 14, No. 1, p. 73

Konietzny, A., J. Bär, M. Mikhaylova, 2017, "Dendritic Actin Cytoskeleton: Structure, Functions, and Regulations", *Frontiers in Cellular Neuroscience*, Vol. 11, p. 147.

Korobova, F., T. Svitkina, 2010, "Molecular Architecture of Synaptic Actin Cytoskeleton in Hippocampal Neurons Reveals a Mechanism of Dendritic Spine Morphogenesis", *Molecular Biology of the Cell*, Vol. 21, No. 1, pp. 165-176.

Kouranti, I., W. Abdel Khalek, S. Mazurkiewicz, I. Loisel-Ferreira, A.M. Gautreau, L. Pintard, E. Clauser, 2022, "Cullin 3 Exon 9 Deletion in Familial Hyperkalemic Hypertension Impairs Cullin3-Ring-E3 Ligase (CRL3) Dynamic Regulation and Cycling", *International Journal of Molecular Sciences*, Vol. 23, No. 9, p. 5151.

Knoblich, J.A., 2008, "Mechanisms of Asymmetric Stem Cell Division", *Cell*, Vol. 132, No. 4, pp. 583-597.

Kremer, M.C., C. Jung, S. Batelli, G.M.Rubin, U. Gaul, 2017, "The Glia of the Adult *Drosophila* Nervous System", *Glia*, Vol. 65, No. 4, pp. 606–638.

Kurusu, M., T. Awasaki, L.M. Masuda-Nakagawa, H. Kawauchi, K. Ito, K. Furukubo-Tokunaga, 2002, "Embryonic and Larval Development of the *Drosophila* Mushroom Bodies: Concentric Layer Subdivisions and the Role of Fasciclin II", *Development*, Vol. 129, No. 2, pp. 409-419.

Kurusu, M., T. Nagao, U. Walldorf, S. Flister, W.J. Gehring, K. Furukubo-Tokunaga, 2000, "Genetic Control of Development of the Mushroom Bodies, the Associative Learning Centers in the *Drosophila* Brain, by the Eyeless, Twin of Eyeless, and Dachshund Genes", *Proceedings of the National Academy of Sciences USA*, Vol. 97, No. 5, pp. 2140-2144.

Lee, P.T., J. Zirin, O. Kanca, W.W. Lin, K.L. Schulze, D. Li-Kroeger, H.J. Bellen, 2018, "A Gene-Specific T2A-GAL4 Library for *Drosophila*", *Elife*, Vol. 7, p. 35574.

Liaci, C., M. Camera, G. Caslini, S. Rando, S. Contino, V. Romano, G.R. Merlo, 2021, "Neuronal Cytoskeleton in Intellectual Disability: from Systems Biology and Modeling to Therapeutic Opportunities", *International Journal of Molecular Sciences*, Vol. 22, No. 11, p. 6167.

Luo, L., 2002, "Actin Cytoskeleton Regulation in Neuronal Morphogenesis and Structural Plasticity", *Annual Review of Cell and Developmental Biology*, Vol. 18, No. 1, pp. 601-635.

Luo, X., J.A. Rosenfeld, S. Yamamoto, T. Harel, Z. Zuo, M. Hall, 2017, "Clinically Severe CACNA1A Alleles Affect Synaptic Function and Neurodegeneration Differentially", *PLoS Genetics*, Vol. 13, No. 7, p. 1006905.

Ma, Z., T. Stork, D.E. Bergles, M.R. Freeman, 2016, "Neuromodulators Signal Through Astrocytes to Alter Neural Circuit Activity and Behaviour", *Nature*, Vol. 539, No. 7629, pp. 428-432.

MacNamee, S.E., K.E. Liu, S. Gerhard, C.T. Tran, R.D. Fetter, A. Cardona, L.A. Oland, 2016, "Astrocytic Glutamate Transport Regulates a *Drosophila* CNS Synapse That Lacks Astrocyte Ensheathment", *The Journal of Comparative Neurology*, Vol. 524, No. 10, pp. 1979–1998.

Mariano, V., T. Achsel, C. Bagni, A.K. Kanellopoulos, 2020, "Modelling Learning and Memory in *Drosophila* to Understand Intellectual Disabilities", *Neuroscience*, Vol. 445, pp. 12-30.

Martini, S.R., R.L. Davis, 2005, "The Dachshund Gene is Required for the Proper Guidance and Branching of Mushroom Body Axons in *Drosophila melanogaster*", *Journal of Neurobiology*, Vol. 64, No. 2, pp. 133-144.

Maurange, C., A.P. Gould, 2005, "Brainy But Not Too Brainy: Starting and Stopping Neuroblast Divisions in *Drosophila*", *Trends in Neurosciences*, Vol. 28, No. 1, pp. 30-36.

McLennan, Y., J. Polussa, F. Tassone, R. Hagerman, 2011, "Fragile X Syndrome", *Current Genomics*, Vol. 12, No. 3, pp. 216-224.

Michel, C.I., 2004, "Defective Neuronal Development in the Mushroom Bodies of *Drosophila* Fragile X Mental Retardation 1 Mutants", *Journal of Neuroscience*, Vol. 24, No. 25, pp. 5798–5809.

Morandell, J., L.A. Schwarz, B. Basilico, 2021, "*Cul3* Regulates Cytoskeleton Protein Homeostasis and Cell Migration During a Critical Window of Brain Development", *Nature Communications,* Vol. 12, No. 1, p. 3058.

Morris-Rosendahl, D.J., M.A. Crocq, 2022, "Neurodevelopmental Disorders—the History and Future of a Diagnostic Concept", *Dialogues in Clinical Neuroscience*, Vol. 22, No. 1, pp. 65-72.

Muthukumar, A.K., T. Stork, M.R. Freeman, 2014, "Activity-Dependent Regulation of Astrocyte GAT Levels During Synaptogenesis", *Nature Neuroscience*, Vol. 17, No. 10, pp. 1340–1350.

Nakashima, M., 2020, "De Novo Variants in CUL3 are Associated with Global Developmental Delays with or without Infantile Spasms", *Journal of Human Genet*ics, Vol. 65, No. 9, pp. 727-734.

Ni, J.Q., R. Zhou, B. Czech, L. P. Liu, L. Holderbaum, D. Yang-Zhou, N. Perrimon, 2011, "A Genome-Scale shRNA Resource for Transgenic RNAi in *Drosophila*", *Nature Methods*, Vol. 8, No. 5, pp. 405-407.

Nishida, H., S. Okabe, 2007İ "Direct Astrocytic Contacts Regulate Local Maturation of Dendritic Spines", *Journal of Neuroscience*, Vol. 27, No. 2, pp. 331-340.

Olsen, M. L., B. S. Khakh, S. N. Skatchkov, M. Zhou, C. J. Lee, N. Rouach, 2015, "New Insights on Astrocyte Ion Channels: Critical for Homeostasis and Neuron-Glia Signaling", *Journal of Neuroscience*, Vol. 35, No. 41, pp. 13827-13835.

Omoto, J. J., P. Yogi, V. Hartenstein, 2015, "Origin and Development of Neuropil Glia of the *Drosophila* Larval and Adult Brain: Two Distinct Glial Populations Derived from Separate Progenitors", *Developmental Biology*, Vol. 404, No. 2, pp. 2–20.

Otto, N., Z. Marelja, A. Schoofs, H. Kranenburg, J. Bittern, K. Yildirim, C. Klämbt, 2018, "The Sulfite Oxidase Shopper Controls Neuronal Activity by Regulating Glutamate Homeostasis in *Drosophila* Ensheathing Glia", *Nature Communications*, Vol. 9, No. 1, p. 3514.

Ou, C.Y., Y. F. Lin, Y. J. Chen, C.T. Chien, 2002, "Distinct Protein Degradation Mechanisms Mediated by Cul1 and Cul3 Controlling Ci Stability in *Drosophila* Eye Development", *Genes and Development*, Vol. 16, No. 18, pp. 2403-2414.

Parinejad, N., E. Peco, E., T. Ferreira, S.M. Stacey, D.J. van Meyel, 2016 “Disruption of an EAAT-Mediated Chloride Channel in a *Drosophila* Model of Ataxia”, *Journal of Neuroscience*, Vol. 36, No. 29, pp. 7640–7647.

Peco, E., S. Davla, D.M. Camp, S. Stacey, M. Landgraf, D. Meyel, 2016, “*Drosophila* Astrocytes Cover Specific Territories of the CNS Neuropil and are Instructed to Differentiate by Prospero, a Key Effector of Notch”, *Development*, Vol. 143, No. 7, pp. 1170–1181.

Pfeiffer, B.D., A. Jenett, A.S. Hammonds, T.T.B. Ngo, S. Misra, C. Murphy, G.M. Rubin, 2008, “Tools for Neuroanatomy and Neurogenetics in *Drosophila*”, *Proceedings of the National Academy of Sciences USA*, Vol. 105, No. 28, pp. 9715-9720.

Pralong, D., P.J. Verma, 2006, “Techniques for Nuclear Transfer to Mouse Embryonic Stem Cells”, *Nuclear Transfer Protocols: Cell Reprogramming and Transgenesis*, pp. 269-283.

Purice, M.D., A. Ray, E.J. Münzel, B.J. Pope, D.J. Park, S.D. Speese, M.A. Logan, 2017, “A Novel *Drosophila* Injury Model Reveals Severed Axons are Cleared Through a Draper/MMP-1 Signaling Cascade”, *Elife*, Vol. 6, p. 23611.

Purves D., G.J. Augustine, D. Fitzpatrick, 2001, *Neuroscience,* Second Edition, Sinauer Associates, Sunderland.

Ransom B, T. Behar, M. Nedergaard, 2003, “New Roles for Astrocytes”, *Trends Neuroscience*, Vol. 26, pp. 520–522.

Redin, C., 2017, “The Genomic Landscape of Balanced Cytogenetic Abnormalities Associated with Human Congenital Anomalies”, *Nature Genetics,* Vol. 49, pp. 36–45.

Renn, S.C., J.D. Armstrong, M. Yang, Z. Wang, X. An, K. Kaiser, P.H. Taghert, 1999, "Genetic Analysis of the *Drosophila* Ellipsoid Body Neuropil: Organization and Development of the Central Complex", *Journal of Neurobiology*, Vol. 41, No. 2, pp. 189-207.

Rives-Quinto, N., H. Komori, C.M. Ostgaard, D.H. Janssens, S. Kondo, Q. Dai, C.Y. Lee, 2020, "Sequential Activation of Transcriptional Repressors Promotes Progenitor Commitment by Silencing Stem Cell Identity Genes", *Elife*, Vol. 9, p. 56187.

Rolls, E. T.,1987, "Information Representation, Processing and Storage in the Brain: Analysis at the Single Neuron Level", *The Neural and Molecular Bases of Learning*, pp. 503-540.

Rueter, S.M., T.R. Dawson, R.B. Emeson, 1999, "Regulation of Alternative Splicing by RNA Editing", *Nature*, Vol. 399, No. 6731, pp. 75-80.

Saini, N., H. Reichert, 2012, "Neural Stem Cells in *Drosophila*: Molecular Genetic Mechanisms Underlying Normal Neural Proliferation and Abnormal Brain Tumor Formation", *Stem Cells International*, 2012, Vol. 486169.

Salinas, G.D., L.A. Blair, L.A. Needleman, J.D. Gonzales, Y. Chen, M. Li, J. Marshall, 2006, "Actinfilin is a Cul3 Substrate Adaptor, Linking GluR6 Kainate Receptor Subunits to the Ubiquitin-Proteasome-Pathway", *Journal of Biological Chemistry*, Vol. 281, No. 52, pp. 40164-40173.

Sandoval, H., C.K. Yao, K. Chen, M. Jaiswal, T. Donti, Y.Q. Lin, H.J. Bellen, 2014, "Mitochondrial Fusion But Not Fission Regulates Larval Growth and Synaptic Development Through Steroid Hormone Production", *Elife*, Vol. 3, p. 03558.

Schafer D.P., B. Stevens, 2015, "Microglia Function in Central Nervous System Development and Plasticity", *Cold Spring Harbor Perspectives Biology*, Vol. 7, p. 20545.

Senatore, A., H. Raiss, P. Le, 2016, "Physiology and Evolution of Voltage-Gated Calcium Channels in Early Diverging Animal Phyla: Cnidaria, Placozoa, Porifera and Ctenophora", *Frontiers in Physiology*, Vol. 7, p. 481.

Sengupta, S., L.B. Crowe, S. You, M.A. Roberts, F.R. Jackson, 2019, "A Secreted Ig-Domain Protein Required in Both Astrocytes and Neurons for Regulation of *Drosophila* Night Sleep", *Current Biology*, Vol. 29, No. 15, pp. 2547-2554.

Shi, X., S. Xiang, J. Cao, H. Zhu, B. Yang, Q. He, M. Ying, 2019, "Kelch-Like Proteins: Physiological Functions and Relationships with Diseases", *Pharmacological Research*, Vol. 148, p. 104404.

Shields, A.R., A.C. Spence, Y.M. Yamashita, E.L. Davies, M.T. Fuller, 2014, "The Actin-Binding Protein Profilin is Required for Germline Stem Cell Maintenance and Germ Cell Enclosure by Somatic Cyst Cells", *Development*, Vol. 141, No. 1, pp. 73-82.

da Silva Montenegro, E. M., 2019, "Meta-Analyses Support Previous and Novel Autism Candidate Genes: Outcomes of an Unexplored Brazilian Cohort", *Autism Research,* Vol. 13, No. 2, pp. 199-206.

Simons, M., K. A. Nave, 2016, "Oligodendrocytes: Myelination and Axonal Support", *Cold Spring Harbor Perspectives in Biology*, Vol. 8, No. 1, p. 020479.

Sleyp, Y., I. Valenzuela, A. Accogli, K. Ballon, B. Ben-Zeev, S. F. Berkovic, 2022, "De Novo Missense Variants in the E3 Ubiquitin Ligase Adaptor KLHL20 Cause a Developmental Disorder with Intellectual Disability, Epilepsy, and Autism Spectrum Disorder", *Genetics in Medicine*, Vol. 24, No. 12, pp. 2464-2474.

Sousa-Nunes, R., L. Y. Cheng, A.P. Gould, 2010, "Regulating Neural Proliferation in the *Drosophila* CNS", *Current Opinion in Neurobiology*, Vol. 20, No. 1, pp. 50-57.

Soustelle, L., M.T. Besson, T. Rival, S. Birman, 2002, "Terminal Glial Differentiation Involves Regulated Expression of the Excitatory Amino Acid Transporters in the *Drosophila* Embryonic CNS", *Developmental Biology*, Vol. 248, No. 2, pp. 294-306.

Stogios, P.J., G.S. Downs, J.J. Jauhal, S.K. Nandra, G.G. Privé, 2005, "Sequence and Structural Analysis of BTB Domain Proteins", *Genome Biology*, Vol. 6, pp. 1-18.

Stork, T., D. Engelen, A. Krudewig, M. Silies, R. J. Bainton, C. Klämbt, 2008, "Organization and Function of the Blood-Brain Barrier in *Drosophila*", *Journal of Neuroscience*, Vol. 28, No. 3, pp. 587–597.

Tanaka, N.K., H. Tanimoto, K. Ito, 2008, "Neuronal Assemblies of the *Drosophila* Mushroom Body", *Journal of Comparative Neurology*, Vol. 508, No. 5, pp. 711-755.

Tasdemir-Yilmaz, O.E., M.R. Freeman, 2014, "Astrocytes Engage Unique Molecular Programs to Engulf Pruned Neuronal Debris from Distinct Subsets of Neurons", *Genes and Development*, Vol. 28, No. 1, pp. 20-33.

Technau, G., M. Heisenberg, 1982, "Neural Reorganization During Metamorphosis of the Corpora Pedunculata in *Drosophila melanogaster*", *Nature*, Vol. 295, No. 5848, pp. 405-407.

Thomason, E.J., M. Escalante, D.J. Osterhout, B. Fuss, 2020, "The Oligodendrocyte Growth Cone and Its Actin Cytoskeleton: a Fundamental Element for Progenitor Cell Migration and CNS Myelination", *Glia*, Vol. 68, No. 7, pp. 1329-1346.

Ullian, E.M., K.S. Christopherson, B.A. Barres, 2004, "Role for Glia in Synaptogenesis", *Glia*, Vol. 47, No. 3, pp. 209-216.

Vanderheyden, W.M., A.G. Goodman, R.H. Taylor, M.G. Frank, H.P. Van Dongen, J.R. Gerstner, 2018, "Astrocyte Expression of the *Drosophila* TNF-Alpha Homologue, Eiger, Regulates Sleep in Flies", *PLoS Genetics*, Vol. 14, No. 10, p. 1007724.

Varoqueaux, F., D. Fasshauer, 2017, “Getting Nervous: an Evolutionary Overhaul for Communication”, *Annual Review of Genetics*, Vol. 51, pp. 455-476.

Venken, K. J., J.W. Carlson, K.L. Schulze, H. Pan, Y. He, R. Spokony, R.A. Hoskins, 2009, “Versatile P[acman] BAC Libraries for Transgenesis Studies in *Drosophila melanogaster*”, *Nature Methods*, Vol. 6, No. 6, pp. 431-434.

Waddell, S., J.D. Armstrong, T. Kitamoto, K. Kaiser, W.G. Quinn, 2000, “The Amnesiac Gene Product is Expressed in Two Neurons in the *Drosophila* Brain That are Critical for Memory”, *Cell*, Vol. 103, No. 5, pp. 805-813.

Wang, W., J. Ding, E. Allen, P. Zhu, L. Zhang, H. Vogel, Y. Yang, 2005, “Gigaxonin Interacts with Tubulin Folding Cofactor B and Controls Its Degradation Through the Ubiquitin-Proteasome-Pathway”, *Current Biology*, Vol 15, No. 22, pp. 2050-2055.

Wangler, M.F., Y. Hu, J.M. Shulman, 2017, “*Drosophila* and Genome-Wide Association Studies: a Review and Resource for the Functional Dissection of Human Complex Traits”, *Disease Models and Mechanisms*, Vol. 10, No. 2, pp. 77-88.

Watts, R.J., O. Schuldiner, J. Perrino, C. Larsen, L. Luo, 2004, “Glia Engulf Degenerating Axons During Developmental Axon Pruning”, *Current Biology*, Vol. 14, No. 8, pp. 678-684.

Wong, M., 2019, “The Role of Glia in Epilepsy, Intellectual Disability, and Other Neurodevelopmental Disorders in Tuberous Sclerosis Complex”, *Journal of Neurodevelopmental Disorders,* Vol. 11, No. 1, p. 30.

Yang, Q., J. Zhao, D. Chen, Y. Wang, 2021, “E3 Ubiquitin Ligases: Styles, Structures and Functions”, *Molecular Biomedicine*, Vol. 2, pp. 1-17.

Yildirim, K., J. Petri, R. Kottmeier, C. Klämbt, 2019, “Drosophila Glia: Few Cell Types and Many Conserved Functions”, *Glia*, Vol. 67, No. 1, pp. 5-26.

Yoon, W.H., H. Sandoval, S. Nagarkar-Jaiswal, M. Jaiswal, S. Yamamoto, N.A. Haelterman, H.J. Bellen, 2017, "Loss of Nardilysin, a Mitochondrial Co-Chaperone for α-Ketoglutarate Dehydrogenase, Promotes mTORC1 Activation and Neurodegeneration", *Neuron*, Vol. 93, No. 1, pp. 115-131.

Young, J.M., J.D. Armstrong, 2010, "Building the Central Complex in *Drosophila*: the Generation and Development of Distinct Neural Subsets", *Journal of Comparative Neurology*, Vol. 518, No. 9, pp. 1525-1541.

Young, J.M., J.D. Armstrong, 2010, "Structure of the Adult Central Complex in *Drosophila*: Organization of Distinct Neuronal Subsets", *Journal of Comparative Neurology*, Vol. 518, No. 9, pp. 1500-1524.

Yu, F., O. Schuldiner, 2014, "Axon and Dendrite Pruning in *Drosophila*", *Current Opinion in Neurobiology*, Vol. 27, pp. 192-198.

Xiong, W.C., H. Okano, N.H. Patel, J.A. Blendy, C. Montell, 1994, "Repo Encodes a Glial-Specific Homeo Domain Protein Required in the *Drosophila* Nervous System", *Genes and Development*, Vol. 8, No. 8, p. 981.

Zhang B, J. Zou, L. Han, N. Rensing, M. Wong, 2016, "Microglial Activation During Epileptogenesis in a Mouse Model of Tuberous Sclerosis Complex", *Epilepsia*, Vol. 57, pp. 1317–1325.

Zhu, H., L. Chen, Y. Yang, Z. Zhu, X. Zhang, W. Li, G. Ou, 2017, "The Glial Actin Cytoskeleton Regulates Neuronal Ciliogenesis", *Cell Research*, Vol. 27, No. 3, pp. 448-451.

Zhu, K.Y., S.R. Palli, 2020, "Mechanisms, Applications, And Challenges of Insect RNA Interference", *Annual Review of Entomology*, Vol. 65, pp. 293-311.